MODELING AND SIMULATION OF NANOPARTICULATE LITHIUM IRON PHOSPHATE BATTERY ELECTRODES

by

Bernardo Orvananos Murguia

A dissertation submitted in partial fulfillment
of the requirements for the degree of
Doctor of Philosophy
(Materials Science and Engineering)
in The University of Michigan
2014

Doctoral Committee:

Associate Professor Katsuyo S. Thornton, Chairperson
Associate Professor Emmanuelle Marquis
Assistant Professor Charles W. Monroe
Assistant Professor Donald J. Siegel

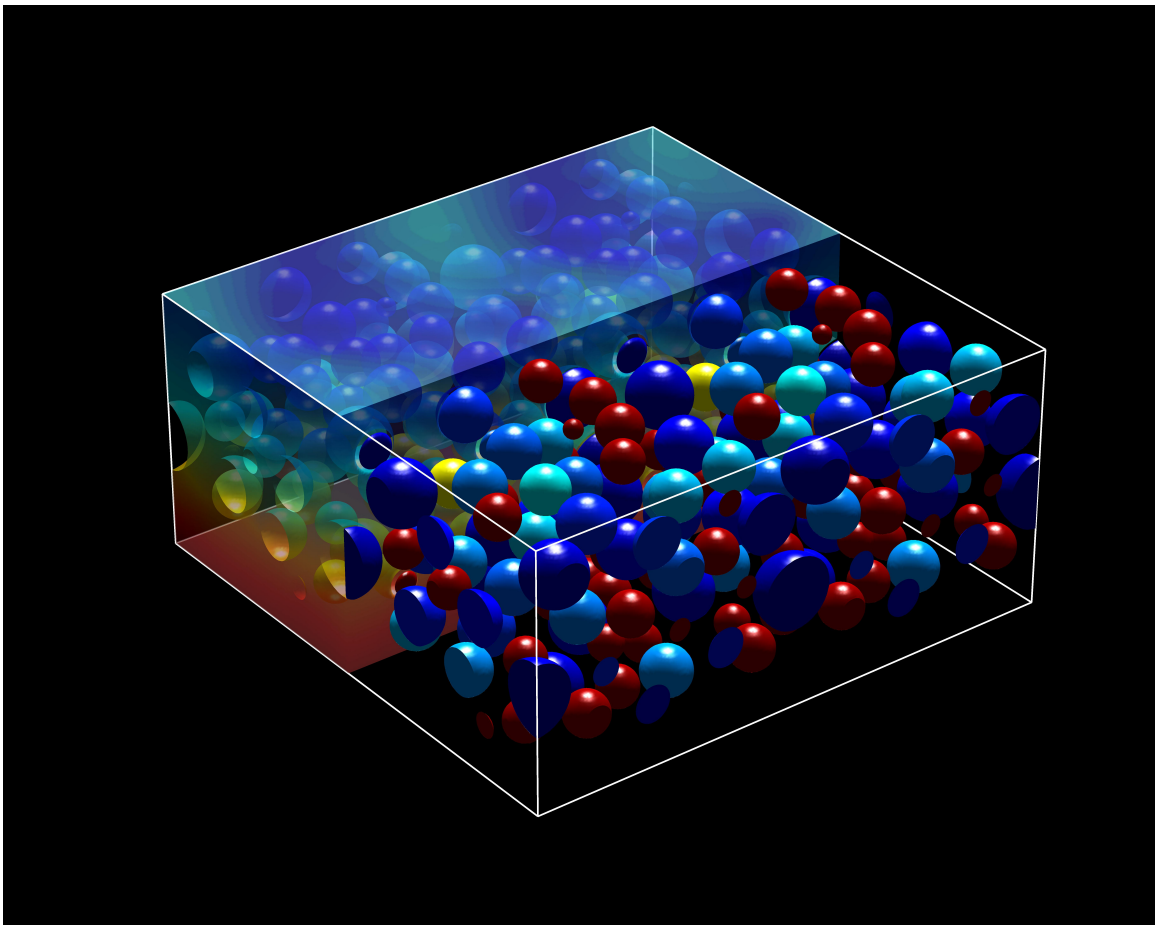

Agglomerate of $LiFePO_4$ nanoparticles. The Li concentration in the particles is shown in front, and the Li concentration in the electrolyte is shown in back. High Li concentrations are represented in red, and low Li concentrations are represented in blue. This image won the first place award in the category "Simulated Microstructures as Products of Computational Materials Science" in the 2012 Materials Science and Engineering Imaging Microstructure Contest.

To My Parents

ACKNOWLEDGEMENTS

First, I would like to acknowledge my advisor Prof. Katsuyo Thornton and Dr. Hui-Chia Yu for their help and patience over the years. I would like to thank the current and former members of the Thornton group: Dr. Larry Aagesen, Dr. Chloe Funkhouser, Dr. David Montiel, Dr. Ali Ramazani, Dr. Oncu Akyildiz, Dr. Nirand Pisutha-Arnond, Dr. Hsun-Yi Chen, Dr. Susan Gentry, Dr. Susanta Ghosh, Dr. Candace Gilet, Stephen DeWitt, Tapiwa Mushove, Beck Andrews, Alex Chadwick, Victor Chan, Andrea Jokisaari, Jason Luce, Reshma Mathew, Amber Wingfield, Chal Parks, Min-Ju Choe, and Connor Murray. I would also like to acknowledge my collaborators: Prof. Gerbrand Ceder, Prof. Clare Grey, Prof. Martin Bazant, Dr. Rahul Malik, Dr. Todd Ferguson, Aziz Abdellahi, Hao Liu, and Fiona Strobridge.

I would like to express my appreciation for financial support from the Northeastern Center for Chemical Energy Storage, an Energy Frontier Research Center funded by the United States Department of Energy, Basic Energy Sciences under award number DE-SC0001294, and from the National Science Foundation under Contract No. DMS-0842504.

Last but not least, I would like to thank Dr. Anne Vazquez, Bo Varga, Adalberto Flores, and Jakob Fleischmann, who have served as mentors at different moments of my career, as well as my family, girlfriend, and friends for all their support.

TABLE OF CONTENTS

LIST OF FIGURES

Figure

LIST OF TABLES

Table

LIST OF ACRONYMS

3D three-dimensional

ADLR alternating direction line relaxation

DOD depth of discharge

EDXRD energy dispersive x-ray diffraction

FP $FePO_4$

LFP $LiFePO_4$

LHS left-hand side

PET porous electrode theory

PLED particle-level electrochemical dynamics

PTFE polytetrafluoroethylene

RHS right-hand side

SBM smoothed boundary method

SEI solid electrolyte interphase

STXM scanning transmission x-ray microscopy

SOC state of charge

TEM transmission electron microscopy

ABSTRACT

MODELING AND SIMULATION OF NANOPARTICULATE LITHIUM IRON PHOSPHATE BATTERY ELECTRODES

by

Bernardo Orvananos Murguia

Chairperson: Katsuyo S. Thornton

Elucidating the complex charge/discharge dynamics in nanoparticulate phase-separating electrode materials such as lithium iron phosphate, $LiFePO_4$, is a challenging task because of the small temporal and spatial scale associated with the material and the process. During the charge/discharge cycles of nanoparticulate $LiFePO_4$ electrodes, phase separation inside the particles can be hindered even when a thermodynamic driving force for phase separation exists. In such cases, particles may (de)lithiate via a process referred to as interparticle phase separation, which involves Li redistribution between particles. The role of interparticle Li transport and multiparticle (de)lithiation kinetics could be the key to understand these processes. In this thesis, the complex dynamics of lithium iron phosphate is investigated based on the particle-level electrochemical dynamics (PLED) and the porous electrode theory (PET). PLED combined with a phase field model and the Smoothed Boundary Method is utilized to study the kinetic processes of interparticle phase separation. Using this approach, simple two-particle systems are examined to elucidate the detailed dynamics of the lithiation/delithiation process. Additionally, more realistic structures

consisting of many particles are utilized to analyze more complex cases of interparticle phase separation. The dependence of the electrochemical dynamics on (i) the exchange current density, (ii) the particle position, (iii) the presence of intraparticle phase separation, (iv) the particle size distribution, (v) the particle connectivity, and (vi) the equilibrium potential are elucidated. Simulations based on PET are employed to examine the overall behavior of the cell; these simulations elucidate the position dependence of the electrochemical dynamics on a coin-cell battery experimentally mapped. This thesis presents a comprehensive study on the interactions between $LiFePO_4$ nanoparticles and their effect on battery performance.

CHAPTER I

INTRODUCTION

1.1 General Background

Li-ion batteries have the potential to revolutionize the transportation and electric utilities technologies. For deployment on a large scale, Li-ion battery systems must be inexpensive and safe. To ensure the long-term safety and reliability of Li-ion battery systems, special attention is required to avoid accelerating the degradation of the material and, at worst, thermal runaway. Solving this problem requires a detailed understanding of the relationship between the battery's measurable properties (voltage, charge/discharge history, etc.) and the state of charge (SOC) of the individual particles in the electrode. Understanding this relationship can be particularly challenging in nanoparticulate materials (i.e., those composed of particles with a size $< \sim$100 nm) because their dynamics may differ from those of materials comprising larger particles. Furthermore, studying these materials is complicated by their small size and rapid transformation.

In electrode materials that remain in a single phase at equilibrium with respect to the Li concentration for the relevant cycling range (as in $LiTiS_2$ [4]), a thermodynamic driving force homogenizes the Li concentration among all active particles as well as within each particle. In these cases, the voltage reading across the cell reflects particles' SOC. However, for phase-separating systems, in which Li-poor and Li-rich phases are thermodynamically more stable than a uniform mixture, the interactions

between particles are much more complex. In such cases, particles in the electrode can coexist in equilibrium at very different SOCs and in many different configurations in a narrow potential range [5, 1]. Interest in phase-separating electrode materials has primarily been driven by the promising performance of nanoparticulate lithium iron phosphate, $LiFePO_4$ (LFP). LFP was first explored by Padhi et al. as a battery cathode in 1997 [6] and was not initially considered a suitable electrode material upon its discovery due to its low ionic diffusivity and electronic conductivity. This difficulty has been overcome by nanosizing particles [7], carbon coating [8], and doping with other metallic cations [9].

Although phase separation in nano-LFP particles has been observed in-situ during chemical lithiation [10] and ex-situ after electrochemical lithiation [11], it remains unclear whether phase separation occurs during normal operation of a battery, and if so, how the phase separation proceeds. This is because phase transformation during chemical lithiation can differ from that during electrochemical lithiation and Li distribution may evolve before ex-situ measurements are performed.

Many models have been proposed for the phase-transformation path. Several models have proposed different paths for "intraparticle phase separation" (i.e., phase separation inside the particle), such as the shrinking core [12], domino-cascade model [13], and amorphous transition [14], among others [15, 16]. Other models have proposed that intraparticle phase separation is prevented and that particles therefore remain homogeneous without nucleation. Meethong et al. [17] and Wagemaker et al. [18] proposed that non-bulk thermodynamics, such as surface energy and coherency stress, may suppress phase separation in nanoparticles with sizes smaller than 15-20 nm. Malik et al. [19] proposed that nucleation of the second phase in particles may not be feasible and that particles transform through a non-equilibrium solid solution path. Bai et al. [20] proposed that phase separation occurs at low currents, while a sufficiently large current suppresses phase transformation. They approximated that

the threshold may be in the range of 0.3C to 4.5C. Note that this range is comparable to the C-rates associated with many batteries applications including electric vehicles and portable electronics.

Despite the disagreement on the phase-transformation path at the individual particle level, there is a consensus that LFP particles transform inhomogeneously and non-concurrently [11, 21, 22]. For example, Chueh et al. [11] found that only ∼2 % of the particles react simultaneously at a 1C rate. Dreyer et al. [5] explained the strong inhomogeneity of the transformation of the particles by proposing that Li is redistributed between particles during phase transformation. When the particles are nanosized, Li can be easily redistributed between the nanoparticles to generate stable phases among the nanoparticles without the energy penalty of interface formation (i.e., they undergo "interparticle phase separation" [19]). In LFP electrodes, many particles ($\sim 10^{10}$ - 10^{17})[5] are interconnected ionically (through the electrolyte) and electronically (through carbon-coating, carbon black, or particle-particle contact). Therefore, a particle network is formed in which Li can be transported not only between the cathode and the anode but also between the active particles within the cathode. Given the driving force toward interparticle phase separation and the network of active particles in which Li can be redistributed, particles transform sequentially in the slow charging/discharging limit [5]. Thus, at any given time, a small fraction of particles in the electrode is lithiating (during discharge) or delithiating (during charge) and sustains the cell current. Consequently, the cell voltage does not reflect the SOC for the individual particles because the cell voltage also depends on additional factors, such as charge and discharge history [23], particle size distribution, and cathode architecture (which determines how the particles are interconnected) [1, 24]. The interparticle Li redistribution has been experimentally verified in LFP nanoparticles by Lee et al. [25]. They showed that when fully delithiated smaller particles are relaxed near lithiated larger particles, the smaller particles

lithiate by absorbing Li from the larger particles. Even though Li redistribution has been verified, how it occurs during battery operation has not been addressed in the literature and is the central subject of this thesis.

1.2 Research Objectives

In this thesis, we focus on the interactions between particles. We primarily consider the case where particles transform via a metastable solid solution because it allows us to efficiently analyze the interactions between many particles. In Chapter IV, we explore the applicability of the results from the solid solution model by comparing the results against those from phase separating cases. There, we also show that the dynamics can change both quantitatively and qualitatively when phase separation within a particle is suppressed in one particle, but not in the other.

Our work reveals detailed electrochemical dynamics at the individual particle level and extends to the collective behavior of many particles in an electrode. We specifically focus on the manner in which interparticle phase separation is affected by (1) particle location, (2) the exchange current density, (3) particle size, (4) the interaction with phase-separated particles, (5) particle interconnectivity, and (6) size dependence of the equilibrium potential. Throughout the thesis, several configurations are used to study different aspects of the particle interactions. Our simulations indicate that interparticle interactions are significant at the lower applied currents examined, which produce sudden increases and decreases in the voltage profile, while sufficiently high current ($\sim$1C rate for the parameters here used) suppresses these interactions. Although this work focuses on the charge/discharge behavior of nanoparticulate LFP, similar dynamics may be expected in other nanoparticulate materials that have tendency for phase separation, such as nanoparticles for hydrogen storage [26, 27] and nano-$LiMnPO_4$ [25]).

1.3 Qualitative Description of Charge-Discharge Process

In this thesis, we focus on the dynamics of nanoparticulate LFP cathodes. However, to facilitate the explanation of their dynamics, we first perform two auxiliary descriptions: First we briefly describe the general dynamics of an entire battery. Second, we discuss a simple case of the charge/discharge of a cathode in which Li remains as a solid solution. After these two descriptions, the dynamics of LFP are described.

1.3.1 Process overview

Li-ion batteries store and release energy by transferring Li between the anode and cathode, separated by a separator. Figure 1.1 shows the configuration and the charge-discharge process.

The process of charging/discharging the battery involves Li transport through the electrolyte and electrodes, electron transport through the microstructure, and electrochemical reactions between ions and electrons at the electrode-electrolyte interfaces. During battery charging (Fig. 1.1(a)), the Li in the cathode particles undergoes an electrochemical reaction on the particle surface to form a positively charged ion (cation) and an electron. The cations dissolve in the electrolyte, where negative ions (anions) are also present. The cations are transported from the cathode to the anode through the porous separator. Simultaneously, the electrons are transported through the conducting phase and current collector to the external circuit and ultimately to the anode. At the anode-electrolyte interface, the ions and electrons undergo another electrochemical reaction and recombine. The same process occurs during discharge in the opposite direction; see Fig. 1.1(b).

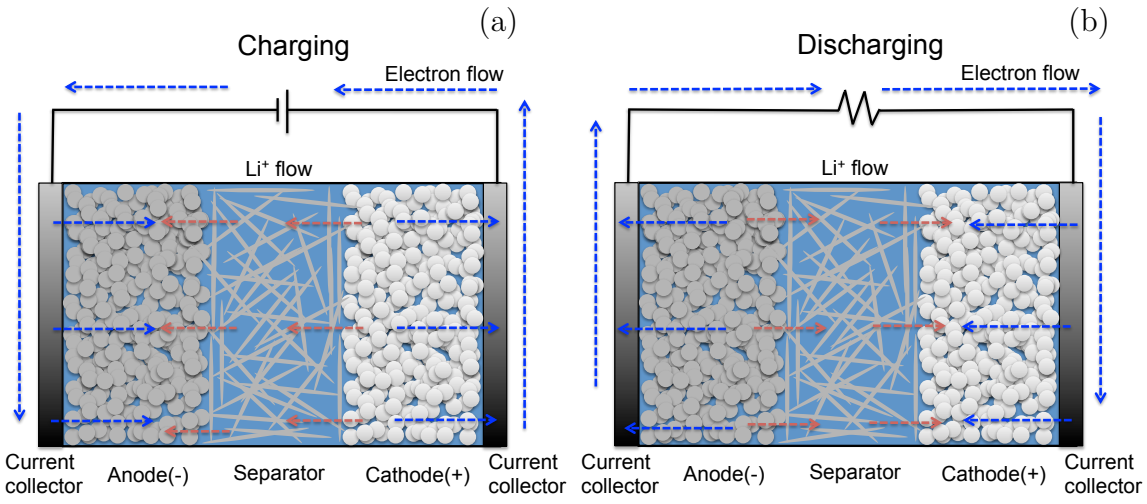

Figure 1.1: Schematic of a cell configuration as well as the (a) charge and (b) discharge process.

1.3.2 Cathode dynamics with solid solution

In many cathode materials, such as $LiCoO_2$, $LiMn_2O_4$, and $Li(Ni,Co,Mn)O_2$, Li forms solid solutions in a wide composition range [1]. In this section, we provide a simplified description of the general charge/discharge dynamics observed for such cases. We first describe the driving force for concentration evolution in the particles and for the reaction kinetics. In cathode particles in which Li forms a solid solution, the free energy of Li, f, is a single-well function; i.e., it only has one minimum value. An illustration of such a free energy is presented in Fig. 1.2. From the free energy, the particle chemical potential, μ_p, can be obtained. It is defined as the partial derivative of free energy with respect to the Li site fraction, X_p (plus other non-bulk terms, μ_{nb}):

$$\mu_p = \frac{\partial f}{\partial X_p} + \mu_{nb} \tag{1.1}$$

Figure 1.3 shows the chemical potential based on the free energy function presented in Fig. 1.2. The chemical potential determines the concentration evolution (assuming uniform electrostatic potential). Li tends to migrate from regions of high chemical potential to regions of low chemical potential. Given a monotonically increasing

chemical potential, as in this case, Li always has a driving force to migrate from regions of high concentration to regions of low concentration. Thus, the Li concentration tends to become homogeneous throughout the cathode particles.

The reaction kinetics of the cathode particles depends on the equilibrium potential and the potential difference across the particle-electrolyte interface, $\Delta\phi$, which equals the applied potential for the case of uniform electrostatic potentials. As described by its name, the equilibrium potential, ϕ_{eq}, is the voltage at which a particle remains in equilibrium (i.e., at a constant SOC) [28]. The equilibrium potential depends on both the chemical potential of Li in the cathode and the chemical potential of Li in the anode. However, when Li metal is considered as the anode (as in this work), the chemical potential of Li in the anode becomes constant. For the purpose of this introduction, we take the equilibrium potential to be proportional to $-\mu_p$, which is shown in Fig. 1.4.

We now describe a simple case in which four particles are lithiated (discharged). We assume that the particles have the same size, the electrolyte concentration is uniform and that there are no gradients in the electrostatic potential of the particles or electrolyte. For such a simple case, the particles react uniformly. Figures 1.5(a)-(c) show the lithiation (discharge) process for a set of four particles, and (d)-(f) show the corresponding voltage. The driving force toward lithiation can be approximated as the difference between the equilibrium potential and $\Delta\phi$. Initially the particles are nearly fully delithiated and have a high voltage. To lithiate the particles, the voltage is constantly lowered as the particles depth of discharge (DOD=1-SOC) increases. All the particles have the same driving force toward lithiation and thus lithiate uniformly. When the particles reach a nearly fully lithiated state, the voltage reaches a minimum value. In a more realistic cell, the concentration in the particles would not be uniform, and the order of reaction of the particles would depend on their size, position, etc.

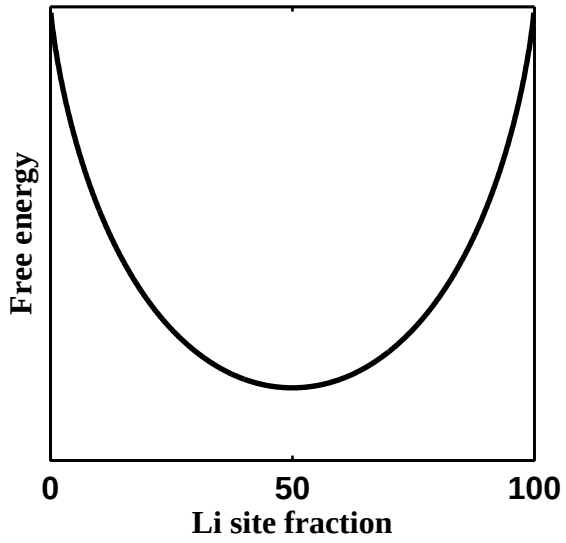

Figure 1.2: Example of a single-well free energy function.

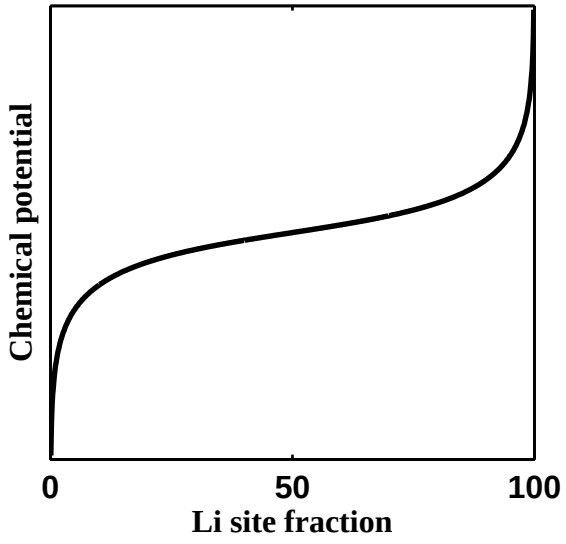

Figure 1.3: Example of the chemical potential that results from the free energy shown in Fig. 1.2.

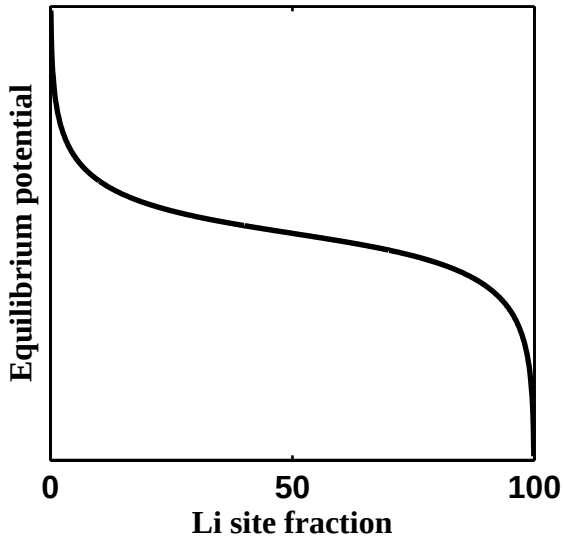

Figure 1.4: Example of the equilibrium potential from the free energy shown in Fig. 1.2.

1.3.3 LFP cathode dynamics: driving force toward phase separation

Now, we introduce the free energy, chemical potential, and equilibrium potential that govern the kinetics of Li transport and electrochemistry for LFP. LFP has a thermodynamic driving force to phase separate into Li-rich and a Li-poor phases [29]. The free energy function, f, for this case corresponds to a double-well function, which is shown in Fig. 1.6. The free energy of this system is minimized when some regions of the cathode become Li rich and others Li poor. The system in the concentration range between the inflection points of the free energy curve is unstable; the concentration values at these inflection points are called the spinodal points. Figure 1.7 shows the chemical potential that results from the free energy in Fig. 1.6. In this figure, we also indicate the location of the spinodal points. The spinodal points correspond to the concentration values at which the chemical potential is at a local minimum or a local maximum. The spinodal point near a low concentration is referred to as the lower spinodal point, and the spinodal point near a high concentration is referred to as the higher spinodal point. Unlike the case with single-phase equilibrium, the chemical

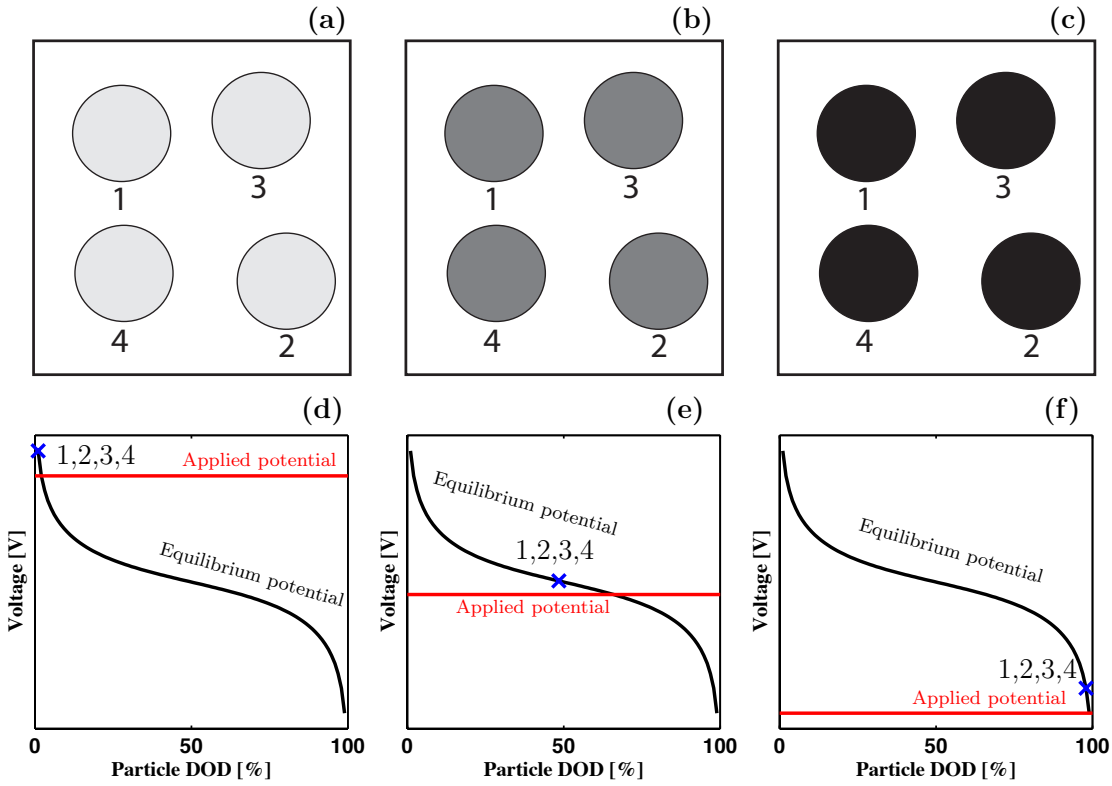

Figure 1.5: Schematic for the lithiation of four particles (assuming uniform electrostatic potentials). (a), (b) and (c) represent the particles during lithiation (the grayscale indicates the degree of lithiation, with darker gray indicating a higher Li concentration); (d), (e) and (f) indicate the applied voltage and the DOD of the particles. When the equilibrium potential is monotonic the particles tend to react uniformly.

potential is non-monotonic with increasing concentration. Figure 1.8 presents the equilibrium potential that results from the chemical potential from Fig. 1.7, which differs by a sign, a constant factor and a shift; we here refer to the region between the spinodal points as the "inverted potential range."

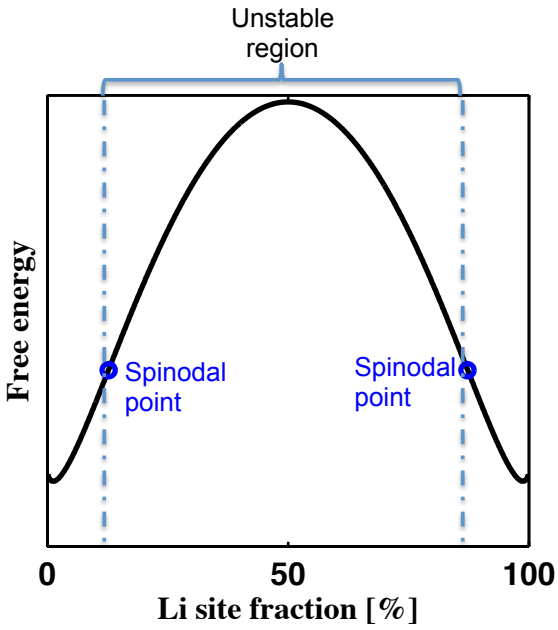

Figure 1.6: Example of a double-well free energy function.

We now detail the discharge (lithiation) process for nanoparticulate LFP cathodes; the description is based on Ref. [1]. We here assume that phase separation cannot occur inside the particles and that instead particles remain monophasic during their phase transformation [19]. In Chapter IV, we show that the results presented in this thesis are similar even if this assumption is removed. Figure 1.9 presents a schematic of the process at the low current limit. The driving force for Li insertion into the particles is the difference between the equilibrium potential and $\Delta\phi$. When $\Delta\phi$ is lower than the equilibrium potential, the particles are driven to lithiate (discharge). Materials with a tendency for phase separation, such as LFP, have a non-monotonic equilibrium potential, similar to those shown in Figs. 1.8 and 1.9(d)-(f).

In Fig. 1.9(d), we show the initial voltage, which is considered approximately equal

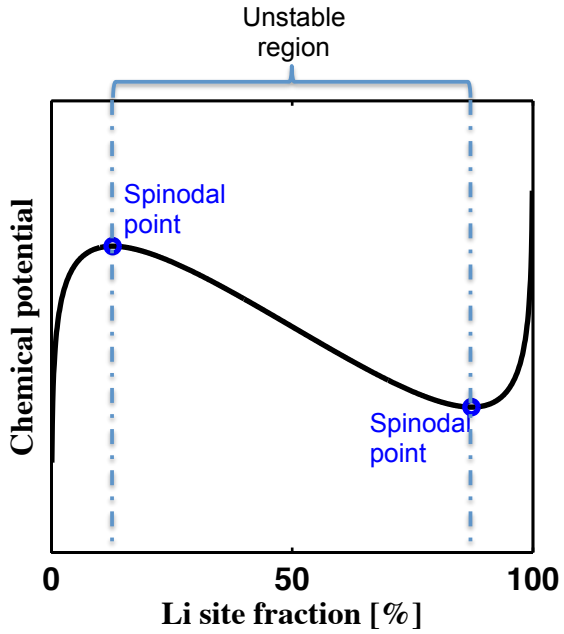

Figure 1.7: Example of the chemical potential that results from the free energy shown in Fig. 1.6.

to $\Delta\phi$ for the purpose of this description. Upon discharge, the applied potential across the cell is continually lowered to drive Li insertion. Shortly after the process begins, the lower spinodal point voltage is reached (Fig. 1.9(e)). Due to the non-monotonic nature of the equilibrium potential with respect to Li concentration, beyond the lower spinodal point, the driving force for additional Li insertion begins to increase. This effect can be observed in Fig. 1.9(e) or (f), where the difference between the equilibrium and applied potentials is larger at a higher particle DOD. When one of the particles reaches the spinodal point, the particle begins to undergo rapid lithiation, while the other particles experience some Li loss, as discussed in the next paragraph. The order in which particles react is affected by several factors, such as the particle size, location, and connectivity; this will be discussed throughout the thesis. Once the particle is nearly fully lithiated, another particle begins to lithiate (Fig. 1.9(c) and (f)). Thus, the particles lithiate sequentially. The delithiation process is similar, except for that particles are initially at the lithiated state and Li is extracted from

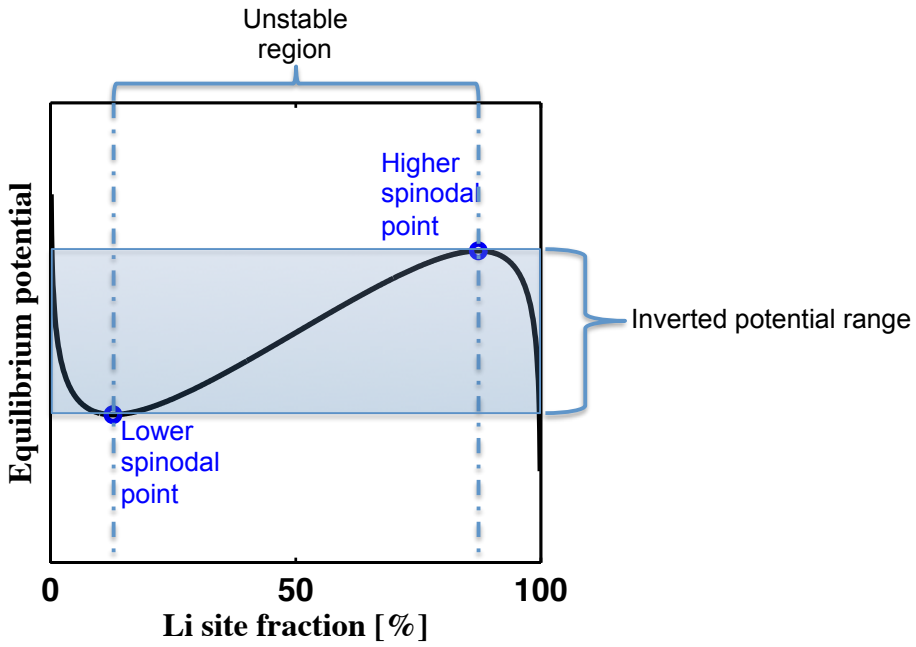

Figure 1.8: Example of the equilibrium potential from the free energy shown in Fig. 1.6.

the system during the process. These processes, along with the rate effects, will be explained in more detail in Chapter III and IV.

In an electrode with many interacting active particles, we must consider a driving force for interparticle Li redistribution. Redistribution is driven by the higher free energy of the particles at an intermediate Li concentration compared to a mixture of particles in Li-rich and Li-poor phases. As will be shown in detail in Chapter III, redistribution is concurrent with rapid particle lithiation/delithiation. We schematize this process in Fig. 1.10 for a system containing four particles that are at an intermediate concentration. In this example, the particles reach equilibrium by redistributing Li. Li redistribution among particles is triggered when some particles begin accelerated lithiation, which causes a voltage increase. This voltage increase produces a driving force for particles that are not undergoing rapid lithiation to delithiate. Thus, particles release or absorb Li and tend to transform into either a Li-poor or a Li-rich phase.

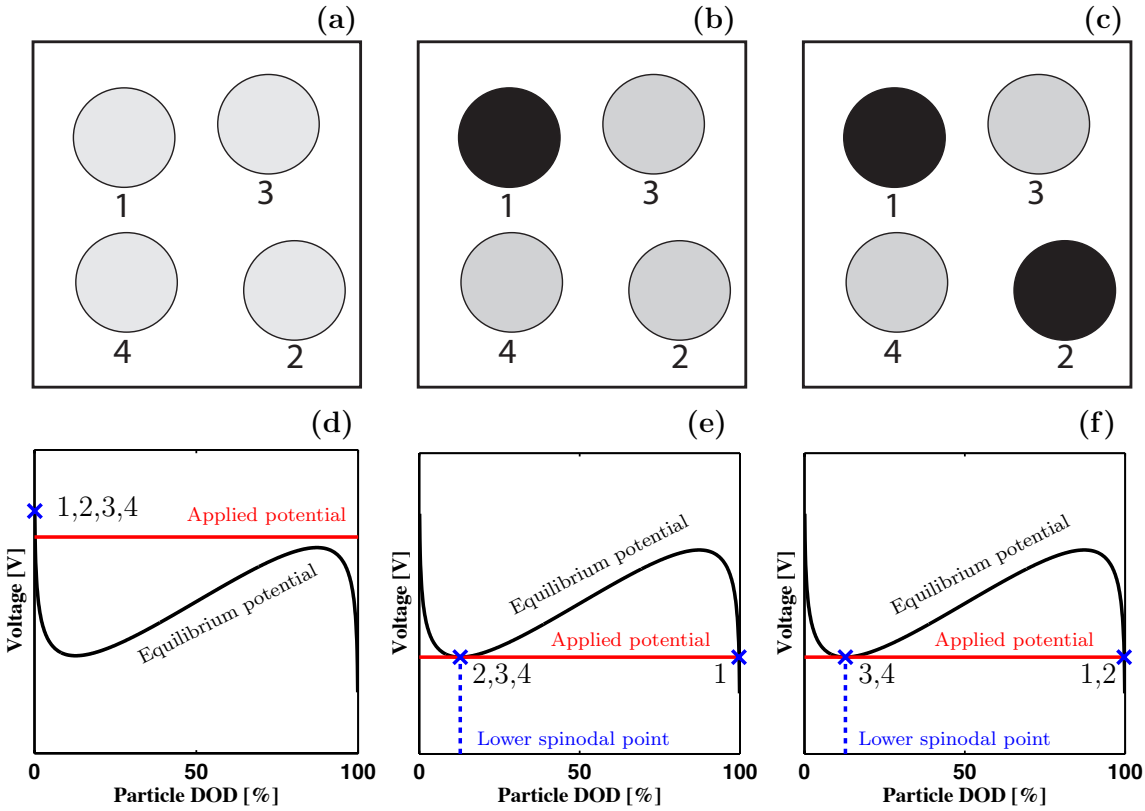

Figure 1.9: Schematic for sequential transformation of four particles neglecting inter-particle redistribution; based on a schematic from Ref. [1] (assuming that the applied potential approximates the local potential difference across the particle-electrolyte interface, $\Delta\phi$). (a), (b) and (c) represent the particles during lithiation (the grayscale indicates the degree of lithiation, with darker gray indicating a higher Li concentration); (d), (e) and (f) indicate the applied voltage and the DOD of the particles. (a) and (d) At the beginning of the process, the voltage is constantly lowered to lithiate the particles. (b) and (e) When the particles reach the spinodal point, the particles begin to lithiate sequentially due to the increasing driving force they incur due to the non-monotonic shape of the equilibrium potential. (c) and (f) The process continues until all particles are fully transformed.

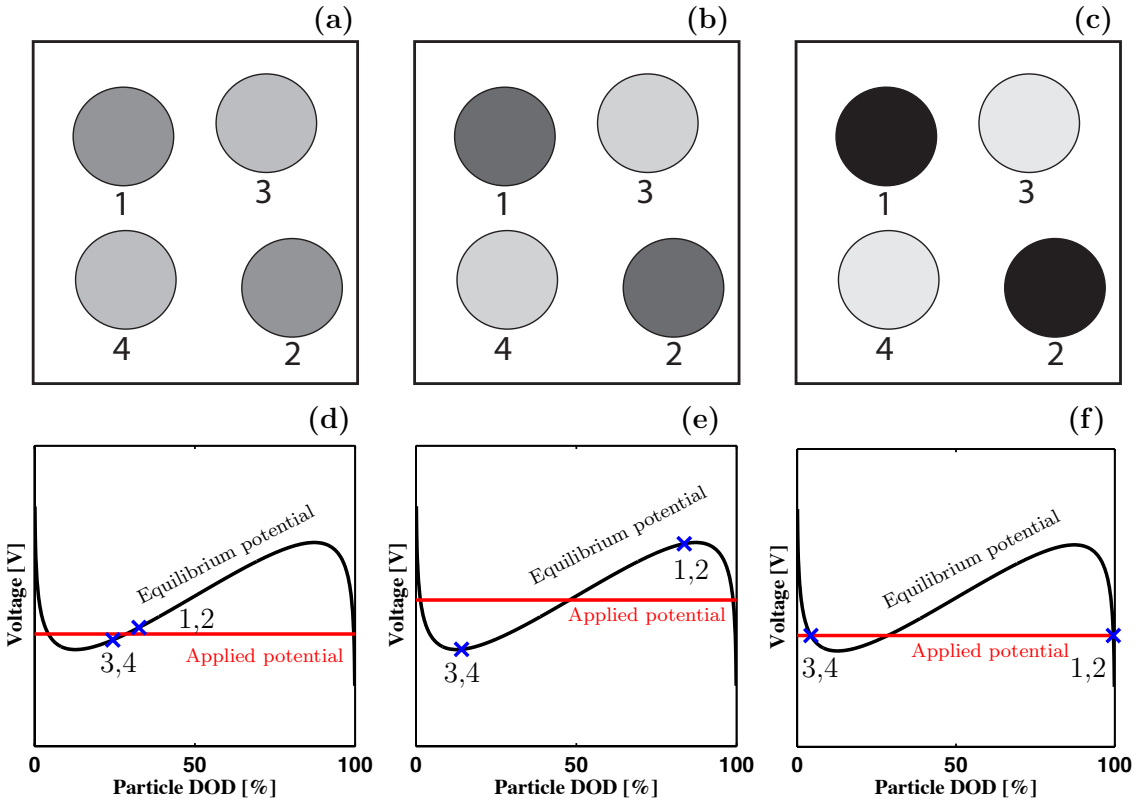

Figure 1.10: Schematic of Li redistribution between four particles via a reaction (assuming that the applied potential approximates $\Delta\phi$). (a), (b) and (c) represent the particles during the process (the grayscale indicates the degree of lithiation, with darker gray indicating a higher Li concentration); (d), (e) and (f) indicate the voltage applied to and the DOD of the particles. (a) and (d) A small difference in the concentration determines which particles extract Li and which particles absorb Li. (b) and (e) During redistribution, the applied voltage fluctuates to equilibrate insertion and extraction. (c) and (f) The process ends when the particles reach equilibrium in a Li-poor or a Li-rich phase.

1.4 Modeling Approach

The charge/discharge process can be modeled and simulated at different length scales. At the continuum level (i.e., discrete nature of atoms are not considered), there are two distinct length scales. The microscale is used to refer to the scale at which microstructures consist of various phases such as the active particles and electrolyte, while the macroscale refers to the scale at which microstructural details are ignored.

At the microscale, the dynamics are modeled explicitly considering the particle geometries. We refer to the dynamics at this length scale as particle-level electrochemical dynamics (PLED). The finite element method is conventionally used to represent the material micro-structures, as in Ref. [30, 31]. However, a challenge in applying this method arises when performing three-dimensional (3D) simulations. The battery electrode microstructures are highly complex; therefore, generating a 3D mesh is a challenging and time-consuming task especially for realistic microstructures. In this thesis, we use an alternative approach to account for electrode structures in a microscale model. We apply the smoothed boundary method (SBM), which was initially introduced by Bueno-Orovio et al. [32, 33, 34] and further developed by Yu et al. [2]. The SBM involves modification of the partial differential equations using mathematical identities and has been applied in studies of structural evolution, with and without contact angles, and diffusion. The PLED equations in both their conventional and SBM form are presented in Chapter II.

The aforementioned electrochemical dynamics are also modeled at the macroscale using effective parameters, such as conductivity and diffusivity [28], which can be calculated from coarse-grained microstructural characteristics such as porosity and tortuosity [35]. This type of model is referred to as porous electrode theory (PET) model. PET models are computationally efficient, often capture the dynamic nature of the charge/discharge process in a relatively simple description over the cell scale, and can be directly compared with experimental data. However, a disadvantage is

that these models only consider average properties and therefore are not applicable for investigations of the effects of micro-structural details. The PET formulation and simulations are described in Chapter VII (and briefly in Chapter III).

1.5 Thesis Outline

This dissertation contains nine chapters: (I) Introduction, (II) PLED Model, (III)-(VI) PLED Results, (VII) PET Model and Results, (VIII) Summary, Discussion and Future Work, and (IX) Conclusion.

In Chapter II, we describe the PLED model. We present the governing equations in their conventional formulation, derive the SBM formulation, and present the numerical methods employed to solve the equations.

In Chapter III, we present the charge/discharge simulation results for systems of (i) two particles and (ii) 26 particles of equal size. We focus on the dependence of the particles' order of reaction on their position. In addition, we study the effect of an anisotropic exchange current density on the lithiation-delithiation dynamics. This chapter is based on the published work "Particle-Level Modeling of the Charge-Discharge Behavior of Nanoparticulate Phase-Separating Li-Ion Battery Electrodes" [36].

In Chapter IV, we study the dependence of particle interactions on the presence of intraparticle phase separation. Here, we utilize a configuration of two particles with different sizes to compare the interactions between the particles for three cases: (i) when phase separation is suppressed in both particles, (ii) when phase separation is not suppressed in either particle, and (iii) when phase separation is suppressed only in one particle but not in the other. This chapter is based on a publication in preparation, "Kinetics of Interparticle Phase Separation" [37].

In Chapter V, we study the dependence of inter-particle interactions on connectivity. Here, we consider two agglomerates: one with 65 particles in which the particles

are not in direct contact with others and one with 200 particles in which they are in direct contact with neighboring particles. The 65-particle agglomerate represents an ideal structure with what we termed as "homogeneous" connectivity between particles, while the 200-particle corresponds to a more realistic structure with "heterogeneous" connectivity. This chapter is based on the published work "Architecture Dependence on the Dynamics of Nano-$LiFePO_4$ Electrodes" [38].

In Chapter VI, we study the effect of a size-dependent equilibrium potential on the particle interactions. We employ the two-particle cell from Chapter IV and the 65-particle agglomerate from Chapter V to analyze the change in dynamics when a size-dependent equilibrium potential is considered in the model. This chapter is based on a publication in preparation, "Effect of a Size-Dependent Equilibrium Potential on Nano-$LiFePO_4$ Particle Interactions" [39].

In Chapter VII, we present the PET model and its corresponding simulation results. We here employ a three-dimensional configuration representative of a coin cell battery. These simulations provide insights into experiments that map the position dependence of the order of reaction of the particles within the cathode. Additionally, sensitivity analyses are performed on the particle-size distribution and the electrode porosity. This chapter is based on a publication in preparation, "Mapping the Inhomogeneous Electrochemical Reaction Through Porous $LiFePO_4$-Electrodes in a Standard Coin Cell Battery" [40].

In Chapter VIII we present the summary, discussion and future work. In Chapter IX, we conclude this thesis.

CHAPTER II

FORMULATION OF PARTICLE-LEVEL ELECTROCHEMICAL DYNAMICS

We present a model used to study the dynamics of the electrochemical process; this model is used throughout Chapters III - VI, with certain variations that are identified at the beginning of each chapter. The porous electrode model is described in Chapter VII. In this chapter, we first present the conventional electrochemical formulation, then we derive the smoothed boundary method (SBM) formulation; finally, we describe the numerical methods used to solve the governing equations.

2.1 Conventional Formulation

Lithium transport in the cathode particles is modeled using either Fick's diffusion law or the Cahn-Hilliard equation. We assume that the cathode particles are electrically well connected to the current collector through a carbon black network, and consequently, we assume that the electrostatic potential is uniform throughout the entire cathode. We assume electroneutrality throughout the electrolyte, allowing calculation of the electrolyte electrostatic potential based on the charge conservation conditions. The lithium ion transport into the electrolyte is driven by the gradients of concentration and electrostatic potential, which correspond to diffusion and migration, respectively; here, they are modeled using the Nernst-Planck equation. The Li ion reaction with electrons is modeled using the Butler-Volmer equation.

2.1.1 Transport within the particles

We now present the equations that govern Li transport within the particles. We first introduce Cahn-Hilliard equation and then Fick's diffusion equation. A flux of Li within the particle, $\mathbf{J}_p$, can originate from gradients in the chemical potential of Li, μ_p, within the particle,

$$\mathbf{J}_p = -M_p \nabla \mu_p, \tag{2.1}$$

where M_p is the mobility of Li in the particles. Here, we only account for fluxes originating from concentration gradients, while they can also arise due to the presence of an electrostatic field (i.e., migration). Using the mass conservation law, the concentration evolution can be defined as the divergence of a flux within the bulk of the cathode particle, V_p,

$$\frac{\partial C_p}{\partial t} = -\nabla \cdot \mathbf{J}_p \in V_p, \tag{2.2}$$

where C_p is the concentration of Li in the particles, and t is time. To model concentration evolution in phase-separating systems, the Cahn-Hilliard equation [41] is commonly employed. Combining Eq. (2.1) and Eq. (2.2) we can obtain the Cahn-Hilliard equation,

$$\frac{\partial C_p}{\partial t} = \nabla \cdot (M_p \nabla \mu_p) = \nabla \cdot \left[M_p \nabla \left(\mu_b - \nabla \cdot \left(\frac{\boldsymbol{\kappa}}{\rho^2} \nabla C_p \right) \right) \right] \in V_p, \tag{2.3}$$

where $\boldsymbol{\kappa}$ is the energy gradient coefficient, M_p is the Li mobility, and μ_b is the bulk term for the chemical potential. The term $\nabla \cdot \left(\frac{\boldsymbol{\kappa}}{\rho^2} \nabla C_p \right)$ accounts for the energy penalty of having an interface within the particle, where ρ is the Li concentration at which the Li site fraction, X_p is equal to one ($X_p = C_p/\rho$). The different models employed to approximate the chemical potential are specified in each chapter.

When the concentration is proportional to the chemical potential, which is the case for ideal mixtures, a flux can be defined as a function of the concentration instead of the chemical potential. Fick's first law relates that a flux results from gradients in

the concentration,

$$\mathbf{J}_p = -D_p \nabla C_p, \tag{2.4}$$

where D_p is the diffusivity of Li in the particles. Fick's second law relates the change in concentration over time as the divergence of the flux defined in Eq. (2.4),

$$\frac{\partial C_p}{\partial t} = \nabla \cdot (D_p \nabla C_p) \in V_p. \tag{2.5}$$

As mentioned in Chapter I, in most chapters (except Chapter IV), we assume no phase separation within the individual particles. This assumption allows us to focus solely on the interparticle phase separation dynamics as the collective behavior of an electrode consisting of many nanoparticles. For $LiFePO_4$ (LFP), there is a consensus that phase separation inside the particles is thermodynamically suppressed in particles smaller than 20 nm [42, 17, 18]; furthermore, phase separation can also be kinetically suppressed in larger particles during the charge/discharge process [43]. For simplicity and numerical efficiency, we model the concentration evolution in the particle using Fick's law of diffusion (Eq. (2.5)) and not the Cahn-Hilliard equation (Eq. (2.3)). For the cases examined in this work, the Li concentration in the particles is nearly uniform, but we employ this model to retain generality. The boundary condition at the particle-electrolyte interface is determined by the reaction rate, which accounts for Li (de)intercalation:

$$\vec{n} \cdot \mathbf{J} = r_{Li} \in A, \tag{2.6}$$

where r_{Li} is the reaction rate, $\vec{n}$ represents the unit normal vector in the direction from the electrolyte to the particle, and $\mathbf{J}$ is the flux at the particle-electrolyte interfacial region, A.

2.1.2 Electrostatic potential in the electrolyte

Here, we describe the equations that govern electrostatic potential in the electrolyte. We use the dilute solution model for diffusion in a binary electrolyte in which one

cationic and one anionic species are present in a neutral solvent, as described in the textbook by Newman and Thomas-Alyea [44].

Transporting a charged species through the electrolyte produces an ionic current, which can be decomposed into terms that correspond to diffusion and migration. The current density vector, $\mathbf{i}$, accounts for both diffusion and migration and is given by [44]:

$$\mathbf{i} = -z_+ \upsilon_+ F \left[\frac{F}{RT}(z_+ D_+ - z_- D_-) C_e \nabla \phi_e + (D_+ - D_-) \nabla C_e \right], \tag{2.7}$$

where υ_+ is the number of cations produced by the electrolyte dissociation, F is Faraday's constant, R is the gas constant, T is the absolute temperature, and C_e and ϕ_e are the concentration and electrostatic potential of the electrolyte, respectively. Furthermore, z_i is the charge number, and D_i is the diffusivity of ith species.

Based on the charge conservation condition, the divergence of the current equals zero in the absence of a source or sink (or, equivalently, in the absence of a reaction), which is the case for the locations of the electrolyte away from the interfaces:

$$-\frac{\nabla \cdot \mathbf{i}}{z_+ \upsilon_+ F} = \nabla \cdot \left[\frac{F}{RT}(z_+ D_+ - z_- D_-) C_e \nabla \phi_e \right] + \nabla \cdot [(D_+ - D_-) \nabla C_e] = 0 \in V_e. \tag{2.8a}$$

where V_e represents the bulk of the electrolyte domain. The boundary condition at the particle-electrolyte interface is determined based on the reaction rate,

$$\frac{\vec{n} \cdot \mathbf{i}}{z_+ \upsilon_+ F} = \frac{r_{Li}}{\upsilon_+} \in A. \tag{2.8b}$$

Equations (2.8a) and (2.8b) are solved to obtain the electrostatic potential in the electrolyte under the flux boundary condition imposed at the particle-electrolyte interfaces. The electrostatic potential is used in the Butler-Volmer equation to determine the reaction rate. On the anode-electrolyte boundary, the reference value of 0 V is set as the electrostatic potential of the electrolyte.

2.1.3 Transport in the electrolyte

The equations that govern transport in the electrolyte are now described following the derivation of Ref. [44]. The Nernst-Planck equations for the concentrations of cation, C_+, and anion, C_-, when there is no convection can be expressed as

$$\frac{\partial C_+}{\partial t} = \nabla \cdot (z_+ u_+ F C_+ \nabla \phi_e) + \nabla \cdot (D_+ \nabla C_+) \in V_e, \tag{2.9a}$$

$$\frac{\partial C_-}{\partial t} = \nabla \cdot (z_- u_- F C_- \nabla \phi_e) + \nabla \cdot (D_- \nabla C_-) \in V_e. \tag{2.9b}$$

Here, u_i is the transport mobility of the species i. The dissociation relationship relates the electrolyte concentration and anion/cation concentrations:

$$C_e = \frac{C_+}{\upsilon_+} = \frac{C_-}{\upsilon_-}, \tag{2.10}$$

where C_e is the electrolyte concentration and υ_- is the dissociation number of the anion. The dissociation relationship is applied to both Eq. (2.9a) and Eq. (2.9b) to express these equations in terms of C_e,

$$\frac{\partial C_e}{\partial t} = \nabla \cdot (z_+ u_+ F C_e \nabla \phi_e) + \nabla \cdot (D_+ \nabla C_e) = \nabla \cdot (z_- u_- F C_e \nabla \phi_e) + \nabla \cdot (D_- \nabla C_e) \in V_e. \tag{2.11}$$

The following two substitutions are then performed: (1) The term $F C_e \nabla \phi_e$ is expressed in terms of the current density vector and concentration gradients using Eq. (2.7),

$$F C_e \nabla \phi_e = \frac{-RT\mathbf{i}}{z_+ \upsilon_+ F (z_+ D_+ - z_- D_-)} - \frac{RT(D_+ - D_-)}{(z_+ D_+ - z_- D_-)} \nabla C_e. \tag{2.12}$$

(2) The mobilities are substituted by diffusivities using the Nernst-Einstein equation.

$$D_i = RT u_i. \tag{2.13}$$

Thus, we obtain an equation governing the electrolyte concentration independent of the electrostatic potential:

$$\frac{\partial C_e}{\partial t} = \nabla \cdot \left(D_{amb} \nabla C_e \right) - \nabla \cdot \left(\frac{t_+ \mathbf{i}}{z_+ \upsilon_+ F} \right) \in V_e, \tag{2.14}$$

where D_{amb} is the ambipolar diffusion coefficient, and t_+ is the transference number of the cation. The ambipolar diffusion coefficient is an effective diffusion coefficient that accounts for both the diffusion and migration of the electrolyte and is defined as

$$D_{amb} = \frac{D_+ D_- (z_+ - z_-)}{(z_+ D_+ - z_- D_-)}, \tag{2.15}$$

and the transference number of the cation is defined as:

$$t_+ = \frac{z_+ D_+}{z_+ D_+ + z_- D_-}. \tag{2.16}$$

The second term of Eq. (2.14) is then expanded to obtain the following,

$$\frac{\partial C_e}{\partial t} = \nabla \cdot \left(D_{amb} \nabla C_e \right) - \left(\frac{\mathbf{i} \cdot \nabla t_+}{z_+ \upsilon_+ F} \right) - \left(\frac{t_+ \nabla \cdot \mathbf{i}}{z_+ \upsilon_+ F} \right) \in V_e. \tag{2.17}$$

Using the charge conservation condition (Eq. (2.8a)), Eq. (2.17) is simplified into

$$\frac{\partial C_e}{\partial t} = \nabla \cdot \left(D_{amb} \nabla C_e \right) - \left(\frac{\mathbf{i} \cdot \nabla t_+}{z_+ \upsilon_+ F} \right) \in V_e, \tag{2.18}$$

in the electrolyte regions away from the interfaces.

At the boundary, a boundary condition similar to Eq. (2.6) is applied but with opposite sign. Furthermore, because the last term of the right-hand side (RHS) of Eq. (2.17) has a non-zero boundary condition (denoted by Eq. (2.8b)), the effective boundary condition becomes

$$\vec{n} \cdot \mathbf{J} = -(1 - t_+) \frac{r_{Li}}{\upsilon_+} \in A. \tag{2.19}$$

Note that the reaction rate is divided by υ_+ (using Eq. (2.10)) to denote the flux in moles of electrolyte. This reaction rate accounts for Li ion transfer to and from the

electrodes, similar to the equation used by Ferguson and Bazant [45].

Because the electrolyte was assumed to be electroneutral, the concentrations and total quantity of each ionic species (anions or cations) in the electrolyte are equal. The anions are considered inert; thus, the total quantity of both species in the electrolyte must remain constant. Therefore, as the Li reacts at the cathode particle surface, we assume that the corresponding amount of lithium reacts at the anode-electrolyte interface as follows:

$$\int_{A_A} \vec{n}_a \cdot \mathbf{J}_a dA = \frac{1}{S_A} \int_{A_r} (1 - t_+) r_{Li} dA, \tag{2.20}$$

where $\vec{n}_a$ is the unit normal vector pointing from the anode to the electrolyte, $\mathbf{J}_a$ is the flux at the anode-electrolyte boundary, A_A is the anode-electrolyte interface, A_r is the particle-electrolyte interfaces, and S_A is the total surface of the anode-electrolyte interface.

We neglect the effect of the double layers because, for the range of current considered here, electrolyte depletion is limited, and the concentrations remain high ($\sim$1M), which yield thin double layers. For models that account for double-layers/non-neutral electrolytes, see Refs. [46] and [47].

2.1.4 Reaction at the cathode particle-electrolyte interface

Now we show the derivation for the Butler-Volmer equation following Ref. [48]. This model is valid for reactions that involve only one electron and that occur in one step, which is the case for $LiFePO_4$.

The electrochemical reaction that takes place in the electrolyte-electrode interface of LFP can be defined as:

$$Li^+ + e^- + FePO_4 \underset{k_b}{\overset{k_f}{\rightleftharpoons}} LiFePO_4, \tag{2.21}$$

where k_f and k_b are the rates of forward and backward reaction respectively. The net

reaction, r_{net}, is defined as the forward reaction, r_f, minus the backward reaction, r_b,

$$r_{net} = r_f - r_b = k_f C_+^s - k_b C_p^s = \frac{i}{F}. \tag{2.22}$$

Here, C_+^s and C_p^s denote the surface concentration of Li in the electrolyte and in the particles, respectively. Furthermore, i is the current density, which is defined as positive in the direction from the electrolyte to the electrode. The rate constants k_f and k_b, can be written in an Arrhenius form,

$$k_f = A_f \exp(-\Delta G_c^{\ddagger}/RT), \tag{2.23a}$$

$$k_b = A_b \exp(-\Delta G_a^{\ddagger}/RT). \tag{2.23b}$$

$\Delta G_c^{\ddagger}$ is the standard free energy for activation of the cathodic reaction (forward reaction) and $\Delta G_a^{\ddagger}$ is the standard free energy for activation of the anodic reaction (backward reaction). A_f and A_b are frequency factors for the forward and backward reactions, respectively.

The interfacial potential difference, $\Delta\phi$, is defined as the potential of the electrode minus the potential of the electrolyte, ($\Delta\phi = \phi_p - \phi_e$). The formal potential ($\phi^{0'}$) is defined as the potential at which the rates of the forward reaction and the backward reaction are equal, when the bulk concentration of Li^+ in the electrolyte, C_+^b, and Li in the particles, C_p^b, are equal (here the superindex b denotes bulk). We denote $\Delta G_{0i}^{\ddagger}$ as the free energy at the condition at which the formal potential is defined. We can express $\Delta G_i^{\ddagger}$ for any applied potential as

$$\Delta G_c^{\ddagger} = \Delta G_{0c}^{\ddagger} + \alpha F(\Delta\phi - \phi^{0'}), \tag{2.24a}$$

$$\Delta G_a^{\ddagger} = \Delta G_{0a}^{\ddagger} - (1-\alpha) F(\Delta\phi - \phi^{0'}), \tag{2.24b}$$

where $\Delta G_0^{\ddagger}$ is the free energy reference to the formal potential and α is the transfer coefficient, which ranges from zero to one and accounts for the symmetry of the reaction energy landscape. Substituting Eqs. (2.23a) and (2.23b), into Eqs. (2.24a)

and (2.24b), respectively, we obtain:

$$k_f = A_f \exp(-\Delta G^{\ddagger}_{0c}/RT) \exp\left[-\frac{\alpha F}{RT}(\Delta\phi - \phi^{0'})\right], \tag{2.25a}$$

$$k_b = A_b \exp(-\Delta G^{\ddagger}_{0a}/RT) \exp\left[\frac{(1-\alpha) F}{RT}(\Delta\phi - \phi^{0'})\right]. \tag{2.25b}$$

At equilibrium and when $C^b_+ = C^b_p$, the interfacial potential drop is equal to the formal potential $\Delta\phi = \phi^{0'}$, and k_f becomes equal to k_b,

$$k_f = A_f \exp(-\Delta G^{\ddagger}_{0c}/RT) = k_b = A_b \exp(-\Delta G^{\ddagger}_{0a}/RT) = k_0, \tag{2.26}$$

which defines the standard rate constant, k_0.

Using Eq. (2.26), Eqs. (2.25a) and (2.25b) can be expressed as

$$k_f = k_0 \exp\left[-\frac{\alpha F}{RT}(\Delta\phi - \phi^{0'})\right], \tag{2.27a}$$

$$k_b = k_0 \exp\left[\frac{(1-\alpha) F}{RT}(\Delta\phi - \phi^{0'})\right], \tag{2.27b}$$

respectively. Inserting these expressions in Eq. (2.22) we obtain:

$$i = Fk^0\left[C^s_+ \exp\left(-\frac{\alpha F}{RT}(\Delta\phi - \phi^{0'})\right) - C^s_p \exp\left(\frac{(1-\alpha) F}{RT}(\Delta\phi - \phi^{0'})\right)\right]. \tag{2.28}$$

Now, Eq. (2.28) is simplified to obtain the Butler-Volmer equation. The equilibrium potential, E_{eq}, is defined as the potential at which the forward and backward reaction are equal but not necessarily at $C^b_+ = C^b_p$,

$$\phi_{eq} = \phi^{0'} + \frac{RT}{F} \ln \frac{C^b_+}{C^b_p}. \tag{2.29}$$

Considering the case of equilibrium, $i = 0$, in Eq. (2.28), the interfacial potential difference is equal to the equilibrium potential, $\Delta\phi = \phi_{eq}$, and the surface concentration is equal to the bulk concentration, $C^s_i = C^b_i$. Therefore, we obtain

$$Fk^0 C^b_+ \exp\left(-\frac{\alpha F}{RT}(\phi_{eq} - \phi^{0'})\right) = Fk^0 C^b_p \exp\left(\frac{(1-\alpha) F}{RT}(\phi_{eq} - \phi^{0'})\right) = i_0, \tag{2.30}$$

where i_0 is the exchange current density. Equation (2.29) can be rearranged to obtain

$$\exp\left(\frac{F}{RT}(\phi_{eq}-\phi^{0'})\right)=\frac{C_+^b}{C_p^b}, \tag{2.31}$$

which can be substituted back into Eq. (2.30) to obtain an expression for i_0,

$$i_0 = Fk^0 C_+^{b(1-\alpha)} C_p^{b(\alpha)}. \tag{2.32}$$

Dividing Eq. (2.28) by Eq. (2.32) results in

$$\frac{i}{i_0}=\frac{C_+^s}{C_+^{b(1-\alpha)}C_p^{b(\alpha)}}\exp\left(-\frac{\alpha F}{RT}(\Delta\phi-\phi^{0'})\right)-\frac{C_p^s}{C_+^{b(1-\alpha)}C_p^{b(\alpha)}}\exp\left(\frac{(1-\alpha)F}{RT}(\Delta\phi-\phi^{0'})\right), \tag{2.33}$$

which can be rearranged into

$$\frac{i}{i_0}=\frac{C_+^s}{C_+^b}\left(\frac{C_+^b}{C_p^b}\right)^{\alpha}\exp\left(-\frac{\alpha F}{RT}(\Delta\phi-\phi^{0'})\right)-\frac{C_p^s}{C_p^b}\left(\frac{C_+^b}{C_p^b}\right)^{-(1-\alpha)}\exp\left(\frac{(1-\alpha)F}{RT}(\Delta\phi-\phi^{0'})\right). \tag{2.34}$$

Substituting Eq. (2.31) into Eq. (2.34), we obtain

$$i=i_0\left[\frac{C_+^s}{C_+^b}\exp\left(-\frac{\alpha F}{RT}\eta\right)-\frac{C_p^s}{C_p^b}\exp\left(\frac{(1-\alpha)F}{RT}\eta\right)\right], \tag{2.35}$$

where η is the overpotential and is defined as $\eta=\phi-\phi_{eq}$. The equilibrium potential, ϕ_{eq}, can be approximated by the Nernst equation assuming Li metal as the reference, $\phi_{eq}=E^{0'}-\mu_p/F$, where $E^{0'}$ is the formal potential, which is approximated with the open circuit voltage plateau in the simulations. Assuming that the surface concentration is similar to the bulk concentration, the model can be simplified into:

$$i=i_0\left[\exp\left(-\frac{\alpha F}{RT}\eta\right)-\exp\left(\frac{(1-\alpha)F}{RT}\eta\right)\right], \tag{2.36}$$

which is the so-called Butler-Volmer equation. Dividing Eq. (2.36) by Faraday's constant, the reaction rate r_{Li} is obtained:

$$r_{Li}=\frac{i_0}{F}\left[\exp\left(-\frac{\alpha F}{RT}\eta\right)-\exp\left(\frac{(1-\alpha)F}{RT}\eta\right)\right], \tag{2.37}$$

The Butler-Volmer equation provides a good approximation for overpotential range below 100 mV. The overpotentials observed in our simulations are well within this regime. Even at the highest C-rate, the overpotential is only slightly over the 100 mV boundary, where the Butler-Volmer kinetics begin to deviate from Marcus-Hush-Chidsey kinetics, which has a broader range of accuracy than the Butler-Volmer kinetics [49, 50].

2.2 Smoothed Boundary Method

The particle-level electrochemical dynamics (PLED) equations presented above are numerically implemented using the SBM. The SBM allows us to effectively manage problems composed of multiple physics and multiple phases. In this method, a continuous domain parameter, $\psi(x)$, is used to distinguish the different domains (i.e., the electrolyte and cathode in this case). The domain boundary is defined as a region with a finite thickness, rather than a sharp boundary, thus giving rise to the name, smoothed boundary method. Figure 2.1 compares a classical sharp interface and the SBM description of a domain. Figure 2.1(a) shows the sharp boundary description of a domain. In this figure, Ω denotes the bulk of the domain, and $\partial\Omega$ denotes the interface.

In the SBM (Fig. 2.1(b)), the cathode particles are defined as the regions in which $\psi = 1$, and the electrolyte is where $\psi = 0$. The value of the domain parameter smoothly transitions from zero to one over the region near the domain boundary between the electrolyte and cathode particle, which yields a finite thickness of the interfacial region (where $0 < \psi < 1$). The conventional governing equations that describe lithium transport in the electrolyte and cathode particles as well as charge conservation in the electrolyte are reformulated into the SBM form below.

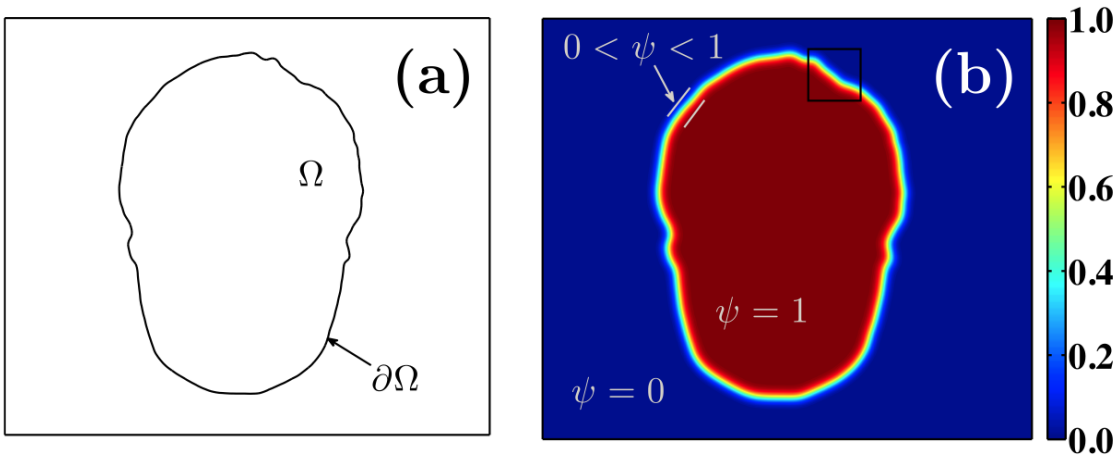

Figure 2.1: (a) Sharp interface description of a domain in which the interface has a zero thickness. (b) SBM definition of a domain in which the interface has a finite thickness. Figure obtained from Ref. [2].

2.2.1 Transport within the particles

Equation (2.5) is reformulated to its SBM form, which consists of bulk and boundary terms [2]. Here, we detail the derivation employed to generate the SBM form of the equation.

We begin by multiplying both sides of the diffusion equation, Eq. (2.5), by the domain parameter ψ,

$$\psi \frac{\partial C_p}{\partial t} = \psi \nabla \cdot (D_p \nabla C_p). \tag{2.38}$$

We then apply the product rule of differentiation to expand the RHS of the equation,

$$\psi \frac{\partial C_p}{\partial t} = \nabla \cdot (\psi D_p \nabla C_p) - \nabla \psi \cdot (D_p \nabla C_p). \tag{2.39}$$

We substitute $D_p \nabla C_p$ in the second term of the RHS of the equation with $-\mathbf{J}$ using the Fick's fist law (Eq. (2.4)),

$$\psi \frac{\partial C_p}{\partial t} = \nabla \cdot (\psi D_p \nabla C_p) + \nabla \psi \cdot \mathbf{J}. \tag{2.40}$$

A flux in the normal direction of the interface is defined as follows:

$$J_n = \vec{n} \cdot \mathbf{J}, \tag{2.41}$$

where $\vec{n}$ is the unit normal vector. The unit normal vector can be defined in terms of the domain parameter as

$$\vec{n} = \frac{\nabla\psi}{|\nabla\psi|}, \tag{2.42}$$

from which we obtain

$$\nabla\psi \cdot \mathbf{J} = |\nabla\psi| J_n. \tag{2.43}$$

Here, J_n is given by the reaction rate, r_{Li}, and thus Eq. (2.43) can be written as

$$\nabla\psi \cdot \mathbf{J} = |\nabla\psi| r_{Li}. \tag{2.44}$$

By substituting Eq. (2.44) to Eq. (2.40), the evolution equation for C_p can be expressed as follows:

$$\psi\frac{\partial C_p}{\partial t} = \nabla \cdot (\psi D_p \nabla C_p) + |\nabla\psi| r_{Li}, \tag{2.45}$$

which is rearranged into its final form,

$$\frac{\partial C_p}{\partial t} = \frac{1}{\psi}\left[\nabla \cdot (\psi D_p \nabla C_p)\right] + \frac{|\nabla\psi|}{\psi} r_{Li}. \tag{2.46}$$

Note that Eq. (2.46) reduces to the original equation, Eq. (2.5) for the bulk of the particles, where $\psi = 1$, while imposing the flux boundary condition with the reaction rate on the particle boundary. The regions where $\psi = 0$ are outside of the domain, and the solutions for these regions are nonphysical and irrelevant.

The derivation here presented can also be employed to obtain the SBM form of the Cahn-Hilliard equation (Eq. (2.3)):

$$\frac{\partial C_p}{\partial t} = \frac{1}{\psi}\nabla \cdot \left[\psi M_p \nabla\left(\mu_b - \nabla \cdot \left(\frac{\boldsymbol{\kappa}}{\rho^2}\nabla C_p\right)\right)\right] + \frac{|\nabla\psi|}{\nabla\psi} r_{Li}, \tag{2.47}$$

which is employed when phase transformation is considered.

2.2.2 Electrostatic potential in the electrolyte

The equations for charge conservation in the electrolyte (Equations (2.8a) and (2.8b)) can be combined into a single equation in the SBM formulation using a similar procedure. Equation (2.8a) is first multiplied by $(1-\psi)$, which is equal to 1 in the electrolyte phase:

$$-(1-\psi)\frac{\nabla\cdot\mathbf{i}}{z_+\upsilon_+F}=0. \tag{2.48}$$

This is expanded into

$$-\nabla\cdot\left(\frac{(1-\psi)\mathbf{i}}{z_+\upsilon_+F}\right)-\nabla\psi\frac{\mathbf{i}}{z_+\upsilon_+F}=0. \tag{2.49}$$

The second term of the left-hand side (LHS) of the equation can be re-expressed employing Eq. (2.43) as

$$-\nabla\cdot\left(\frac{(1-\psi)\mathbf{i}}{z_+\upsilon_+F}\right)-|\nabla\psi|\frac{i_n}{z_+\upsilon_+F}=0. \tag{2.50}$$

We then utilize Eq. (2.8b) and Eq. (2.41) to express the boundary condition in terms of the reaction flux,

$$-\nabla\cdot\left(\frac{(1-\psi)\mathbf{i}}{z_+\upsilon_+F}\right)-|\nabla\psi|\frac{r_{Li}}{\upsilon_+}=0. \tag{2.51}$$

Finally, we use the definition of $\mathbf{i}$ (Eq. (2.7)) and rearrange the equation to obtain the final expression,

$$\nabla\cdot[(1-\psi)\frac{F}{RT}(z_+D_+-z_-D_-)C_e\nabla\phi_e]=|\nabla\psi|\frac{r_{Li}}{\upsilon_+}+\nabla\cdot[(1-\psi)(D_--D_+)\nabla C_e]. \tag{2.52}$$

2.2.3 Transport in the electrolyte

We obtain the SBM version of the governing equations for concentration evolution of the electrolyte. Eqs. (2.18) and (2.19) are combined using the SBM domain parameter. First, the equation for transport in the electrolyte Eqs. (2.18) is multiplied by $1-\psi$, which corresponds to the bulk region of the electrolyte (i.e., $1-\psi=1$ in the

electrolyte),

$$(1-\psi)\frac{\partial C_e}{\partial t} = (1-\psi)\nabla\cdot(D_{amb}\nabla C_e) - (1-\psi)\left(\frac{\mathbf{i}\cdot\nabla t_+}{z_+\upsilon_+ F}\right). \tag{2.53}$$

Following the same steps employed to derive the equations for transport in the particles, we obtain the following form of the equation,

$$(1-\psi)\frac{\partial C_e}{\partial t} = \nabla\cdot\left[(1-\psi)D_{amb}\nabla C_e\right] - (1-\psi)\left(\frac{\mathbf{i}\cdot\nabla t_+}{z_+\upsilon_+ F}\right) - |\nabla\psi| J_n. \tag{2.54}$$

Combining Eq. (2.19) and (2.41), we obtain $J_n = (1-t_+)r_{Li}$. By substituting this to Eq. (2.54), we arrive at the final form of the equation,

$$\frac{\partial C_e}{\partial t} = \frac{1}{1-\psi}\left[\nabla\cdot\left((1-\psi)D_{amb}\nabla C_e\right)\right] - \left(\frac{\mathbf{i}\cdot\nabla t_+}{z_+\upsilon_+ F}\right) - (1-t_+)\frac{|\nabla\psi|}{1-\psi} r_{Li}. \tag{2.55}$$

Note that Eq. (2.55) reduces to the original equation, Eq. (2.18), in the electrolyte. At the particle-electrolyte interface, where $|\nabla\psi| \neq 0$, the reaction rate sets the flux boundary condition.

2.3 Numerical Methods

We now discuss the numerical methods employed to solve the governing equations. The simulation domain is discretized on a three-dimensional (3D) Cartesian grid with uniform spacing. Here, the subscripts i, j and k indicate a grid point along in the x-, y- and z-directions, respectively, and the superscript n indicates the time step.

2.3.1 Discretization

We first describe the spatial discretization. We here employ a second-order central finite difference scheme, approximation that allows us to solve the governing equations in a computationally efficient manner. As an example, we here show the discretization of the term $\nabla\cdot(D\psi\nabla C)$, which appears in Eq. (2.46) (for brevity we here drop the suscripts p).

We first expand the term $D\psi\nabla C$. The term has components in the three cartesian directions,

$$D\psi\nabla C = \left(D\psi\frac{\partial C}{\partial x}\right)\hat{\mathbf{x}} + \left(D\psi\frac{\partial C}{\partial y}\right)\hat{\mathbf{y}} + \left(D\psi\frac{\partial C}{\partial z}\right)\hat{\mathbf{z}}, \tag{2.56}$$

where $\hat{\mathbf{x}}$, $\hat{\mathbf{y}}$, and $\hat{\mathbf{z}}$ are the unit vectors in x-, y- and z-direction, respectively. In a 3D domain, the divergence of a gradient, $\nabla \cdot (\psi\nabla C)$, results in the scalar

$$\nabla \cdot (D\psi\nabla C) = \frac{\partial}{\partial x}\left(D\psi\frac{\partial C}{\partial x}\right) + \frac{\partial}{\partial y}\left(D\psi\frac{\partial C}{\partial y}\right) + \frac{\partial}{\partial z}\left(D\psi\frac{\partial C}{\partial z}\right). \tag{2.57}$$

As the first step, we discretize the terms within the parentheses. These partial derivatives can be defined at a location halfway between grid points. Using a Taylor expansion, $(D\psi\frac{\partial C}{\partial x})$ are discretized at the midpoint $i+1/2$ and $i-1/2$ into

$$\left(D\psi\frac{\partial C}{\partial x}\right)_{i+1/2,j,k} = \frac{(D_{i+1,j,k}+D_{i,j,k})}{2}\frac{(\psi_{i+1,j,k}+\psi_{i,j,k})}{2}\frac{(C_{i+1,j,k}-C_{i,j,k})}{h}, \tag{2.58a}$$

$$\left(D\psi\frac{\partial C}{\partial x}\right)_{i-1/2,j,k} = \frac{(D_{i,j,k}+D_{i-1,j,k})}{2}\frac{(\psi_{i,j,k}+\psi_{i-1,j,k})}{2}\frac{(C_{i,j,k}-C_{i-1,j,k})}{h}, \tag{2.58b}$$

respectively, where h is the uniform grid spacing ($\Delta x = \Delta y = \Delta z = h$). Similar to Eqs. (2.58a) and (2.58b) , $(D\psi\frac{\partial C}{\partial y})$ is discretized in the y-direction at midpoints $j+1/2$ and $j-1/2$, and $(D\psi\frac{\partial C}{\partial z})$ is discretized in the z-direction at midpoints $k+1/2$ and $k-1/2$.

The partial derivatives outside the parentheses in Eq. (2.57) are discretized in a similar manner in terms of the partial derivatives inside the parentheses,

$$\begin{aligned}\nabla \cdot \left(D\psi\nabla C\right)_{i,j,k} = &\frac{\left(D\psi\frac{\partial C}{\partial x}\right)_{i+1/2,j,k} - \left(D\psi\frac{\partial C}{\partial x}\right)_{i-1/2,j,k}}{h} + \\ &\frac{\left(D\psi\frac{\partial C}{\partial y}\right)_{i,j+1/2,k} - \left(D\psi\frac{\partial C}{\partial y}\right)_{i,j-1/2,k}}{h} + \\ &\frac{\left(D\psi\frac{\partial C}{\partial z}\right)_{i,j,k+1/2} - \left(D\psi\frac{\partial C}{\partial z}\right)_{i,j,k-1/2}}{h}.\end{aligned} \tag{2.59}$$

Substituting the discretizations shown in Eqs. (2.58a) and (2.58b) and those corre-

sponding to other directions into Eq. (2.59), we obtain

$$\begin{aligned}\nabla \cdot \Big(D\psi \nabla C \Big)_{i,j,k} = \frac{1}{4h^2} \Big[& (D_{i+1,j,k} + D_{i,j,k})(\psi_{i+1,j,k} + \psi_{i,j,k})(C_{i+1,j,k} - C_{i,j,k}) - \\ & (D_{i,j,k} + D_{i-1,j,k})(\psi_{i,j,k} + \psi_{i-1,j,k})(C_{i,j,k} - C_{i-1,j,k}) + \\ & (D_{i,j+1,k} + D_{i,j,k})(\psi_{i,j+1,k} + \psi_{i,j,k})(C_{i,j+1,k} - C_{i,j,k}) - \\ & (D_{i,j,k} + D_{i,j-1,k})(\psi_{i,j,k} + \psi_{i,j-1,k})(C_{i,j,k} - C_{i,j-1,k}) + \\ & (D_{i,j,k+1} + D_{i,j,k})(\psi_{i,j,k+1} + \psi_{i,j,k})(C_{i,j,k+1} - C_{i,j,k}) - \\ & (D_{i,j,k} + D_{i,j,k-1})(\psi_{i,j,k} + \psi_{i,j,k-1})(C_{i,j,k} - C_{i,j,k-1}) \Big],\end{aligned} \tag{2.60}$$

which is the spatial discretization we employ.

We now describe the temporal discretization. We utilize a forward difference approach to describe the partial derivative with respect to time:

$$\frac{\partial C^n}{\partial t} = \frac{C^{n+1} - C^n}{\Delta t}, \tag{2.61}$$

where Δt is the time step. To describe the terms that are not derived with respect to time, we use two different temporal discretization methods. For the concentration evolution of the particles, the RHS of Eq. (2.46) or (2.47) is evaluated at time n, which yields an explicit time stepping. For the concentration evolution of the electrolyte, the RHS of Eq. (2.55) is evaluated at time $n + 1$, which leads to an implicit time stepping. For the electrostatic potential of the electrolyte, which does not have a partial derivative with respect to time, the variables are assumed at time $n + 1$. Below, we describe how each of the discretized equations are solved.

2.3.2 Direct solver for the concentration evolution in the particles

We employ a first-order forward Euler time-stepping scheme to determine the particle concentration. Here, we present the discretization of the SBM form of Fick's diffusion

(Eq. (2.46)). Note that here we refer drop the subindices p for simplicity. Using Eqs. (2.60) and (2.61), we discretize Eq. (2.46) into the following:

$$\begin{aligned}
&\frac{C^{n+1}_{i,j,k} - C^{n}_{i,j,k}}{\Delta t} = \\
&\frac{1}{4h^2\psi}\Big[(D_{i+1,j,k} + D_{i,j,k})(\psi_{i+1,j,k} + \psi_{i,j,k})(C^{n}_{i+1,j,k} - C^{n}_{i,j,k}) - \\
&\quad (D_{i,j,k} + D_{i-1,j,k})(\psi_{i,j,k} + \psi_{i-1,j,k})(C^{n}_{i,j,k} - C^{n}_{i-1,j,k}) + \\
&\quad (D_{i,j+1,k} + D_{i,j,k})(\psi_{i,j+1,k} + \psi_{i,j,k})(C^{n}_{i,j+1,k} - C^{n}_{i,j,k}) - \\
&\quad (D_{i,j,k} + D_{i,j-1,k})(\psi_{i,j,k} + \psi_{i,j-1,k})(C^{n}_{i,j,k} - C^{n}_{i,j-1,k}) + \\
&\quad (D_{i,j,k+1} + D_{i,j,k})(\psi_{i,j,k+1} + \psi_{i,j,k})(C^{n}_{i,j,k+1} - C^{n}_{i,j,k}) - \\
&\quad (D_{i,j,k} + D_{i,j,k-1})(\psi_{i,j,k} + \psi_{i,j,k-1})(C^{n}_{i,j,k} - C^{n}_{i,j,k-1})\Big] \\
&\qquad + \frac{|\nabla\psi_{i,j,k}|}{\psi_{i,j,k}} r^{n}_{Li,i,j,k},
\end{aligned} \tag{2.62a}$$

where the central discretization of $|\nabla\psi_{i,j,k}|$ is

$$|\nabla\psi_{i,j,k}| = \sqrt{\left(\frac{\psi_{i+1,j,k} - \psi_{i-1,j,k}}{2h}\right)^2 + \left(\frac{\psi_{i,j+1,k} - \psi_{i,j-1,k}}{2h}\right)^2 + \left(\frac{\psi_{i,j,k+1} - \psi_{i,j,k-1}}{2h}\right)^2}. \tag{2.62b}$$

Equation (2.62a) has only one unknown at each grid point, $C^{n+1}_{i,j,k}$, and can therefore be solved directly.

2.3.3 Alternating-direction-line-relaxation (ADLR) solver for the concentration evolution in the electrolyte

We now describe the method employed to solve the governing equation for the Li transport in the electrolyte. The method is also used in determining the electrostatic potential from Eq. (2.55).

Here, Eq. (2.55) is rewritten for the case of constant diffusivity,

$$\frac{\partial C}{\partial t} = \frac{D_{amb}}{\psi}\left[\nabla\cdot\left(\psi\nabla C\right)\right] - (1 - t_+)\frac{|\nabla\psi|}{\psi} r_{Li}. \tag{2.63}$$

For simplicity, we employ the simplified notation $C = C_e$ and $\hat{\psi} = 1 - \psi$. Equation

(2.63) is discretized in a similar manner as Eq. (2.62a); the difference is that the terms on the RHS of the equation are evaluated at timestep $n+1$, except for the reaction rate, which is evaluated at time step n:

$$\begin{aligned}
&\frac{C^{n+1}_{i,j,k} - C^{n}_{i,j,k}}{\Delta t} = \\
&\frac{D_{amb}}{2h^2\hat{\psi}_{i,j,k}}\Big[(\hat{\psi}_{i+1,j,k}+\hat{\psi}_{i,j,k})(C^{n+1}_{i+1,j,k}-C^{n+1}_{i,j,k}) - (\hat{\psi}_{i,j,k}+\hat{\psi}_{i-1,j,k})(C^{n+1}_{i,j,k}-C^{n+1}_{i-1,j,k}) + \\
&\quad (\hat{\psi}_{i,j+1,k}+\hat{\psi}_{i,j,k})(C^{n+1}_{i,j+1,k}-C^{n+1}_{i,j,k}) - (\hat{\psi}_{i,j,k}+\hat{\psi}_{i,j-1,k})(C^{n+1}_{i,j,k}-C^{n+1}_{i,j-1,k}) + \\
&\quad (\hat{\psi}_{i,j,k+1}+\hat{\psi}_{i,j,k})(C^{n+1}_{i,j,k+1}-C^{n+1}_{i,j,k}) - (\hat{\psi}_{i,j,k}+\hat{\psi}_{i,j,k-1})(C^{n+1}_{i,j,k}-C^{n+1}_{i,j,k-1})\Big] \\
&\quad -(1-t_+)\frac{|\nabla\hat{\psi}_{i,j,k}|}{\hat{\psi}_{i,j,k}} r^{n}_{Li,i,j,k}.
\end{aligned} \tag{2.64}$$

Equation (2.64) can be rearranged as follows:

$$\begin{aligned}
&\hat{\psi}(C^{n+1}_{i,j,k} - C^{n}_{i,j,k}) = \\
&D^*\Big[(\hat{\psi}_{i+1,j,k}+\hat{\psi}_{i,j,k})(C^{n+1}_{i+1,j,k}-C^{n+1}_{i,j,k}) - (\hat{\psi}_{i,j,k}+\hat{\psi}_{i-1,j,k})(C^{n+1}_{i,j,k}-C^{n+1}_{i-1,j,k}) + \\
&\quad (\hat{\psi}_{i,j+1,k}+\hat{\psi}_{i,j,k})(C^{n+1}_{i,j+1,k}-C^{n+1}_{i,j,k}) - (\hat{\psi}_{i,j,k}+\hat{\psi}_{i,j-1,k})(C^{n+1}_{i,j,k}-C^{n+1}_{i,j-1,k}) + \\
&\quad (\hat{\psi}_{i,j,k+1}+\hat{\psi}_{i,j,k})(C^{n+1}_{i,j,k+1}-C^{n+1}_{i,j,k}) - (\hat{\psi}_{i,j,k}+\hat{\psi}_{i,j,k-1})(C^{n+1}_{i,j,k}-C^{n+1}_{i,j,k-1})\Big] \\
&\quad -\Delta t(1-t_+)|\nabla\hat{\psi}_{i,j,k}| r^{n}_{Li,i,j,k},
\end{aligned} \tag{2.65}$$

where $D^* = D_{amb}\Delta t/(2h^2)$.

Equation (2.65) can be written as a matrix equation of the form $A\mathbf{x} = \mathbf{b}$, where A is a square matrix, $\mathbf{x}$ is a vector containing the values of C^{n+1} at the different grid points, and $\mathbf{b}$ is a vector. To solve for this matrix equation, calculating the inverse of the matrix A is required, however inverting a matrix is computationally expensive. It is convenient to modify the matrix to express it as a tridiagonal matrix because finding the inverse of a such a matrix is computationally less expensive. Therefore, we use an alternating-direction-line-relaxation (ADLR) solver [51, 52, 2] to solve Eq. (2.65). In

ADLR, the different unknowns in a Cartesian direction are solved iteratively, allowing the matrix to become tridiagonal. To illustrate this procedure here, we present the process for solving the equation in the x-direction. We thus first consider $C^{n+1}_{i-1,j,k}$, $C^{n+1}_{i,j,k}$ and $C^{n+1}_{i+1,j,k}$ as the unknowns, while $C^{n+1}_{i,j-1,k}$, $C^{n+1}_{i,j+1,k}$, $C^{n+1}_{i,j,k-1}$ and $C^{n+1}_{i,j,k+1}$ are held constant. Taking the unknowns to the LHS and the knowns to the RHS,

$$\begin{aligned}-D^*(\hat{\psi}_{i,j,k}+\hat{\psi}_{i-1,j,k})C^{n+1}_{i-1,j,k}+(\hat{\psi}_{i,j,k}+\hat{\psi}^*_{i,j,k}D^*)C^{n+1}_{i,j,k}-D^*(\hat{\psi}_{i+1,j,k}+\hat{\psi}_{i,j,k})C^{n+1}_{i+1,j,k}=\\ D^*\Big[(\hat{\psi}_{i,j+1,k}+\hat{\psi})(C^{n+1}_{i,j+1,k})+(\hat{\psi}_{i,j,k}+\hat{\psi}_{i,j-1,k})(C^{n+1}_{i,j-1,k})+\\ (\hat{\psi}_{i,j,k+1}+\hat{\psi}_{i,j,k})(C^{n+1}_{i,j,k+1})+(\hat{\psi}_{i,j,k}+\hat{\psi}_{i,j,k-1})(C^{n+1}_{i,j,k-1})\Big]\\ +\hat{\psi}_{i,j,k}C_{i,j,k}-\Delta t(1-t_+)|\nabla\hat{\psi}_{i,j,k}|r_{Li,i,j,k},\end{aligned} \tag{2.66}$$

where

$$\begin{aligned}\hat{\psi}^*_{i,j,k}=(\hat{\psi}_{i+1,j,k}+\hat{\psi}_{i,j,k})+(\hat{\psi}_{i,j,k}+\hat{\psi}_{i-1,j,k})+\\ (\hat{\psi}_{i,j+1,k}+\hat{\psi}_{i,j,k})+(\hat{\psi}_{i,j,k}+\hat{\psi}_{i,j-1,k})+(\hat{\psi}_{i,j,k+1}+\hat{\psi}_{i,j,k})+(\hat{\psi}_{i,j,k}+\hat{\psi}_{i,j,k-1}).\end{aligned} \tag{2.67}$$

For a domain of size x in the x-direction, Eq. (2.66) can be rewritten as a tridiagonal matrix,

$$\begin{bmatrix} b_1 & c_1 & & & & & \\ a_2 & b_2 & c_2 & & & & \\ & a_3 & b_3 & c_3 & & & \\ & & \ddots & \ddots & \ddots & & \\ & & & a_{x-2} & b_{x-2} & c_{x-2} & \\ & & & & a_{x-1} & b_{x-1} & c_{x-1} \\ & & & & & a_x & b_x \end{bmatrix} \begin{bmatrix} C_{1,j,k} \\ C_{2,j,k} \\ C_{3,j,k} \\ \vdots \\ C_{x-2,j,k} \\ C_{x-1,j,k} \\ C_{x,j,k} \end{bmatrix} = \begin{bmatrix} d_1-a_0 \\ d_2 \\ d_3 \\ \vdots \\ d_{x-2} \\ d_{x-1} \\ d_x-c_x \end{bmatrix}, \tag{2.68}$$

where

$$a_i=-D^*(\hat{\psi}_{i,j,k}+\hat{\psi}_{i-1,j,k}), \tag{2.69a}$$

$$b_i = (\hat{\psi}_{i,j,k} + \hat{\psi}^*_{i,j,k} D^*), \tag{2.69b}$$

$$c_i = -D^*(\hat{\psi}_{i+1,j,k} + \hat{\psi}_{i,j,k}), \tag{2.69c}$$

$$\begin{aligned} d_i = D^* \Big[& (\hat{\psi}_{i,j+1,k} + \hat{\psi}_{i,j,k})(C^{n+1}_{i,j+1,k}) + (\hat{\psi}_{i,j,k} + \hat{\psi}_{i,j-1,k})(C^{n+1}_{i,j-1,k}) + \\ & (\hat{\psi}_{i,j,k+1} + \hat{\psi}_{i,j,k})(C^{n+1}_{i,j,k+1}) + (\hat{\psi}_{i,j,k} + \hat{\psi}_{i,j,k-1})(C^{n+1}_{i,j,k-1}) \Big] \\ & + \hat{\psi}_{i,j,k} C^n_{i,j,k} - \Delta t(1 - t_+) |\nabla \hat{\psi}_{i,j,k}| r_{Li,i,j,k}. \end{aligned} \tag{2.69d}$$

We directly solve for this matrix using a tridiagonal matrix solver. In the first iteration, the values of C in the RHS are approximated with their values from time n, and in the subsequent iterations with their values from the previous iteration. A similar matrix is then constructed to solve the equation in the y-direction using the results from the solution for Eq. (2.68) for the x-direction as the input. Here, the terms involving $C^{n+1}_{i,j-1,k}$, $C^{n+1}_{i,j,k}$, and $C^{n+1}_{i,j+1,k}$ in Eq. (2.66) are placed on the LHS, and the remaining terms are placed on the RHS. This equation is also expressed as a matrix equation with a tridiagonal matrix and is solved directly using the tridiagonal matrix solver. Finally, we solve for the equation for the z-direction using the solution from the y-direction as input. In this case, the terms $C^{n+1}_{i,j,k-1}$, $C^{n+1}_{i,j,k}$, and $C^{n+1}_{i,j,k+1}$ in Eq. (2.66) are placed on the LHS, and the remaining terms on the RHS. This equation is solved in a similar manner. This process is repeated until a convergence criterion is met. The name "alternating direction line relaxation" stems from the fact that the direction along which the variables are updated alternates.

CHAPTER III

THE EXCHANGE CURRENT DENSITY AND POSITION DEPENDENCE OF PARTICLE INTERACTIONS

3.1 Introduction

In this chapter, we investigate the dynamics of interparticle phase separation (i.e., mosaic instability) during lithiation and delithiation (discharge and charge) in phase separating electrodes consisting of nanoparticles. We constrain ourselves to the case where all the particles are of the same size, allowing us to focus on the dependence of the interactions on the exchange current density and on the position of the particles within the electrode. We model the nanoparticles as a Li solid solution based on the theory mentioned in Chapter II. This chapter presents an in-depth study of (1) the initiation of the interparticle phase separation, (2) the asymmetric lithiation/delithiation caused by an activity-dependent exchange current density, and (3) the two distinct processes that occur during the interparticle phase separation.

To elucidate the interactions between particles, we first analyze a cell containing two nanoparticles (Sec. 3.4.1). The simulations are then extended to a larger domain containing 26 nanoparticles in a unit cell that is periodic in the direction normal to the cell current (Sec. 3.4.2-3.4.3). The interaction dynamics under varying applied currents is investigated. Furthermore, the effect of the exchange current density is studied by taking the exchange current density to be independent of the activity of the nanoparticles (Sec. 3.4.2) and by using a cathode-activity-dependent exchange current

density (Sec. 3.4.3). Analyses are performed to determine what critical concentration difference is required to trigger the interparticle phase separation, what controls the size of the group of particles that undergo phase transformation simultaneously, and how two mechanisms (Li redistribution and constant (de)lithiation) compete during the interparticle phase separation (Sec. 3.5). Finally, we compare our simulations with those of a macro-homogeneous model based on the porous electrode theory as a verification of our results (Sec. 3.6). While we show that our model reproduces the results of a porous-electrode model for the simple setup studied here, it is a powerful framework with the capability to predict the detailed dynamics in three-dimensional complex electrodes and provides further insights into the complex dynamics that result from the coupling of electrochemistry, thermodynamics, and transport kinetics.

3.2 Model

The model employed in this chapter was almost entirely presented in Chapter II. However, certain definitions, such as the free energy function and exchange current density, were not defined because different functions are utilized throughout the thesis. In this chapter, we assume that the particles remain monophasic; therefore, we use the smoothed boundary method (SBM) form of Fick's diffusion (Eq. (2.46)) to solve for the concentration evolution in the particles. The electrostatic potential and concentration of the electrolyte are solved using Eqs. (2.52) and (2.55), respectively.

In this chapter, we use the regular solution model, which includes both entropic and enthalpic effects, to define the chemical potential of the particles. In the regular solution model, the free energy of Li in the particles, f, takes the form of

$$f = RT\Big[X_p \ln(X_p) + (1 - X_p)\ln(1 - X_p) + \Omega X_p(1 - X_p)\Big], \tag{3.1}$$

where X_p is the site fraction of Li in Li_xFePO_4, R is the gas constant, T is the absolute temperature, and Ω is the interaction parameter. The bulk chemical potential, μ_b,

which is the partial derivative of the free energy with respect to site fraction (Eq. (1.1)) takes the form of:

$$\mu_b = \mu_p = RT\left[\ln\left(\frac{X_p}{1-X_p}\right) + \Omega(1-2X_p)\right]. \tag{3.2}$$

Here μ_b is equal to μ_p since the particles are assumed monophasic. When Ω has a value greater than two, the free energy becomes a double-well function and the chemical potential becomes non-monotonic. This represents a state where phase separation is thermodynamically favored.

The electrochemical reaction rate, r_{Li}, was solved using the Butler-Volmer equation, Eq. (2.37). In this chapter, the exchange current density is a function of the activities of Li in the electrolyte and particles, which yields a nonlinear dependence of the exchange current density on the Li concentration. The use of an activity-dependent exchange current density is referred to as the "modified Butler Volmer" equation [53, 20], which differs from the standard Butler-Volmer equation, which is linearly dependent on the concentration. In a dilute electrolyte, the activity can be approximated by the normalized concentration, $a_e = C_e/C_e^0$, where C_e is the electrolyte concentration and C_e^0 is the concentration at which i_0 was measured. In the particles, the activity is defined by the Arrhenius equation of the chemical potential as $a_p = \exp(\mu_p/RT)$. Thus, the exchange current density is given by

$$i_0 = \frac{F(k_c^0 a_e)^{1-\alpha}(k_a^0 a_p)^{\alpha}}{\gamma_{TS}} = i_0'\sqrt{a_e X_p(1-X_p)\exp[\Omega(1-2X_p)]}. \tag{3.3}$$

Here, it has been assumed that $\alpha = 0.5$ and $i_0' = F(k_c^0)^{1-\alpha}(k_a^0)^{\alpha}$, where i_0' is the exchange current coefficient, k_c^0 and k_a^0 are the standard rate constants of cathodic and anodic reactions, respectively, and γ_{TS} is the chemical activity coefficient of the transition state, approximated as $(1-X_p)^{-1}$ to account for the site availability [20]. (The approach of combining the two rate constants into one parameter (i_0') is similar to those presented in Refs. [20, 54, 55].)

3.3 Simulation Configuration

We consider a cell that contains a cathode consisting of equal-sized nanoparticles immersed in a $LiPF_6$ electrolyte, a separator represented by empty space filled with electrolyte, and lithium metal foil as the anode, for which the Li concentration and chemical potential are constant. A square-prismatic computational box is used in the simulations, which spans 1152 nm in the direction from the anode to the cathode current collector (z-axis) and 64 nm in other directions (x- and y-axes). The anode-electrolyte interface is located at the boundary at $z = 0$. Furthermore, $r_{Li,j}$ and S_j are the reaction rate and surface of particle j, respectively, N_{tot} is the total number of particles, and A_a is the total area of the anode-electrolyte boundary. The cathode current collector is located at $z = 1152$ nm, where we apply a no-flux boundary condition for C_e and ϕ_e, and the value of ϕ_p is adjusted to obtain the current set by the constant current condition. Periodic boundary conditions are imposed on the x-z and y-z planes of the computational box. Thus, this configuration represents a planar cell, of which in-plane dimensions (in x-y plane) are much larger than the depth (in z-direction) of the cell. Such an arrangement is convenient for investigating the effect of particle locations on the interparticle phase separation in the depth direction.

Simulations with two different configurations were conducted: one with two particles and the other with 26 particles in the cell. In the first set, two particles 40 nm in diameter were located 728 nm apart (measured between the closest surfaces), one particle was 332 nm from the anode and the other was 12 nm from the cathode current collector with respect to the nearest surfaces; see Fig. 3.1(a). This two-particle simulation is designed to illustrate the cell voltage response during the interaction between particles. In the second simulation configuration, the cathode contains 26 particles in a body-centered-cubic arrangement, where the shortest distance between particle surfaces is 15 nm; see Fig. 3.3(a). The cathode spans 852 nm in the z-direction, while the separator (region of electrolyte without particles) has a length of 300 nm.

The cathode region of this cell has a volume fraction of approximately 25.3% for the active particles. While this particle volume fraction is smaller than an actual battery cathode, it allows us to elucidate the behavior of interacting particles, and we expect the qualitative findings to remain valid for the range of current we examine in this work. This set of simulations with this given arrangement provides information for the many-particle dynamics.

A constant applied current was maintained during the simulations by adjusting the value of the electrostatic potential of the particles. Note, however, that the imposed value of the applied current (calculated using Eq. (2.7) at the anode-electrolyte interface) was allowed to fluctuate ±1.5% to facilitate the faster convergence of the alternating-direction-line-relaxation (ADLR) scheme (described in Chapter II) and improving the numerical efficiency.

We choose the average applied current density (normalized to the total particle surface), $\bar{i}$, to be one of the controlling parameters,

$$\bar{i} = \frac{\sum_{j=1}^{N_{tot}} \int_{S_j} r_{Li,j} F dS_j}{\sum_{j=1}^{N_{tot}} \int_{S_j} dS_j}. \tag{3.4}$$

In the SBM formulation, the interface has a finite thickness and thus a finite volume. Therefore, Eq. (3.4) can also be expressed as

$$\bar{i} = \frac{\sum_{j=1}^{N_{tot}} \int_{V_j} r_{Li,j} F |\nabla\psi| dV_j}{\sum_{j=1}^{N_{tot}} \int_{V_j} |\nabla\psi| dV_j}, \tag{3.5}$$

where ψ is the domain parameter.

Throughout the chapter, $\bar{i}$ is specified as a fraction of the exchange current coefficient, i_0'. We do so to emphasize that the observed dynamics at a given rate depends on the ratio $\bar{i}/i_0'$ and that there is a certain degree of uncertainty in the literature

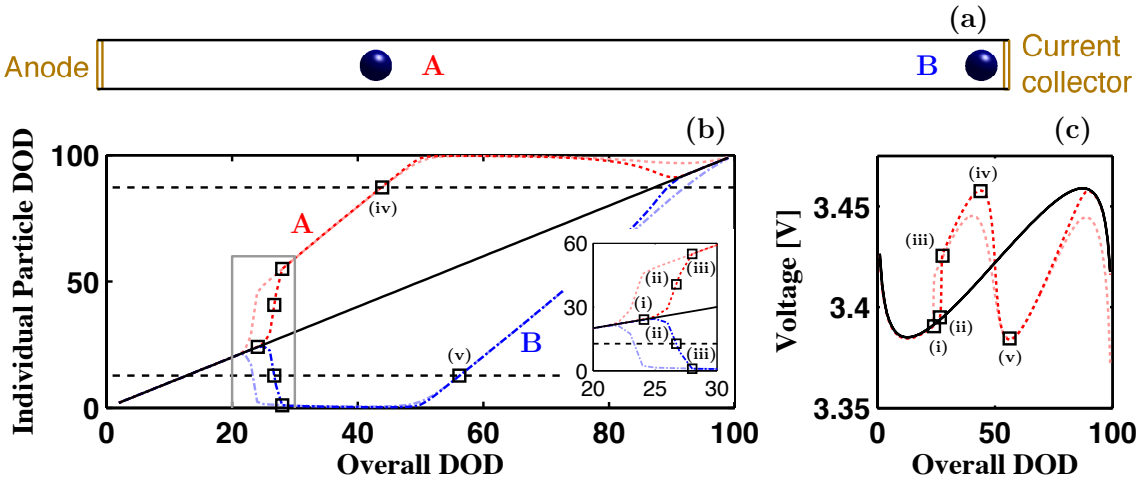

Figure 3.1: (a) Two-particle configuration used in these simulations. (b) Depth of discharge (DOD) of the individual particles with respect to the overall DOD; the range at which the interparticle phase separation begins is magnified in the inset. The dashed red curves correspond to the DOD of the particle closer to the separator (particle A), the dash-dotted blue curves to the DOD of the particle closer to the cathode current collector (particle B) and the black line to the overall DOD. (c) Simulated voltage during the lithiation process with respect to the overall DOD. The red curves represent the obtained voltage from the simulations and the black curve corresponds to the single-particle equilibrium potential. In (b) and (c), the darker curves represent the case when i_0 is assumed to be activity independent and the lighter curves represent when this dependence is included. Labels (i)-(v) highlight the key points of the lithiation process.

values of i_0'. For example, in the work of Dargaville and Farrell [54], a sensitivity analysis on i_0' is performed to address this uncertainty. Note that a constant current density with respect to the particle surface is equivalent to a constant C-rate since the particle size remains unchanged. However, the current density scales with the particle surface while the C-rate, scales with the particle volume (or mass). Consequently, for a system with a given mass under the same C-rate but with larger particles, a larger current density at the surface of the particles will be observed.

The physical parameters used in the simulations are given as follows. For the cathode, the diffusion coefficient of Li in the particles is 1×10^{-12} cm^2/s [56], assumed isotropic for simplicity, and the interstitial site density is 0.0228 mol/cm^3. In the electrolyte, the diffusion coefficients for the cation (Li^+) and anion (PF_6^-) are 1.25×10^{-6} cm^2/s and 4.0×10^{-6} cm^2/s, respectively, to match the work of Ferguson and Bazant [45], which were based on experimental results [57, 58]. The electrolyte has an average concentration of 1 M (consistent with the molarity at which the ionic diffusivities and the exchange current density were measured). The dissociation number of the cation is equal to one. For the modified Butler-Volmer equation, we take $i_0' = 1.75 \times 10^{-6}$ A/cm^2. Here, we have scaled an experimental value of i_0' similar to the one from Refs. [59, 60] by 1/100, as was done in Ref. [20], since the experimental value was measured per the macroscopic cross-sectional area of the cathode, not the actual particle surface area, which is needed for our simulation. The open circuit voltage plateau of $LiFePO_4$ is taken to be 3.422 V [5] and the interaction parameter, Ω, is set to 4.5 [43] for evaluating the chemical potential. This interaction parameter gives a non-monotonic voltage profile with a difference between the local minimum and local maximum of approximately 74 mV; see the single-particle equilibrium potential profile in Fig. 3.1(c).

The cathode structure was defined using the SBM domain parameter. To obtain a unique domain parameter that defines all particles, we first defined each domain

parameter independently using a piecewise sine function:

$$\tilde{\psi}_j = \begin{cases} 1 & \text{if} \quad \left(\frac{|\vec{x}-\vec{x}_{j0}|-r}{\xi}\right) < -\frac{\pi}{2} \\ 0 & \text{if} \quad \left(\frac{|\vec{x}-\vec{x}_{j0}|-r}{\xi}\right) > \frac{\pi}{2} \\ 1-\frac{1}{2}\left[\sin\left(\frac{|\vec{x}-\vec{x}_{j0}|-r}{\xi}\right)+1\right] & \text{otherwise,} \end{cases} \tag{3.6}$$

where $\tilde{\psi}_j$ is the domain parameter of the particle, ξ is a parameter used control the interface thickness, $\vec{x}$ denotes position, and $\vec{x}_{j_0}$ and r_j are the center position and the radius of particle j, respectively. These sets of domain parameters were then added to obtain the domain parameters used in the simulations:

$$\psi = \sum_{j=1}^{N_{tot}} \tilde{\psi}_j. \tag{3.7}$$

The parameter ξ and the grid spacing are set to 2 nm.

3.4 Results

3.4.1 Lithiation in a two-particle cell

We first conducted the simulation of a two-particle cell to illustrate the interparticle interactions and the corresponding voltage response, in a similar way as in Ref. [61]. The cell was lithiated at an applied current density, $\bar{i}$, which is chosen to be 2% of i_0' to examine the low current regime. This loading condition is approximately a C/12 rate. In the first case, we focus exclusively on the interparticle interactions. We first ignore the dependence of the exchange current density on the activity of the cathode particles, and i_0 is assumed to only depend on the electrolyte activity, $i_0 = i_0'\sqrt{a_e}$. Hereafter in this chapter, we refer to the cathode-activity simply as "activity" for convenience.

The depth of discharge (DOD) for the two individual particles and the voltage profile during the lithiation process are shown in Figs. 3.1(b) and (c), respectively.

Here, we refer to the particle close to the separator as particle A and the one close to the cathode current collector as particle B. Since the cell is lithiated under a constant current, the average DOD increases linearly. However the DOD of the individual particles exhibits different behavior. Five points, (i) through (v), on the curves are noted to illustrate the unique dynamics of the interparticle interactions. In the early stage of discharge (prior to point (i)), both of the particles lithiate at a similar rate. However, particle A lithiates slightly faster because both the ion concentration and electrostatic potential in the surrounding electrolyte are higher than that of particle B. Thus, particle A reaches the concentration level of the lower spinodal point first and undergoes rapid lithiation (see point (i)), during which lithium is extracted from particle B (between point (i) and (ii)). Once the concentration level of particle B drops below that of the lower spinodal point, a sudden rise in the voltage curve is observed; see point (ii) in Figs. 3.1(b) and (c). After particle B fully delithiates, the slope of the voltage curve decreases due to the slow lithiation of particle A because it can no longer extract lithium from particle B; see point (iii). When particle A reaches the higher spinodal point, the voltage decreases; see point (iv). In the meantime, the concentration level of particle B slowly increases. After particle B reaches the lower spinodal point, the voltage rises again; see point (v). During the lithiation of particle B, lithium is extracted from particle A to a lesser degree; see the DOD of particle A between point (v) and the end of the evolution.

The dynamics observed above can be understood as follows. To maintain a constant current, the applied voltage is adjusted to a specific value. When such voltage resides in the gap between the local minimum and local maximum of the single-particle equilibrium potential curve (the inverted potential range, shown in Fig. 1.8) and falls in-between the equilibrium potentials of the two particles, one particle is driven to lithiate and the other to delithiate, producing the interparticle phase separation.

Next, we conduct the simulation where the exchange current density is a function

of the activity of the particles, as given in Eq. (3.3); see Fig. 3.2. The form of the exchange current density results from the regular solution model, as explained in Sec. 2.1.4. It has the maximum value when the Li concentration is close to the lower spinodal point, as this is where both the chemical potential and the site availability are large. The difference is substantial – the exchange current density is 28.6 times larger at the lower spinodal point than at the higher spinodal point. Therefore, the magnitude of the required overpotential to maintain a constant current density is smaller at low concentrations and is larger at high concentrations. It is important to note that this exchange current density is based on the regular solution model. For higher accuracy, a more realistic exchange current density is required.

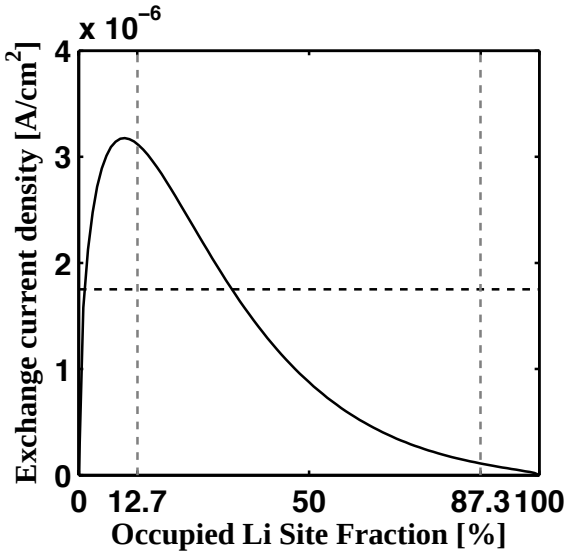

Figure 3.2: Exchange current density. Solid curve: i_0 as a function of the occupied Li site fraction as expressed in Eq. (3.3). Dashed horizontal line: value of i_0 independent of the Li site fraction. The maximum value of the function is located near the lower spinodal point. The value of the exchange current density at the lower spinodal point is 28.6 times higher than that at the larger spinodal point. The vertical dashed lines represent the spinodal points.

The simulation results are given in the lighter curves in Figs. 3.1(b) and (c), and show three features that differ from the case with exchange current density independent of the activity. First, the interparticle phase separation occurs at a lower con-

centration, since the magnitude of the overpotential at low concentrations is smaller (this will be further explained in Sec. 3.5.1). Second, the peak of the voltage rise is smaller (Fig. 3.1(c)), since the overpotential at higher concentrations is larger. Last, at the very end of the process, the redistribution of Li between particle A and particle B is almost completely suppressed (Fig. 3.1(b)). This is caused by the much smaller exchange current density of the particles at that concentration.

3.4.2 Lithiation and delithiation with exchange current density independent of the cathode activity

Having developed an understanding of how two particles can interact, we now examine the dynamics with a larger number of particles via a simulation of the 26-particle configuration mentioned earlier. As in the two-particle configuration, the simulation was also performed at $\bar{i} = 2\%\ i_0'$ (C/12 rate) and the dependence of the exchange current density on the activity of the particles was ignored by assuming $i_0 = i_0'\sqrt{a_e}$ in this section. Figure 3.3 shows Li concentration in the particles at four different times during lithiation. First, all the particles lithiate in a fairly even manner up to the cell DOD of 22%; see Fig. 3.3(i). Next, a group of particles close to the separator simultaneously undergo fast lithiation, extracting lithium from the rest of the particles. As a result, the interparticle phase separation occurs at the cell DOD of 28%, where seven layers of particles are nearly fully lithiated, while the remaining 19 layers are nearly fully delithiated; see Fig. 3.3(ii). The process is repeated with the remaining delithiated particles. They lithiate in a fairly uniform manner (see Fig. 3.3(iii)), and then undergo interparticle phase separation. In the second interparticle phase separation that begins at 46% overall DOD, a group of six particles undergo fast lithiation, and subsequently the cell DOD rises to 50%; see Fig. 3.3(iv). The successive interparticle phase separation involves a smaller number of particles undergoing fast lithiation because the number of particles at intermediate concentrations becomes smaller.

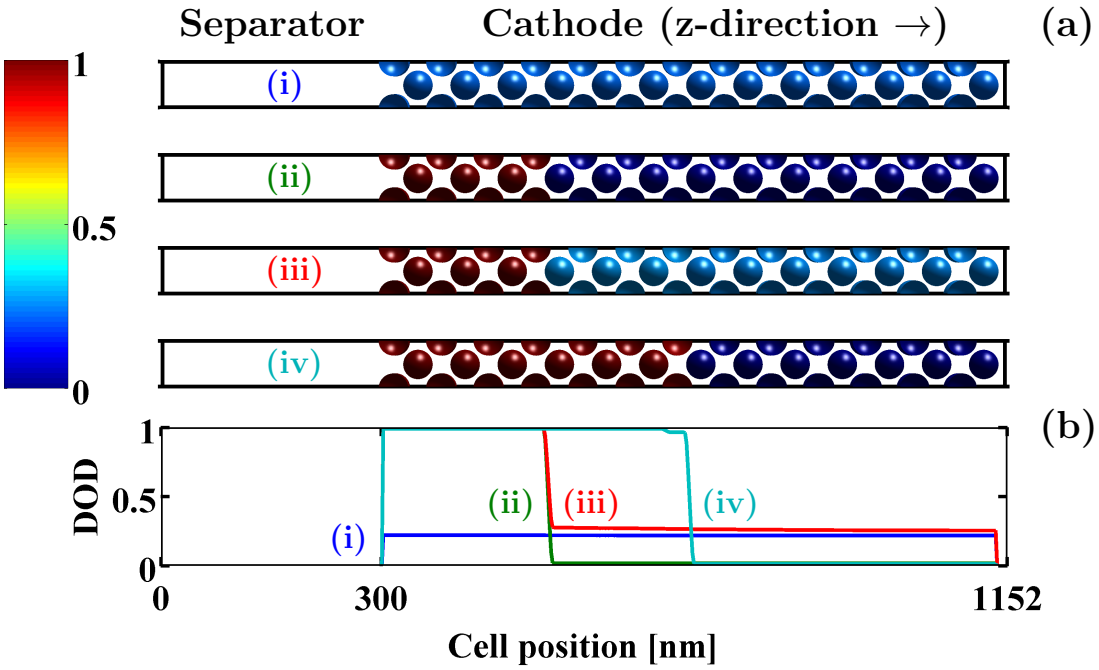

Figure 3.3: Dynamics observed during lithiation when i_0 is assumed independent of the activity of the cathode. (a) Surface Li concentration at four different times. (i) All particles lithiate in a nearly uniform manner (DOD = 22%). (ii) The particles closer to the separator transform to Li-rich phase, and the particles farther away return to a Li-poor phase (DOD = 28%). (iii) The Li-poor particles lithiate in a nearly uniform manner (DOD = 46%). (iv) Another group of particles transforms to the Li-rich phase, delithiating the remaining particles (DOD = 50%). Note that, because the process is reaction limited, each particle has nearly constant concentration (i.e., the surface concentration is approximately equal to the bulk concentration) (b) DOD averaged over the particle region in a cross section in the x-y plane.

The process observed, which we here refer to as a group-by-group interparticle phase separation, is now explained. After some initial concentration accumulation, the first mosaic instability begins. As mentioned before, the particles closer to the separator obtain a slightly higher DOD. Because of the non-monotonic potential, the particles with a higher DOD within the spinodal region have a larger driving force to lithiate. Thus, a small difference in the DOD of the particles is amplified initiating fast lithiation. The process of the first interparticle phase separation is shown in Fig. 3.4, where we can see how a small initial difference in the DOD of the particles is amplified, triggering the instability. The voltage rises due to the increasing equilibrium potential of the lithiating particles. Once $(\phi_p - \phi_e)$, which is nearly uniform throughout the cell at low currents, is higher than the equilibrium potential of the particles that are not lithiating, the non-lithiating particles become thermodynamically driven toward delithiation. Therefore, this leads a group of particles to reach a nearly fully lithiated and another group a nearly fully delithiated state. After the Li redistribution, the delithiated particles start lithiating again in a nearly uniform manner until the next interparticle phase separation is triggered, resulting in the intermittent group-by-group interparticle phase separation, in agreement with the results of Ferguson and Bazant [45], and Dargaville and Farrell [54].

During interparticle phase separation, the particles momentarily lithiate at a higher C-rate than the cell C-rate. In Fig. 3.5 we present the local C-rates at the corresponding DODs from Fig. 3.4. At the beginning of the group-by-group interparticle phase separation (DOD = 22% - 24%), the particles react at C-rates similar to the cell C-rate (i.e., the cross section C-rate/cell C-rate is close to one). When Li is redistributed between the particles (DOD = 26% - 28%), the particles that absorb lithium react at a much more rapid C-rate than the externally imposed cell C-rate.

Figure 3.6 shows the cell voltage profile during a lithiation-delithiation cycle, where the red and blue curves represent the lithiation and delithiation, respectively,

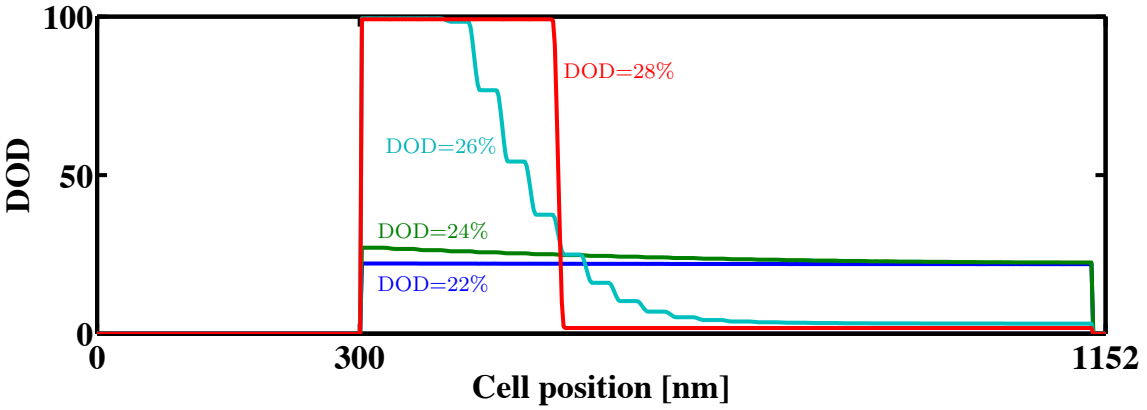

Figure 3.4: DOD (equivalent to Li concentration) averaged over the particle region in a cross section in the x-y plane for the cell DOD in the range from 22% (corresponding to Fig. 3.3(b)(i)) to a DOD of 28% (corresponding to Fig. 3.3(b)(ii)) with a 2% interval.

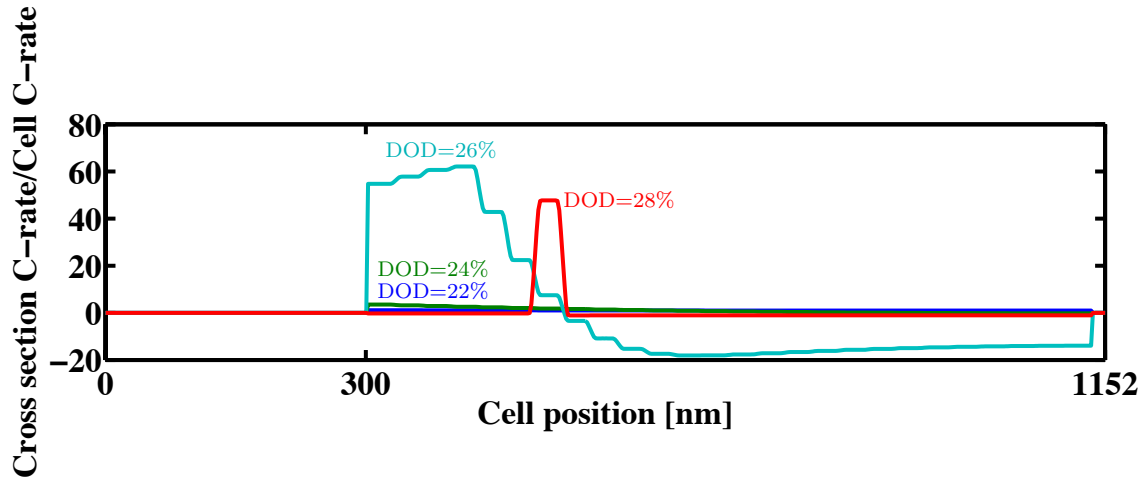

Figure 3.5: C-rate averaged over the particle region in a cross section in the x-y plane at the same DODs as in Fig. 3.4.

and the black curve represents the single-particle equilibrium potential. The two voltage curves are antisymmetric, and the magnitude of the overpotentials of the lithiation and the delithiation are the same when the DOD of the lithiation is equal to the state of charge (SOC $= 1 -$ DOD) of the delithiation. Five sudden rises and drops of the voltage curve during both lithiation and delithiation are observed, which correspond to five discrete phase transformation instabilities. The voltage fluctuates around the lower spinodal point during lithiation. Conversely, it fluctuates around the higher spinodal point during delithiation. This leads to a voltage hysteresis between lithiation and delithiation.

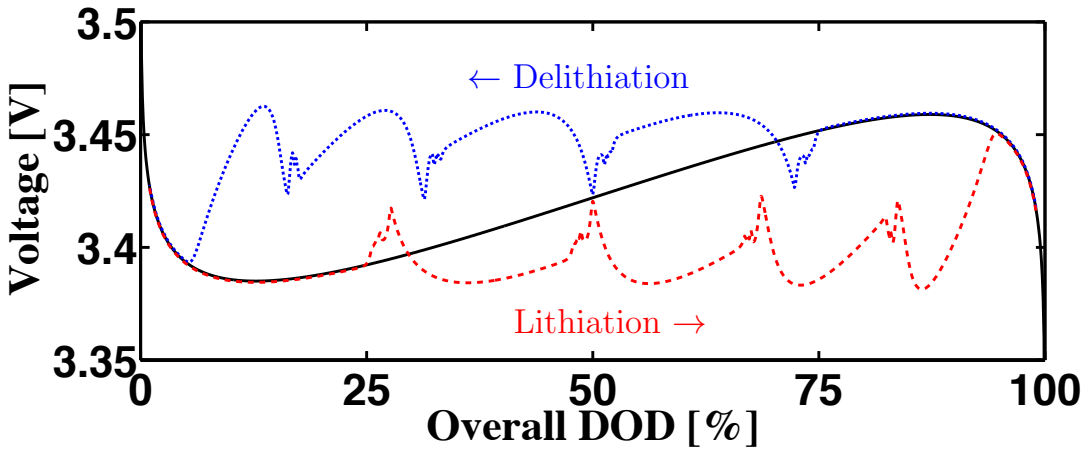

Figure 3.6: Voltage measured during lithiation and delithiation when i_0 is assumed independent of the activity of the cathode. The dashed red and dotted blue curves represent the voltage measured during lithiation and delithiation, respectively.

3.4.3 Lithiation and delithiation with activity-dependent exchange current density

Now, we include the dependence of the exchange current density on the activity of the particles as in Eq. (3.3). As will be shown later, this leads to significant asymmetric dynamics between lithiation and delithiation. In this set of simulations, we investigate how the applied current affects the particle interactions. Two different

aspects are analyzed in the following subsections: (A) the lithiation and delithiation dynamics and their corresponding voltage fluctuations, and (B) the concentration and electrostatic potential in the electrolyte.

Lithiation and delithiation dynamics and the corresponding voltage response

Here, we describe the lithiation and delithiation dynamics with an activity-dependent exchange current density in the Butler-Volmer equation. Note that in this section we only describe the dynamics observed, and the detailed analysis will be deferred to Sec. 3.5. Figures 3.7(a), (c), (e) present the voltage for lithiation and (b), (d), (f) for delithiation at different currents.

The lithiation dynamics is similar to the case where the current density is independent of the activity, presented in Sec. 3.4.2. In both cases, we observe group-by-group lithiation. Figure 3.7(a) shows the voltage curve for $\bar{i} = 2\%\ i_0'$ (C/12 rate), which is the same applied current as in the previous section. The voltage exhibits five primary spikes during this process, indicating five sets of interparticle phase separation. As mentioned in Sec. 2.1.1, purely based on the thermodynamics of the material, the phase separation is expected to occur at the spinodal point. However, significant deviations between the onset of the interparticle phase separation and the spinodal points are observed in our simulations. This deviation is referred to as the "concentration overshoot" hereafter. In Fig. 3.7(a), we observe that the interparticle phase separation occurs at 22% DOD (indicated by the gray vertical dashed lines), which is 9% DOD higher than the lower spinodal point at ∼13% DOD (indicated by the black vertical dashed lines). Figure 3.7(c) shows lithiation at $\bar{i} = 5\%\ i_0'$ (C/4.7 rate). Here, only three primary spikes in the voltage curve are present, indicating three sets of interparticle phase separation. From this observation, it can be deduced that each group contains more particles compared to the case where $\bar{i} = 2\%\ i_0'$. The concentration overshoot increases with an increasing magnitude of the current. In this

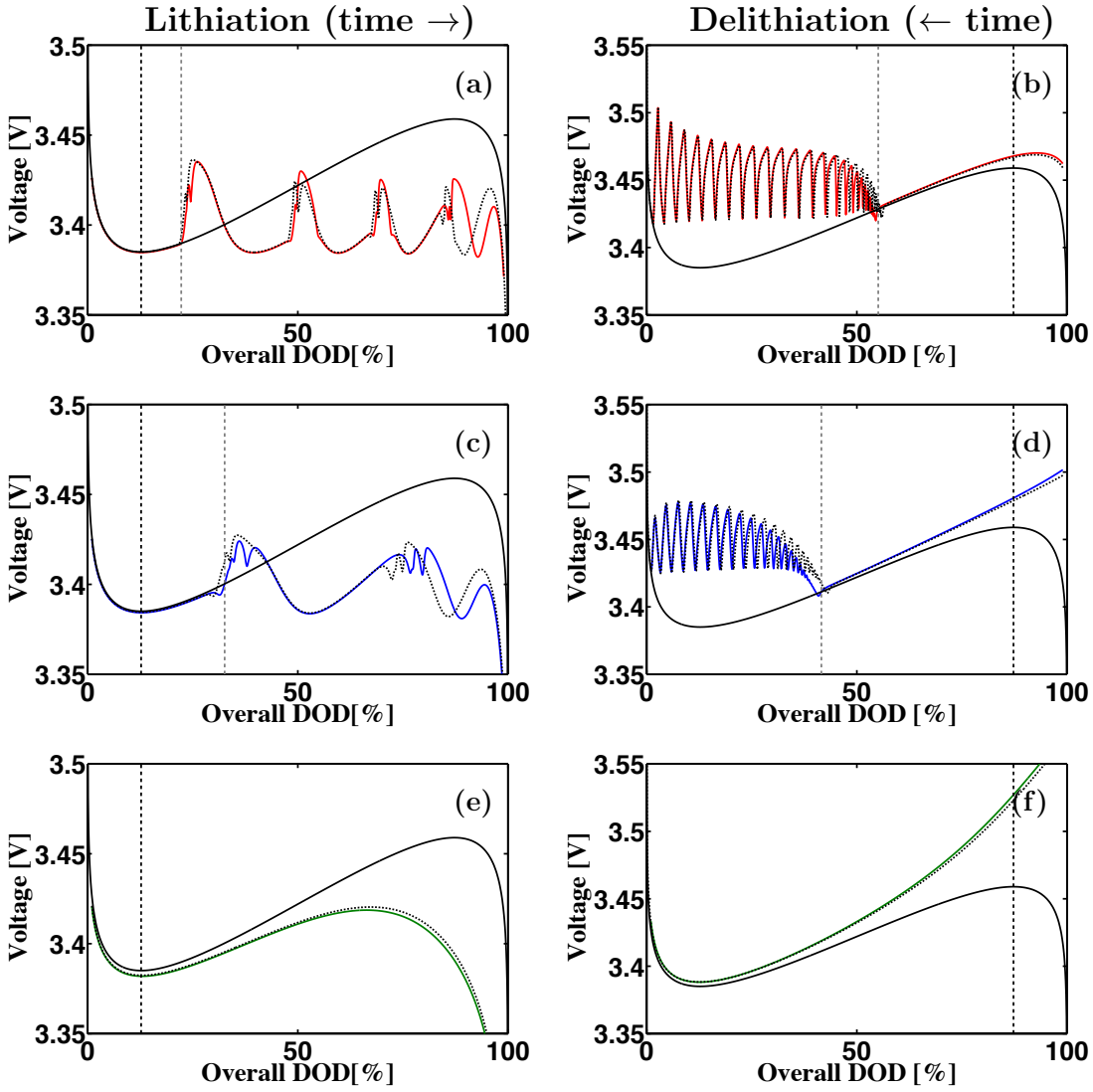

Figure 3.7: Voltage vs. overall DOD during lithiation (left) and delithiation (right) at different currents. (a) & (d) at $\bar{i} = 2\%\ i_0'$, (b) & (e) at $\bar{i} = 5\%\ i_0'$ and (c) & (f) at $\bar{i} = 20\%\ i_0'$. The black curve corresponds to the single-particle equilibrium potential, the color curves to the cells voltage and the dashed curves to the corresponding simulations using a porous electrode model, which are discussed in Sec. 3.6. The vertical black dashed lines indicate the lower and higher spinodal points during lithiation and delithiation, respectively. The vertical gray dashed lines the onset of the interparticle phase separation.

case, the interparticle phase separation begins at 33% DOD, which corresponds to a concentration overshoot of 20% DOD. At a sufficiently high current, all the particles in the computational domain lithiate together and the interactions between the particles are suppressed. This is shown in Fig. 3.7(e), which correspond to lithiation at $\bar{i} = 20\%\ i_0'$ (C/1.2 rate). In this case, there are no spikes in the voltage curve, showing no interparticle phase separation in the concentration evolution.

On the contrary, the dynamics during delithiation differs substantially. Figure 3.8 shows the snapshots of Li concentration evolution during delithiation at four different DODs also at $\bar{i} = 2\%\ i_0'$. The particles delithiate in a fairly even manner until reaching a DOD of around 59%; see Fig. 3.8(i). At this DOD, the first interparticle phase separation begins. At about 54% DOD, the first three layers of particles are fully delithiated and the particles far away from the separator start absorbing lithium from those close to the separator; see Fig. 3.8(ii). This is followed by particle-by-particle delithiation in the computational domain (which is equivalent to a layer-by-layer transformation because of the periodic boundary condition along the x- and y-directions), initiating from the separator-cathode boundary and moving toward the cathode current collector; see Fig. 3.8(iii) at 48% DOD. Such a layer-by-layer phase-front movement continues until the entire cell is fully delithiated. Figure 3.8(iv) shows the concentration at 30% DOD. The voltage curve for delithiation at this current is shown in Fig. 3.7(b), where each spike corresponds to a fast delithiation event of one particle layer. Here, the interparticle phase separation occurs at 55%, which corresponds to a concentration overshoot of 32% DOD. At $\bar{i} = 5\%\ i_0'$, the interparticle phase separation occurs at DOD of 42% and therefore the overshoot is 45% DOD in magnitude (= $\sim$87% DOD at higher spinodal - 42% DOD at first interparticle phase separation) ; see Fig. 3.7(d). Unlike lithiation, the larger overshoot does not affect the number of particles undergoing fast lithiation because it still occurs as a layer-by-layer interparticle phase separation. At a sufficiently high current the interparticle

phase separation is also suppressed; see Fig. 3.7(f) at $\bar{i} = 20\%\ i_0'$.

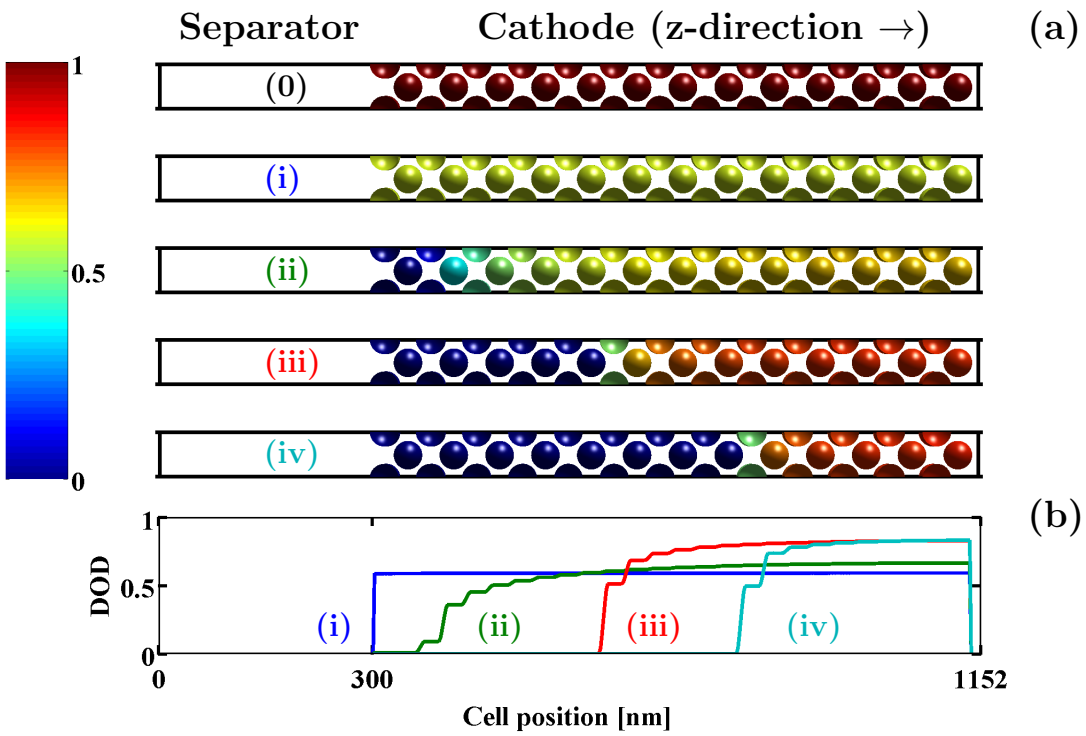

Figure 3.8: Delithiation with exchange current density dependent of DOD. (a) Surface Li concentration of each individual particle layer. (0) Initial condition at DOD = 98%. (i) All the particles delithiate in a fairly uniform manner (DOD = 59%). (ii) The particles closer to the separator fully delithiate, releasing lithium that is absorbed by the remaining particles, some of which will return to a nearly fully lithiated state (DOD = 54%). (iii) More particles become fully delithiated and the particles that were absorbing lithium return to a Li rich phase (DOD = 48%). (iv) The particles continue to delithiate layer by layer (DOD = 30%). As in Fig. 3.3, the surface concentration approximates the bulk concentration. (b) DOD averaged over the particle region in a cross section in the x-y plane.

Concentration and Electrostatic Potential of the Electrolyte

Now, we analyze the effect of the interparticle phase separation on the concentration and the electrostatic potential of the electrolyte. For this purpose, we consider lithiation and delithiation at $\bar{i} = 2\%\ i_0'$. In Figs. 3.9(a) and (b), the voltage for lithiation and delithiation, respectively, is shown again, along with markers noting the

different states examined in this analysis. Figures 3.9(c) and (d) show the profiles of the electrolyte concentration at four different times during lithiation and delithiation, respectively. The curves are represented with the average concentration in the electrolyte on each slice of the x-y planes.

During lithiation before the interparticle phase separation occurs, the electrolyte concentration decreases gradually from the separator to the cathode current collector; see Fig. 3.9(c) curve (i). When the first interparticle phase separation takes place, Li is absorbed rapidly on the particles near the separator, causing the electrolyte concentration in the surrounding region to drop. Meanwhile, the particles closer to the cathode current collector eject Li resulting in a rise in the electrolyte concentration of that region. Consequently, a concentration increase from the cathode current collector side to the anode side is observed; see Fig. 3.9(c) curve (ii). After the first interparticle phase separation, the electrolyte concentration returns to a similar state as prior to the instability; see Fig. 3.9(c) curve (iii). In the second interparticle phase separation, the number of particles undergoing fast lithiation and the number of particles releasing Li is reduced. As a consequence, both the rise and drop in the electrolyte concentration is reduced. Furthermore, the particles undergoing fast lithiation are located closer to the cathode current collector, causing the location of the concentration increase to also be shifted. In addition, the number of particles releasing Li is reduced. As a consequence, both the rise and the drop in the electrolyte concentration are reduced in magnitude and occur closer to the cathode current collector; see Fig. 3.9(c) curve (iv). The subsequent interparticle phase separation is accompanied by smaller variations with the transition moving closer to the cathode current collector.

For the delithiation process, the electrolyte concentration curve before the first mosaic instability is smooth, but has a slope with an opposite sign from that of lithiation, since the flow of ions is in the opposite direction; see Fig. 3.9(d) curve (v). In the first interparticle phase separation, the electrolyte concentration near the an-

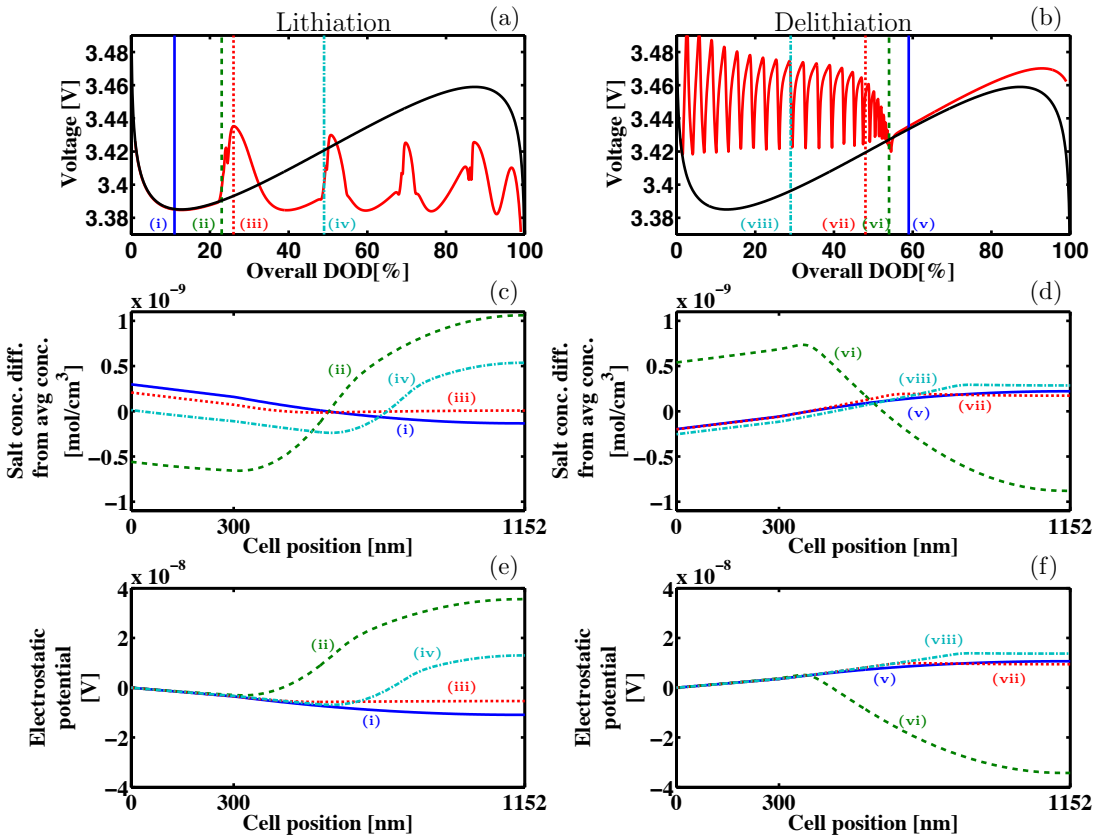

Figure 3.9: (a) & (b) Cell voltage during lithiation and delithiation, respectively at $\bar{i} = 2\%\ i_0'$. The vertical lines indicate the DODs at which concentration and electrostatic potential of the electrolyte are measured. (c) & (d) Electrolyte concentration difference from the average concentration over the electrolyte region in a cross section in the x-y planes during lithiation and delithiation, respectively. (e) & (f) Electrostatic potential over the electrolyte region in a cross section in the x-y planes during lithiation and delithiation, respectively. The electrostatic potential at the anode is taken to be 0 V as a reference. For lithiation, (i) the solid blue line corresponds to 11% DOD, (ii) the green dashed line to 23% DOD, (iii) the red dotted line to 49% DOD and (iv) the cyan dashed-dotted line to 68% DOD. For delithiation, the same DODs as in Fig. 3.8 are used: (v) the solid blue line corresponds to 59% DOD, (vi) the green dashed line to 54% DOD, (vii) the red dotted line to 48% DOD and (viii) the cyan dashed-dotted line to 30% DOD.

ode rises while the concentration near the cathode current collector decreases; see Fig. 3.9(d) curve (vi). During the remainder of the delithiation, the concentration becomes nearly constant near the cathode current collector. This is because the Li concentration in the particles away from those that are reacting remain relatively unaffected during the subsequent interparticle phase separation events. As previously described, the layer-by-layer phase-front moves continuously during delithiation, resulting in a continuous movement of the transition region of the concentration curve, where the slope changes rapidly; see Fig. 3.9(d) curves (vii) and (viii).

We now describe the electrostatic potential in the electrolyte. Figure 3.9(e) shows the electrostatic potential for lithiation. The same states (i)-(iv) as in the electrolyte concentration are presented here. The behavior of the electrostatic potential matches qualitatively with that from the electrolyte concentration. The only difference is that all the curves align at the anode because the potential at the anode is set to 0 as the boundary condition. Similar explanations as for the electrolyte concentration can be used to describe the behavior of the electrostatic potential. The absorption of Li ions from the electrolyte into the particles causes not only a decrease in the electrolyte concentration, but also a decrease in the electrostatic potential. As observed in Eq. (2.8a), this relation is maintained away from the interfacial regions as long as $(D_+ - D_-)$ is negative. During the interparticle phase separation, some of the particles extract lithium into the electrolyte, locally increasing the electrostatic potential in a similar way as observed with the electrolyte concentration. Figure 3.9(f) presents the electrostatic potential during delithiation also at the same times (v)-(viii) as for the electrolyte concentration. An analogous explanation applies for delithiation.

3.5 Analysis

Here, we analyze and further discuss the results presented in the prior sections, primarily focusing on cases where the exchange current density is dependent on the

cathode activity, unless otherwise noted. Three different aspects are included in this analysis: (A) the origin of the concentration overshoot, (B) the determinant of the group size in lithiation, and (C) the origin of the asymmetry in lithiation and delithiation behavior.

3.5.1 Concentration overshoot

As described in Sec 3.4.3, a larger concentration overshoot occurs during delithiation in comparison to lithiation, and in both cases the overshoot increases with current. Now, we perform a simplified analysis to illustrate the origin of this change. For this analysis, we assume a cell in which a group of particles reacts uniformly and one adjacent particle has a different concentration from the rest. We will denote the particle as "particle A." In this hypothetical cell, there is a significant amount of particles such that the DOD of particle A does not affect the DOD of the cell. In order for the group of particles with uniform Li concentration to lithiate at a given current, an applied voltage, "V_x," is required. At the same time, the adjacent particle must have a single-particle equilibrium potential lower than V_x to have a driving force for delithiation while the other particles are lithiating. The Li concentration of the particle at which this occurs can be determined by the intersection of the single-particle equilibrium potential curve and a horizontal line of value V_x. This construction is shown in Fig. 3.10(a) for (de)lithiation at $\bar{i} = 20\%\ i_0'$. The curves for lithiation and delithiation are different because of the activity dependent i_0 (Fig. 3.2).

We now describe the composition difference required for the initiation of the inter-particle phase separation during lithiation and delithiation. As previously mentioned, in order for particle A to delithiate while the group of particles lithiates, particle A must have an equilibrium potential lower than V_x. Thus, the lengths of line (i) and line (iv) in Fig. 3.10(a) represent the composition difference required at the first DOD

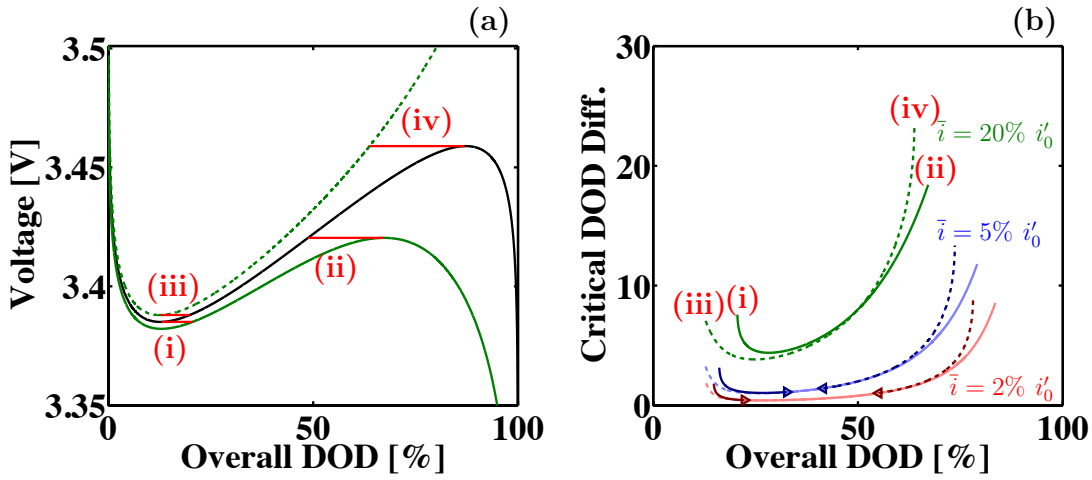

Figure 3.10: (a) Applied voltage for lithiation and delithiation at $\bar{i} = 20\%\ i_0'$ represented by the solid green curve and the dashed green curve, respectively. The minimum DOD difference required for the interparticle phase separation to begin (i)-(ii) during lithiation, and (iii)-(iv) during delithiation is here indicated. The black curve represents the single-particle equilibrium potential. (b) Minimum DOD difference as a function of the overall DOD for $\bar{i} = 2\%\ i_0'$, $\bar{i} = 5\%\ i_0'$ and $\bar{i} = 20\%\ i_0'$, represented here by a red, blue and green curve, respectively. Right-pointing and left-pointing triangles represent the first interparticle phase separation during lithiation and delithiation, respectively. The darker curves represent the DODs before the interparticle phase separation occurs, while the lighter curves indicate the regions after it occurs. The solid curve represents lithiation and the dashed curve delithiation.

at which the interparticle phase separation is possible for lithiation and delithiation, respectively. For lithiation, the concentration of the cell is indicated by the right end of line (i) (21% DOD) while the corresponding concentration of the particle A must be at the left end of line (i) (13% DOD). Therefore a composition difference of 8% DOD is required in order for the interparticle phase separation to take place. The interparticle phase separation could not occur at a cell DOD smaller than 21% since the applied voltage below that composition is outside the inverted potential range of the single-particle equilibrium potential. For delithiation, the initial concentration of the cell is indicated by the left end of the line (iv) (64% DOD) and the concentration of the lithiating particle by the right end of the line (41% DOD), therefore a composition difference of 23% DOD is required for the interparticle phase separation to begin. By comparing lithiation to delithiation, the following is observed: First, the DOD at which the interparticle phase separation can occur is farther away from the spinodal points during delithiation compared to lithiation. Second, once the interparticle phase separation can occur, it also requires a larger concentration difference in delithiation compared to lithiation. These two reasons make the concentration overshoot in delithiation larger. However, phase separation within the particles, if allowed, would diminish the concentration overshoot and the asymmetry between lithiation and delithiation discussed above.

Now, we compare the critical concentration difference at different currents. Figure 3.10(b) shows the critical composition difference as a function of the cell DOD for the three different applied currents for lithiation and delithiation. The curves are calculated based on the difference between the equilibrium potential and the theoretical (de)lithiation voltage of the particles in the absence of interparticle phase separation, as described above. Again, the difference between lithiation and delithiation originates from the activity dependence of i_0. The darker curves indicate the ranges of the cell DOD before the onset of the interparticle phase separation relevant for the simu-

lations presented earlier, while the lighter curves indicate the theoretical calculations beyond the onset of the interparticle phase separation. The right- and left-pointing triangular markers on the blue and red curves indicate the points of onset of the first interparticle phase separation in lithiation and delithiation, respectively. The required composition difference increases as the loading current increases, and thus the composition at which the interparticle phase separation can first occur deviates farther from the spinodal points. As a consequence, a larger concentration overshoot occurs with a higher current. Note that, even though the interparticle phase separation could occur at $\bar{i} = 20\%\ i_0'$, it does not occur if the required composition difference is not reached (as is the case in our simulation). Thus, the analysis provides only the minimum overshoot required, not the actual overshoot. If the applied current is high enough such that the cell voltage is outside the inverted potential range (where the interparticle phase separation, i.e., full and empty particles, is favored), the interparticle phase separation will be suppressed, independent of the composition differences.

3.5.2 The determinant of the group size in lithiation

Having established qualitatively the relationship between the concentration overshoot and the current, we now present an analysis to determine the fraction of particles reacting during each interparticle phase separation for a given concentration overshoot. Note that this analysis is rate independent and in here the transport of the electrolyte is assumed not to be a limitation. As previously described, during the interparticle phase separation upon lithiation, the particles with a Li concentration in the spinodal region (the "unstable particles") redistribute Li with each other. By such redistribution process, the particles reach either an almost fully lithiated or an almost fully delithiated state. At the onset of the interparticle phase separation, the particles outside the spinodal region (the "stable particles") are only those that have already undergone fast lithiation. Thus, we assume that the stable particles have a DOD

of 100%. Given the DOD of the cell, DOD_{cell}, the average DOD of the unstable particles, $DOD_{unstable}$, can be approximated from the expression

$$\frac{N_{stable}}{N_{tot}}100\% + \frac{N_{unstable}}{N_{tot}}DOD_{unstable} = DOD_{cell}, \tag{3.8}$$

where N_{stable}, $N_{unstable}$ and N_{tot} are the number of stable, unstable and total particles, respectively. Next, we choose DOD_{cell} at which we can approximate the DOD of the lithiating and delithiating particles. This point corresponds to the DOD at which the voltage peaks occur. If several small peaks occur as part of one main interparticle phase separation event, we take the latest one, as this is the point when concentration can be best approximated. As illustrated in Sec. 3.4.1 (see Figs. 3.1(b) and (c) point (iv)), at this DOD the lithiating particles are close to the higher spinodal point (∼87% DOD). The actual location of the peak depends on the magnitude of the applied current and the number of particles reacting. Due to the activity dependence of i_0, the voltage peak shifts to lower DODs at higher currents. However, for simplicity in the calculation, we ignore this shift. The delithiating particles are at a low concentration that we refer as DOD_{LC} (∼0% at the DOD of Fig. 3.1(b) point (iv)). The concentration of the delithitated particles depends on the height of the voltage peaks, as their equilibrium potential has to remain lower than the applied voltage. DOD_{LC} is here approximated as the DOD at which the equilibrium potential below the spinodal point is equal to the applied voltage.

The fraction of unstable particles that lithiate simultaneously in a given group can be therefore approximated as

$$\frac{N_{group}}{N_{unstable}} = \frac{DOD_{unstable} - DOD_{LC}}{DOD_{HS} - DOD_{LC}}, \tag{3.9}$$

where N_{group} is the number of particles in the group, and DOD_{HS} the DOD of the higher spinodal. Substituting Eq. (3.9) into Eq. (3.8), the fraction of particles that

react simultaneously can be expressed as

$$\frac{N_{group}}{N_{unstable}} = \frac{N_{tot}DOD_{cell} - N_{stable} - N_{unstable}DOD_{LC}}{N_{unstable}(DOD_{HS} - DOD_{LC})}. \tag{3.10}$$

The predictions from this analysis and from our simulations with an activity-dependent i_0 are provided in Table 3.1 for comparison. Note that this analysis could also be used for lithiation with an activity-independent i_0, and a similar analysis could be performed for delithiation with an activity-independent i_0. In the earlier groups (1^{st}-3^{rd} in the case of $i = 2\%\ i_0'$ and 1^{st}-2^{nd} in the case of $i = 5\%\ i_0'$), the estimated fractions are in good agreement with the simulations. However, in the later groups, the estimates are less accurate. There are two primary reasons for this disagreement. (1) The small number of remaining unstable particles limits the results of the fractions in simulations, for example there are only two particles in the 5^{th} group of $i = 2\%\ i_0'$ and therefore the resulting fraction can only take values of either 50% or 100%. (2) Because of the smaller number of particles reacting in the later groups, those particles undergo fast lithiation at a higher rate, which makes the shift of the voltage peak larger. For example, the DOD at which the voltage peaks in the case of $i = 2\%\ i_0'$ for the first group is ∼84% while for the last group is ∼64%. With the consideration of this deviation, the calculated fraction of particles reacting in the last group increases from 63% to 87%, which is closer to the fraction observed in the simulation.

3.5.3 Origin of the asymmetry in lithiation and delithiation behavior

In this section, we elucidate the origin of the asymmetry of the interparticle phase separation during lithiation and delithiation when the current is sufficiently low, observed in Sec. 3.4.3. This asymmetry is a manifestation of a competition between two processes that occur simultaneously: (1) an intermittent Li redistribution among the particles and (2) a constant (de)lithiation of the cell due to the externally applied voltage (which is varied to maintain the desired current). Which of these processes

Applied current	Group number	Cell DOD	Predicted fraction	Fraction in simulations
$\bar{i} = 2\%\ i_0'$	1^{st}	26%	29%	31% (8/26)
	2^{nd}	51%	32%	33% (6/18)
	3^{rd}	70%	39%	41% (5/12)
	4^{th}	87%	59%	71% (5/7)
	5^{th}	97%	63%	100% (2/2)
$\bar{i} = 5\%\ i_0'$	1^{st}	40%	45%	46% (12/26)
	2^{nd}	81%	73%	78% (11/14)
	3^{rd}	94%	57%	100% (3/3)

Table 3.1: Fraction of the unstable particles that react simultaneously obtained by the calculation presented here, compared to the fraction observed in the simulations.

becomes dominant depends on the value of i_0, the exchange current density.

To illustrate these two processes and the resulting dynamics, we conduct simulations including only one of the processes. The insight gained is employed to facilitate our understanding of the origin of the asymmetric dynamics. First, to analyze Li redistribution among the particles without an applied current, we conduct a simulation in which a cell is relaxed with a nearly uniform DOD of 22% (taken from the partially lithiated cell with an activity independent i_0 and $\bar{i} = 2\%\ i_0'$, presented in Sec. 3.4.2; see Fig. 3.3(a)(i)). During the process of relaxation, a cell voltage is imposed to maintain a zero net current through the current collectors. Shown in Fig. 3.11(a) is the cell voltage during the relaxation. Throughout the relaxation, where five particles reach a lithiated state and 21 particles a delithiated state, one primary sudden rise of the voltage occurs as a consequence of changing the Li concentration of the particles and their corresponding equilibrium potential. This shows a natural tendency for the system to transit from an activated unstable state with partially lithiated particles to a coexistence of lithium rich and lithium poor particles. Note that the shape of the voltage rise and drop observed in relaxation is very similar to those observed during lithiation at $\bar{i} = 2\%\ i_0'$ with an activity independent i_0.

Next, we focus on the effect of the applied current by prohibiting an opposing

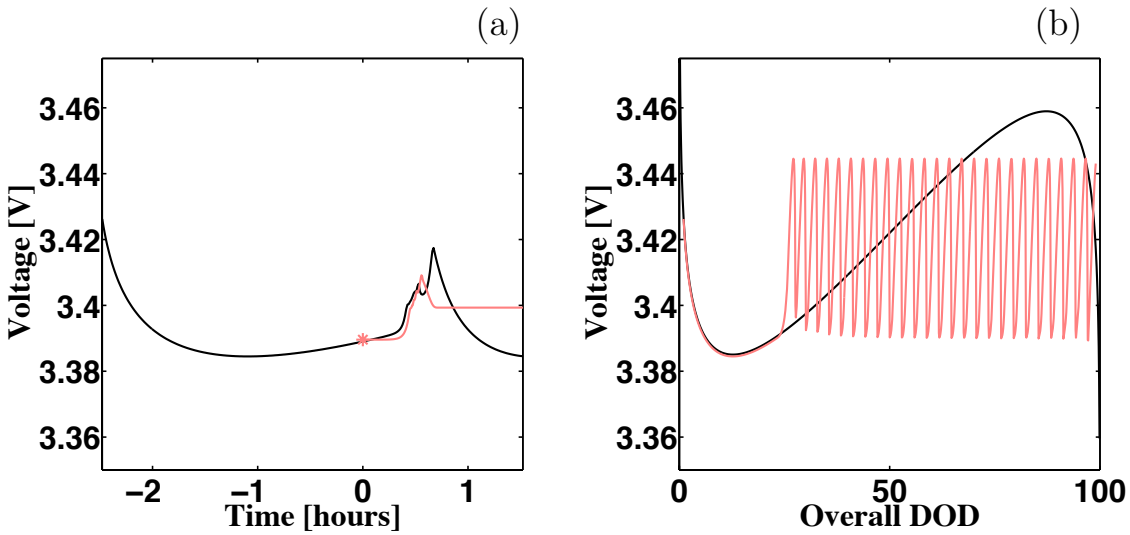

Figure 3.11: (a) Relaxation of a cell with a DOD of 22%. The light red curve represents the voltage of the relaxed cell. The black curve indicates the voltage of the lithiating cell at $\bar{i} = 2\%\ i_0'$ where i_0 is activity independent (corresponding to the data shown in Fig. 3.6 in the range from 1% to 35% DOD). The light red asterisk indicates the beginning of the relaxation of the cell. (b) Lithiation of the cell at $\bar{i} = 2\%\ i_0'$ where i_0 is activity independent and all the backflow fluxes from the particles to the electrolyte are hindered. The light red curve indicates the voltage of the cell and the black curve the single-particle equilibrium potential.

reaction (i.e., Li back-flow into the electrolyte during lithiation of the cell),

$$r_{Li} = \begin{cases} r_{Li}^{BV} & \text{if } \; r_{Li} \geq 0 \\ 0 & \text{if } \; r_{Li} < 0, \end{cases} \tag{3.11}$$

where r_{Li}^{BV} is the reaction rate defined by the Butler-Volmer equation (Eq. (2.37)). The simulation is conducted at $\bar{i} = 2\%\ i_0'$, and i_0 is activity independent. The resulting voltage response indicates that the rapid lithiation occurs one particle at a time. We observe 26 sudden rises (and drops) of the voltage, corresponding to the fast lithiation of the 26 particles; see Fig. 3.11(b). The process begins in the same manner as the case when the back-flow is allowed (described in Sec. 3.4.2). The lithiation increases the DOD of the particles nearly uniformly. Upon reaching the concentration overshoot to trigger the first interparticle phase separation, the first particle begins lithiating rapidly. However, because delithiation is prohibited here, the current is a result of lithiation reaction only, which needs to be slower than the case where delithiation accompanies the process. Thus, a higher voltage, which reduces the lithiation reaction rate, is observed in Fig. 3.11(b). The peaks in this figure are higher than those observed in Fig. 3.6. This larger voltage during fast lithiation leads to a more rapid amplification of the concentration gradient and particle-to-particle variation of the driving force for lithiation. This amplification causes the "runaway" reaction of a particle and consequently a particle-by-particle interparticle phase separation. The lithiation of the subsequent particle can only occur when the rapidly lithiating particle is nearly fully lithiated and the cell voltage decreases to a value below the equilibrium potential of the next particle. This process is repeated and, as a result, the lithiation proceeds in a layer-by-layer manner.

With the background provided by the discussion of the two processes above, we elucidate mechanisms that lead to the observed asymmetric dynamics in our simulations for the case with the activity-dependent i_0. During lithiation, the particles

undergo interparticle phase separation in a group-by-group manner, similarly to the case of an activity-independent i_0 presented in Sec. 3.4.2. The dynamics of this interparticle phase separation strongly resembles that of relaxation, showing that Li redistribution is significant in this case. During the interparticle phase separation, the delithiation of the particles is strongly facilitated by a "sufficiently large" value of i_0 for the particle DOD in the range between an almost fully delithiated state and the onset of the interparticle phase separation. Here, we denote that i_0 is sufficiently large when the value for the particles toward delithiation is similar to or larger than that toward lithiation, at the onset of the interparticle phase separation. In other words, i_0 must be large enough to facilitate delithiation during the lithiation process. Note that this condition for i_0 is met for the lithiation simulations in the previous sections with both activity-dependent and activity-independent exchange current density, as well as for delithiation with activity-independent i_0; see Fig. 3.2. In those cases, Li redistribution readily occurs and is the dominant mechanism for the dynamics of the interparticle phase separation.

In contrast, the delithiation behavior for an activity-dependent i_0, which shows layer-by-layer dynamics, resembles the case of prohibited Li redistribution. At the onset of interparticle phase separation upon delithiation, because the tendency for a particle to lithiate when a neighboring particle delithiates is weak due to the value of i_0 (see Fig. 3.2), the Li redistribution is hindered. As a result, when a lithiated particle undergoes fast delithiation and causes a voltage drop, other lithiated particles remain at a fairly constant concentration close to the higher spinodal point, without returning to the nearly fully lithiated state. The only exception is the initial interparticle phase separation in which the concentration overshoot is larger and therefore some redistribution occurs. The redistribution is kinetically hindered by the exchange current density at a concentration close to the higher spinodal point. Thus, the fast delithiation of a particle corresponds mostly to the constant extraction of Li out of the

cathode without intermittent redistribution of Li between the particles. This results in a layer-by-layer interparticle phase separation, similar to the simplified case where no opposing reaction was allowed.

In summary, our analysis indicate that, because of the asymmetric function of exchange current density, Li redistribution is facilitated upon lithiation of the cell, while redistribution is limited upon delithiation. This difference manifests as a group-by-group interparticle phase separation during lithiation, a thermodynamically favored behavior, and a layer-by-layer interparticle phase separation during delithiation, a kinetically controlled behavior. Note that, besides an asymmetric i_0, other factors such as an asymmetric equilibrium potential as the one presented by Malik et al. [19] or a transfer coefficient with a value different from 0.5 also lead to asymmetric dynamics [62].

3.6 Comparison to the Porous Electrode Model

In this section, we compare our results with those obtained by Ferguson and Bazant using a porous electrode model [45]. For this comparison, the simulation parameters in the porous electrode model were set effectively equal to those in our particle-level simulation and the equations described below were used.

The porous electrode model used is in the pseudocapacitor limit. That is, transport in the solid is fast compared to surface reactions and transport in the electrolyte. For nanoparticles, this approximation is reasonable. This allows the concentration profiles inside the particles to be neglected, and the particles can be treated as sink terms. Since the model averages over the volume of the electrode, what is referred to as a particle is actually a representative particle for that volume of the electrode, and all solid particles inside that volume are assumed to behave the same. The

accumulative Li concentration, $\overline{C_p}$, can be determined by the reaction rate:

$$\frac{\partial \overline{C_p}}{\partial t} = \tilde{a}_v r_{Li}. \tag{3.12}$$

where t is time and $\tilde{a}_v$ is the area to volume ratio of the particles. This equation governs the lithiation of the particles and substitutes Eq. (2.5) and (2.6) of our model. Here, 26 of these "particles" (i.e., volumes of particles) are considered within the cathode.

The average porosity of the electrode, ϵ, defined as volume fraction of electrolyte with respect to the total volume of the cathode, is used to obtain the effective diffusivity and conductivity of the porous media via the Bruggeman empirical relation. In a one-dimensional domain, the electrolyte concentration evolution is described by

$$\epsilon \frac{\partial C_e}{\partial t} = \frac{\partial}{\partial z}\left(\epsilon D_{amb} \frac{\partial C_e}{\partial z}\right) - (1 - t_+)\tilde{a}_p r_{Li}, \tag{3.13}$$

where D_{amb} is the ambipolar diffusivity, t_+ is the transference number of the cation, and $\tilde{a}_p$ is the particle area to electrode volume ratio. Two primary differences between this equation and the original equation (Eq. (2.55)) can be noticed. First, instead of spatially resolving the electrolyte that fills the electrode, the electrolyte concentration is averaged over the volume. Second, the particle surfaces are no longer explicitly defined, and are replaced by a given value of particle surface area.

In order to express the current density, we also need to account for the porosity, and therefore the original equation (Eq. (2.7)) is modified to include this factor,

$$i = -z_+ \upsilon_+ F\left[\frac{F}{RT}(z_+ D_+ - z_- D_-)\epsilon C_e \frac{\partial \phi_e}{\partial z} + (D_+ - D_-)\epsilon \frac{\partial C_e}{\partial z}\right]. \tag{3.14}$$

where υ_+ is the number of cations produced by the electrolyte dissociation, F is Faraday's constant, and ϕ_e is the electrostatic potential of the electrolyte. Furthermore, z_i is the charge number and D_i is the diffusivity of ith species. Lastly, the current

continuity equation (Eqs. (2.8a)-(2.8b)) becomes

$$\frac{\partial i}{\partial z} = r_{Li} F \tilde{a}_p. \tag{3.15}$$

Here, it is assumed that the reaction occurs throughout the entire porous electrode. Detailed explanations of this model can be found in Ferguson and Bazant's work [45].

The porous electrode models are computationally efficient and often capture the dynamical nature of the charge and discharge process within a relatively simple description. However, the simplification leads to a disadvantage that they do not directly allow investigation of microstructural details and resulting effects since they only consider average properties. Thus they require validation and examination of the limit of applicability. Figures 3.7(a)-(f) show the comparisons between the porous electrode simulation (dashed curves) and the SBM simulations (solid curves). The two results are in remarkable agreement. They both capture the interparticle phase separation events observed in the process, have a similar concentration overshoot and predict different dynamics between lithiation a delithiation. However, there is a small difference in the magnitude of the overpotential between the two simulations. This difference leads to a disagreement between the later mosaic instabilities during lithiation, and between the onsets of the first instabilities during delithiation. These differences can be attributed to various approximations involved in each method. On one hand, an artificial finite thickness is assigned to the particle-electrolyte interface in the SBM, and on the other hand, several simplifications are taken in the porous electrode model as described above. Both methods carry some degrees of small errors that, at the end, leads to the disagreement. For the error analysis in the SBM, one can find the information in the work of Yu et al. [2].

The above analysis demonstrates that the models from the two different length scales accurately describe the same physical phenomenon of interparticle phase separation. Note that the agreement between the two models is partly due to the sim-

plicity of the microstructure used here. These two models compliment each other: The particle-level model allows us to study more detailed electrochemical dynamics accounting for the complexity of microstructures [63], which would not be revealed in a homogeneous porous electrode model. The porous electrode model allows us to study much larger cells, such as those from a commercial battery, which is not currently feasible with particle-level simulations.

3.7 Conclusion

In this chapter, we have investigated the behavior of an array of single-sized particles that are not allowed to generate a phase boundary within a particle, despite the bulk thermodynamic driving force to do so. Interparticle phase separation is observed when the current is sufficiently low. Through analysis, the concentration overshoot was explained, and the group sizes of the interparticle phase separation were predicted. Further careful examination elucidated the competition of two mechanisms: thermodynamic relaxation that leads to Li redistribution and to group-by-group phase transformation, and kinetically induced layer-by-layer phase transformation. The asymmetry between lithiation and delithiation is attributed to the exchange current density model, appearing in the modified Butler-Volmer equation. We also compared our simulation with the porous electrode model of Ferguson and Bazant [45], which showed excellent agreement and provided further insights into the mechanism underlying the lithiation/delithiation dynamics, resulting from the model.

CHAPTER IV

INTERPARTICLE VS. INTRAPARTICLE PHASE SEPARATION

4.1 Introduction

In this chapter, we study the interaction kinetics between nanoparticles. Both interparticle phase separation and intraparticle phase separation are examined. A comparison between these two types of interactions offers critical insights that can help the experimental identification of the prevalent interaction that occurs in cells. In a collection of particles with a wide size distribution, particles that remain monophasic are likely to coexist with particles that undergo intraparticle phase separation because the tendency to suppress intraparticle phase separation is size dependent. If the phase separation were suppressed by non-bulk thermodynamics, particles would be expected to remain monophasic below a critical size, whereas particles would be expected to phase separate within themselves above that size, independent of the C-rate (or equivalently current density, in this context). In contrast, if the phase separation is kinetically suppressed, this threshold would be C-rate dependent [20]. The precise phase-transformation path for nanoparticulate $LiFePO_4$ has not yet been identified, and the literature contains conflicting claims [12, 15, 14, 16, 13, 19].

To investigate the kinetics of the particle interactions, we simulate the lithiation of a cell containing only two particles of different sizes. This simple configuration allows us to clearly identify the details of the lithiation process, which would be difficult to isolate if more particles were present. Here, a parametric study is conducted, in which

we vary the interfacial energies to alter the tendencies of intraparticle phase separation. First, we investigate the dynamics of interparticle phase separation. Then, we analyze that of intraparticle phase separation. Finally, we consider the special case in which intraparticle phase separation is suppressed only in the smaller particle. Even though the cell considered here is geometrically and microstructurally simple, the resulting dynamics provide valuable insights that lead to better understanding of multiparticle battery kinetics.

4.2 Model

The electrochemical model is here reduced to two coupled equations: (1) concentration evolution in the electrode particles and (2) reaction that occurs at the particle-electrolyte interfaces. We assume that the particles are electronically well connected via conductive coatings and additives, such that the electrostatic potential in the particles, ϕ_p, is uniform throughout the particles. We also consider the electrolyte concentration, C_e, and its electrostatic potential, ϕ_e, to be uniform. These assumptions are well justified because the size of the cell is very small.

To model the concentration evolution in the particles, we use the Cahn-Hilliard equation (Eq. (2.3)), where the reaction rate serves as a boundary condition at the particle-electrolyte interface (Eq. (2.6)). The gradient coefficient $\boldsymbol{\kappa}$ in Eq. (2.3), is here a tensor as we consider anisotropic interfacial energies,

$$\boldsymbol{\kappa} = \begin{bmatrix} k_x & 0 & 0 \\ 0 & k_y & 0 \\ 0 & 0 & k_z \end{bmatrix}. \tag{4.1}$$

The bulk chemical potential, μ_b, is obtained by a polynomial fit [38] of the single-

particle equilibrium potential calculated from first principles [19],

$$-\mu_b/F = \{\left[5(1.02-2.04X_p)^{51} - 2.925275X_p^2 + 6.375071X_p - 2.558325\right] \times 10^{-2}\}[\text{V}]. \tag{4.2}$$

The variable X_p represents the Li fraction in Li_xFePO_4, which is defined as $X_p = C_p/\rho$. Note that, in this model, we neglect coherency strain because the purpose of this work is to model the interaction between the particles – not the dynamics within a single particle. However, qualitatively similar behavior would be expected if coherency strain were included.

The electrochemical reaction rate for Li intercalation is modeled using the Butler-Volmer equation (Eq. (2.37)). The overpotential at a point on an interface is defined as $\eta = \Delta\phi - \phi_{eq}$, where $\Delta\phi = \phi_p - \phi_e$, and ϕ_{eq} is the single-particle equilibrium potential. Here, $\phi_{eq} = V_{OC} - \mu_p/F$ [45, 36, 38], with a reference value at the experimentally measured open circuit voltage plateau, $V_{OC} = 3.42$ V [29] measured with respect to a Li metal anode. The resulting lower and upper spinodal points (the local minimum and maximum of the single-particle equilibrium potential) are located at $X_p = 0.05$ and $X_p = 0.93$, respectively. The concentration range between the spinodal points is referred to as the spinodal region. In the simulations, $\Delta\phi$ corresponds to the cell voltage as both the electrostatic potential in the particles and in the electrolyte are assumed uniform and no other loss is considered. We impose the current loading by an average constant current density, $\bar{i}$, normalized by the total particle surface. Table 4.1 lists the parameters used in the simulations.

In the simulations, both particles are initially nearly fully delithiated. (For numerical stability we select an initial Li site occupancy of 2%.) The diameters of the smaller and larger particle are 40 nm and 70 nm, respectively. The two particles are immersed in an electrolyte solution within the domain of $96 \times 180 \times 96$ nm^3, which has a concentration of 1M. The particles are placed 80 nm apart, center-to-center distance, at center positions (48 nm, 50 nm, 48 nm) and (48 nm, 130 nm, 48 nm).

In this chapter, we employ a 2-nm grid spacing. The electrostatic potential difference between the electrolyte and the particles, set through the boundary conditions, is adjusted to obtain the desired current. Even though we focus on the lithiation process in this chapter, the dynamics observed during delithiation are qualitatively similar. We employ the smoothed boundary method (SBM) [2, 36] to combine the Cahn-Hilliard equation (Eq. (2.47)) with the reaction rate boundary condition (Eq. (2.37)). We assume constant, isotropic mobility for simplicity.

Symbol	Parameter	Value
T	Temperature	300 K
i_0	Exchange current density	8.5×10^{-7} A/cm^2 [38]
ρ	Interstitial site density	0.0228 mol/cm^3
D_p	Li diffusivity in the particles	5×10^{-13} cm^2/s [64, 65]
M_p	Li mobility in the particles	$D_p\rho/(RT)$
$\boldsymbol{\kappa}$	Gradient energy coefficient	varied; see text

Table 4.1: Parameters employed in the simulations in this chapter

We perform a parametric study on the interfacial energy penalty to analyze the different transformation dynamics by varying $\boldsymbol{\kappa}$. Smaller values of $\boldsymbol{\kappa}$ result in thin interfaces (between Li-rich and Li-poor phases), intermediate values result in thicker interfaces, and larger values result in suppressed intraparticle phase separation. We set $\boldsymbol{\kappa}$ to be anisotropic to obtain a preferential phase separation in one direction, as observed in $LiFePO_4$. However, the detailed dynamics of the phase separation is beyond the scope of this work, as we focus here on the interactions. While the $\boldsymbol{\kappa}$ values in in this parametric study correspond to unrealistically large interfacial thicknesses, we use them to control the phase separation behavior without affecting other conditions such as the size of particles or kinetics. (The interfacial energy per unit area, γ, of our simulations range from 9.04×10^{-6} J/cm^2 to 8.08×10^{-5} J/cm^2, while DFT calculated literature values are in the range of 7×10^{-7} J/cm^2 to 1.15×10^{-5} J/cm^2 for the different crystal orientations [66].) It should also be noted

that coherency strain may contribute to the suppression of phase separation, and therefore the large $\boldsymbol{\kappa}$ may be thought to account for such effect in an approximate manner. In an experimental study, one would instead change the particle size, as it is not possible to increase the interfacial thickness. We refer the reader to the existing literature for the dynamics of phase transformation in individual particles [43, 42, 66].

4.3 Results

4.3.1 Interparticle phase separation

We first analyze the process of interparticle phase separation, in which intraparticle phase separation is fully suppressed. For this purpose, we select the value for $\boldsymbol{\kappa}$ of $\kappa_x = 1.66 \times 10^{-10}$ J/cm (corresponding to interfacial energy per unit area, γ, of $\gamma_x = 3.6{\times}10^{-5}$ J/cm^2 [67]), and $\kappa_y = \kappa_z = 8.32{\times}10^{-10}$ J/cm ($\gamma_y = \gamma_z = 8.08{\times}10^{-5}$ J/cm^2), which suppresses phase separation in both particles. The effective interfacial thickness in this case is 44 nm, which under the kinetic conditions examined, suppresses phase separation. We examine three values of applied current (i) $\bar{i} = 6\%\ i_0$, (ii) $18\%\ i_0$, and (iii) $54\%\ i_0$ which correspond to (i) C/12.5, (ii) C/4.17 and (iii) C/1.39.

We first examine the $\bar{i} = 6\%\ i_0$ case. Snapshots of the particles' concentration evolution and their corresponding depth of discharge (DOD) during lithiation for this case are presented in Figs. 4.1 and 4.2(a), respectively. Note that the horizontal axis in Fig. 4.2(a) is the cell DOD, which is linearly related to time because of the constant current condition. Both particles are initially at a DOD of 2% (Fig. 4.1(a)). The smaller particle lithiates faster than the larger particle because of its greater surface area per volume. Shortly after the DOD of the smaller particle exceeds the lower spinodal point, the particle rapidly transitions to a nearly fully lithiated state (Fig. 4.1(b) and 4.1(c)). During the fast lithiation of the smaller particle, Li is extracted from the larger particle. After the smaller particle is nearly fully lithiated, the larger particle begins a steady lithiation (Fig. 4.1(d)), extracting a small amount of Li from

the smaller particle, until the completion of its lithiation. This lithiation process is facilitated by interparticle phase separation, during which one particle undergoes a rapid transformation to the lithiated state and extracts lithium from the other particle, resulting in a sequential transformation of the particles.

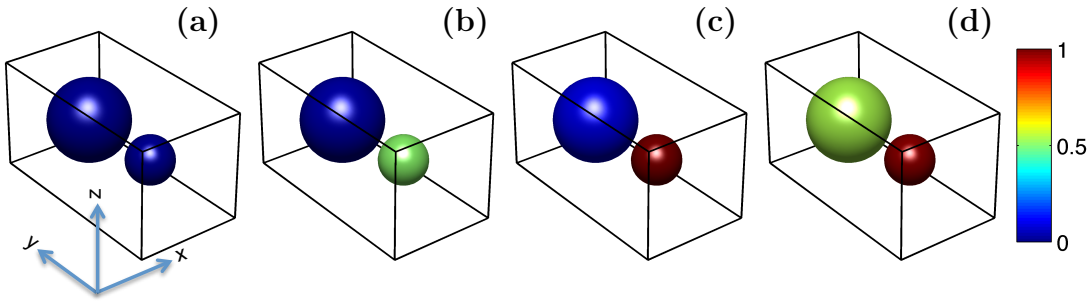

Figure 4.1: The concentration evolution during lithiation with $\bar{i} = 6\%\ i_0$ for the case where intraparticle phase separation is suppressed. Four snapshot are shown at four different times at which the DOD is equal to (a) 2% (initial configuration), (b) 4%, (c) 14%, and (d) 70%. The colors represent x in Li_xFePO_4 according to the color bar on the right, red and blue corresponding to the fully lithiated and delithiated states, respectively. The dimensions of the cell are shown in (a).

To explain the behavior of the system, we examine the voltage of the cell. The cell voltage of the process is shown in Fig. 4.2(b) curve (i) for the case of $\bar{i} = 6\%\ i_0$, along with the equilibrium potential of the particles (curves (ii) and (iii)). In Fig. 4.2, we denote three different regimes with different shades: "stable + stable" (darker blue), "unstable + stable" (gray), and "unstable + unstable" (lighter blue). These regimes indicate the combination of the state of the two particles. We define a stable particle as a particle with a concentration outside the spinodal region, and an unstable particle as one with a concentration within the spinodal region. We refer to the states in this manner because as an unstable particle lithiates, its driving force for lithiation increases and the lithiation accelerates if $\Delta\phi$ remains constant. This is not the case for a stable particle, for which the driving force decreases as it lithiates. At the beginning of the process, both particles are stable ("stable + stable" zone 1 in Fig. 4.2(b)). When the smaller particle exceeds the lower spinodal point, fast lithiation

begins because the driving force for Li intake increases due to the non-monotonic shape of the single-particle equilibrium potential ("unstable + stable" zone 2, not marked in the figure). Shortly after, the larger particle also exceeds the lower spinodal and becomes unstable ("unstable + unstable" zone 3). However, the smaller particle is more lithiated by then and has much larger driving force for lithiation than the larger particle. Thus, the smaller particle supplies all of the current. The cell voltage rises such that the larger particle has a driving force for delithiation. The Li released by the larger particle into the electrolyte is absorbed by the smaller particle, generating an interparticle flux. The larger particle delithiates until it returns to a stable state ("unstable + stable" zone 4). A large sudden increase of the voltage occurs as a response to the increasing equilibrium potential of the smaller particle with increasing Li concentration. When the smaller particle reaches the upper spinodal, both particles become stable ("stable + stable" zone 5). Thus, the voltage decreases to compensate for the decreasing equilibrium potentials with increasing Li concentrations at this stage. When the larger particle lithiates and becomes unstable ("unstable + stable" zone 6), the voltage begins to increase in response to the increasing equilibrium potential of the larger particle. In the meantime, the smaller particle remains stable and undergoes a small partial delithiation. When the larger particle reaches a nearly fully lithiated state ("stable + stable" zone 7), the smaller particle resumes lithiation. The process completes when both particles become fully lithiated.

The voltage behavior in Fig. 4.2(b) can be explained as follows. The results show a sudden increase or decrease in the voltage when one of the particles enters or exits the spinodal region and thus changes from a stable to an unstable state or vice versa. When both particles are stable or both are unstable, the cell voltage is determined by the combination of the driving forces for the insertion on both particles. Conversely, when one particle is stable and the other is unstable, the voltage is set

approximately by the driving force required to apply current to the unstable particle. The overpotential required for the cell lithiation at the given current is primarily provided by the difference between the cell voltage and the equilibrium potential of the unstable particle because $|\eta_{\text{unstable particle}}| >> |\eta_{\text{stable particle}}|$. For the stable particle, which can be either nearly fully lithiated or delithiated, its concentration evolves only by a small amount to maintain its equilibrium at the cell voltage. Thus, it tends to have an equilibrium potential nearly equal to the applied voltage. The steep slope of the voltage outside the spinodal region allows the stable particle to remain near equilibrium with the unstable one through small changes in its DOD. The above description can be clearly observed from the overlap between the cell and the larger particle voltage curves in the "unstable + stable" zones in Fig. 4.2(b).

We present two schematics to illustrate the interparticle phase separation. For this purpose we first define the "inverted potential range." The inverted potential range is the voltage range between the local minimum and the local maximum of the single-particle equilibrium potential, as plotted in Fig. 4.3. Lithium redistribution can only occur when the potential difference between the particle and the electrolyte, $\Delta\phi = \phi_p - \phi_e$, is in the inverted potential range, such that one particle has a positive overpotential while the other has a negative overpotential. Figure 4.3(a) schematizes a scenario in which this criterion is met, leading to the interparticle phase separation. In contrast, Fig. 4.3(b) schematizes the scenario where $\Delta\phi$ is not in the inverted potential range and both particles have a driving force for lithiation. As noted earlier, $\Delta\phi$ is equal to the cell voltage because the electrostatic potentials of the particles and electrolyte are assumed to be uniform. At the rate of $\bar{i} = 6\%\ i_0$, the cell voltage enters the inverted potential range at nearly the lower spinodal point; see Fig. 4.2(b) curve (i). In this case, the difference between the applied voltage and the single particle equilibrium potential is small. Thus, the difference in Li concentration between the spinodal point and the onset of the interparticle phase separation (i.e., when the

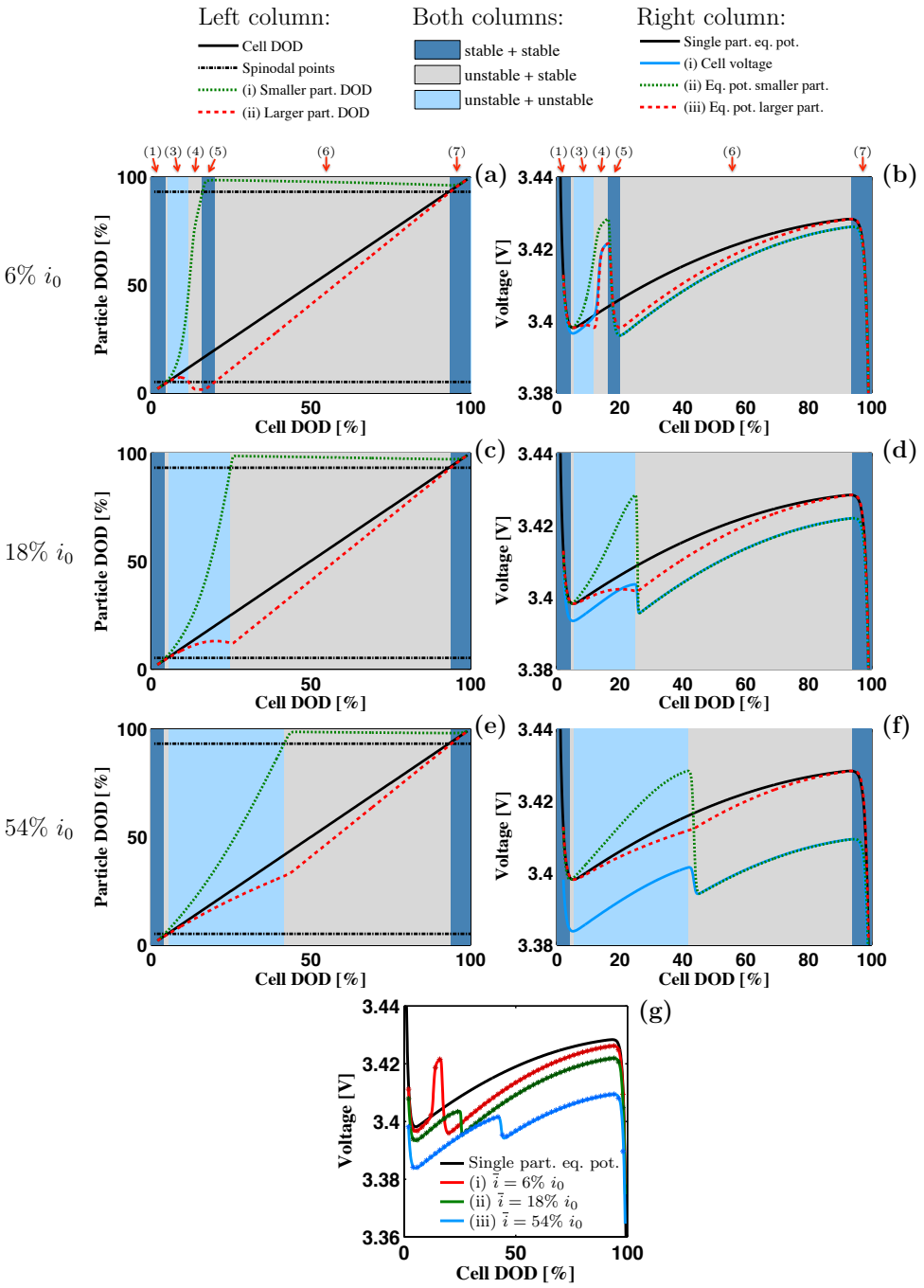

Figure 4.2: Particle concentration evolution and cell voltage when intraparticle phase separation is prevented for (a) & (b) $\bar{i} = 6\%\ i_0$, (c) & (d) $\bar{i} = 18\%\ i_0$, and (e) & (f) $\bar{i} = 54\%\ i_0$. Legends for the curves are noted in subfigure (a) for (a), (c) and (e) and in subfigure (b) for (b), (d) and (f). Color shades are denoted in subfigure (a) for (a)-(f) and indicate the states of the particles: "stable + stable" (darker blue), "unstable + stable" (gray), and "unstable + unstable" (lighter blue). (g) Voltage evolution for the three current conditions simulated, each plotted for two different governing equations for concentration evolution: the Cahn-Hilliard equation (solid) and Fick's Law of diffusion (with markers). This verifies that two dynamics yield nearly identical results.

larger particle begins partial delithiation) is also small. The difference between these two concentrations has been referred as the "concentration overshoot" and analyzed extensively in Chapter II.

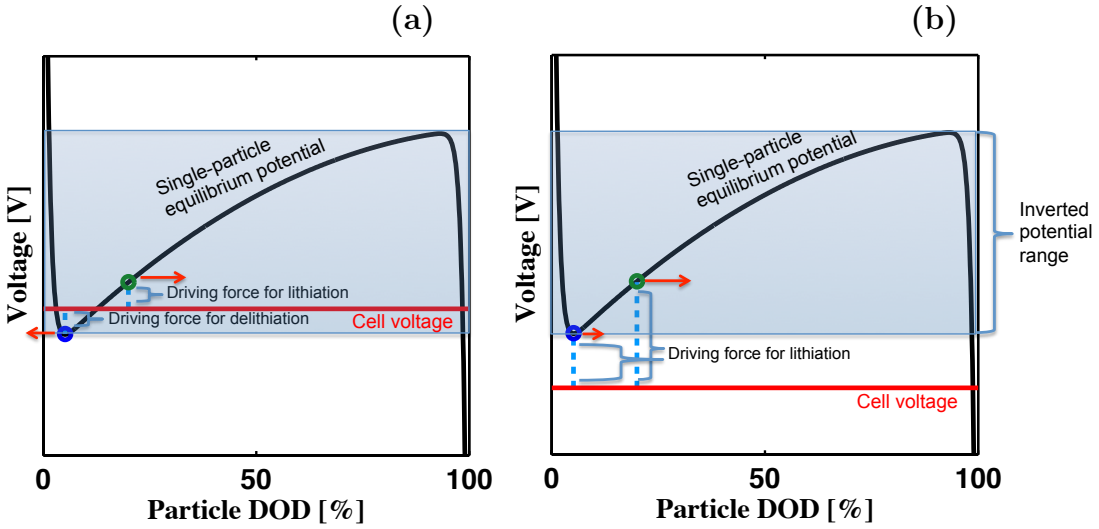

Figure 4.3: A schematic representing the criteria for interparticle phase separation. (a) When the cell voltage falls inside the inverted potential range, one particle can have a driving force to lithiate (marked with a green circle) while the other particle can have a driving force to delithiate (marked with a blue circle), as illustrated in this figure. (b) When the cell voltage falls below the inverted potential range, both particles have a driving force to lithiate.

We examine the particle interactions in response to the magnitude of the applied current by imposing two additional different rates: (ii) $\bar{i} = 18\%\ i_0$ and (iii) $\bar{i} = 54\%\ i_0$ in addition to (i) $\bar{i} = 6\%\ i_0$ studied above. Figure 4.2(c) shows the DOD of the particles for case (ii). At this rate, the larger overpotential increases the DOD at which the voltage enters the inverted potential range (Fig. 4.2(d) curve (i)) and consequently increases the concentration overshoot. When the smaller particle begins fast lithiation, the larger particle has undergone substantial lithiation. Thus, the larger particle cannot release enough lithium to return to a stable concentration and remains unstable. Unlike case (i), the equilibrium potential of the larger particle does not follow the applied voltage during the fast lithiation of the smaller particle because the larger particle remains unstable during this process ("unstable + unstable" zone

in Fig. 4.2(d)). Consequently, a large, sudden change (increase or decrease) of the voltage does not occur, and both particles transform simultaneously. Instead, only a small voltage drop is observed, reflecting that the smaller particle becomes stable (beginning of "unstable + stable" zone, DOD ∼25%). Figures 4.2(e) and 4.2(f) show the DOD and cell voltage for case (iii), where the larger particle does not undergo any partial delithiation during the process. In this case, the overpotential is sufficiently large that the cell voltage barely enters the inverted potential range prior to the lithiation of the smaller particle, thus preventing the interparticle phase separation (Fig. 4.2(f) curve (i)). At these two rates, it can be considered that the particles undergo a simultaneous transformation. As rate increases, the lithiation is more dominated by the case schematized in Fig. 4.3(b) as opposed to the case in Fig. 4.3(a).

We now provide a validation demonstrating that Fick's diffusion can be a good approximation for scenarios in which intraparticle phase separation is suppressed. In Chapters III and V, where much larger computational domains are employed, Fick's diffusion is used to approximate the Cahn-Hilliard equation with large $\boldsymbol{\kappa}$. We performed this approximation because larger stable time steps can be used when solving for Fick's diffusion, reducing the computational costs. Here, we compare the results when the Cahn-Hilliard equation (Eq. (2.47)) is replaced with Fick's diffusion equation (Eq. (2.5) or Eq. (2.46) in its SBM form), which is computationally more efficient. Figure 4.2(g) compares the voltages calculated with the Fick's approximation and the Cahn-Hilliard equation. The markers in Fig. 4.2(g) indicate the results of the simulations using Fick's diffusion, while the solid curves indicate the Cahn-Hilliard simulation results. The two results show excellent agreement. For the given $\boldsymbol{\kappa}$ the maximum difference is 0.5%. We do not include the resulting particle DODs because the curves overlap each other.

4.3.2 Intraparticle phase separation

We now analyze the dynamics in which the particles undergo intraparticle phase separation. For this purpose, $\boldsymbol{\kappa}$ is set to be $\kappa_x = 1.04 \times 10^{-11}$ J/cm ($\gamma_x = 9.04 \times 10^{-6}$ J/cm^2) and $\kappa_y = \kappa_z = 5.20 \times 10^{-11}$ J/cm ($\gamma_y = \gamma_z = 2.02 \times 10^{-5}$ J/cm^2). These parameters result in a phase separation in the y-z plane with a thickness of 11 nm.

We first describe the concentration evolution of the particles at $\bar{i} = 6\%\ i_0$, shown in Fig. 4.4. Some locations of the smaller particle reach the lower spinodal point before any region of the larger particle because of its larger area per volume. At this time, the smaller particle undergoes intraparticle phase separation; see Fig. 4.4(a). During the two-phase lithiation of the smaller particle, the larger particle is partially delithiated and then remains inactive in a Li-poor phase. The partial delithiation of the larger particle indicates the presence of an interparticle flux. The Li-rich phase in the smaller particle then grows until the particle is nearly fully lithiated; see Fig. 4.4(b). Afterwards, the larger particle re-lithiates via a two-phase lithiation process; see Fig. 4.4(c). The Li-rich phase grows in the larger particle until it becomes fully lithiated. This behavior is consistent with the domino-cascade model described in Ref. [13].

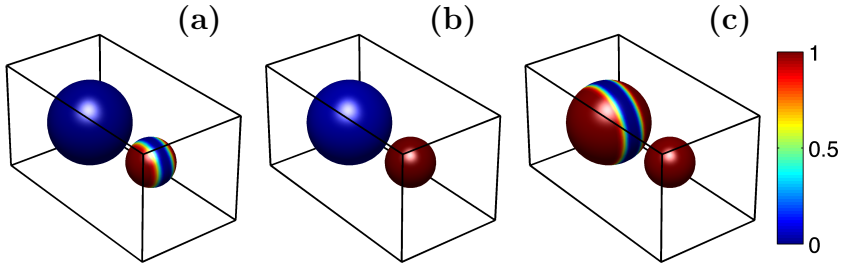

Figure 4.4: The concentration evolution during lithiation with $\bar{i} = 6\%\ i_0$ for the case in which intraparticle phase separation occurs in both particles. Three snapshots are shown at three different times at which the DOD is equal to (a) 10%, (b) 20%, and (c) 70%. The colors represent x in Li_xFePO_4 according to the color bar on the right, red and blue corresponding to the fully lithiated and delithiated states, respectively.

As previously described, the two particles exhibit a sequential lithiation. We refer

to the cell voltage to explain the process in detail. Curve (i) in Figs. 4.5(a) and 4.5(b) shows the DOD of the larger and the smaller particle, respectively, and curve (i) in Fig. 4.5(c) shows the voltage response. When the local concentration of the smaller particle reaches the spinodal point, nucleation of the Li-rich phase occurs and the voltage increases (point (1) in Fig. 4.5(c) inset). During the lithiation of the smaller particle, the voltage remains at a value higher than the value corresponding to the lower spinodal (the local minimum in the equilibrium potential), preventing nucleation in the larger particle. (Figure 4.6 schematizes the lithiation via a two-phase process.) The voltage further increases when the two Li-rich domains in the smaller particles start to contact each other (between Fig. 4.4(a) and 4.4(b) and point (2) in Fig. 4.5(c) inset). During the merging of the two Li-rich domains and after the smaller particle becomes monophasic, the voltage response of the cell is similar to that of a solid solution. A voltage drop follows when the smaller particle reaches the upper spinodal. At this point, the larger particle undergoes intraparticle phase separation, resulting in a flat voltage during the growth of the two Li-rich domains and in a voltage increase when the Li-rich domains contact each other.

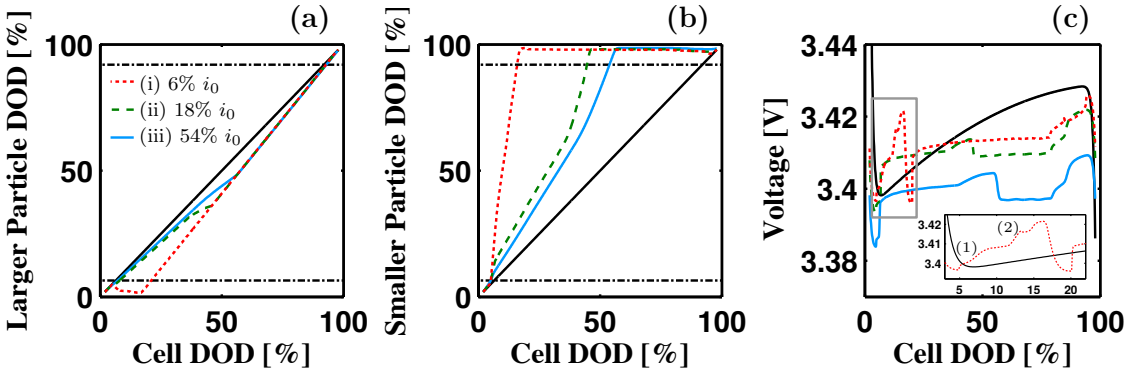

Figure 4.5: Concentration evolution and cell voltage at different currents for the case of intraparticle phase separation in both particles. (a) & (b) DOD of the larger particle and the smaller particle, respectively. (c) Cell voltage; the beginning of curve (i) is magnified in the inset. Three rates are shown: (i) $\bar{i} = 6\%\ i_0$ (red dotted curve), (ii) $\bar{i} = 18\%\ i_0$ (green dashed curve), and (iii) $\bar{i} = 54\%\ i_0$ (blue solid curve).

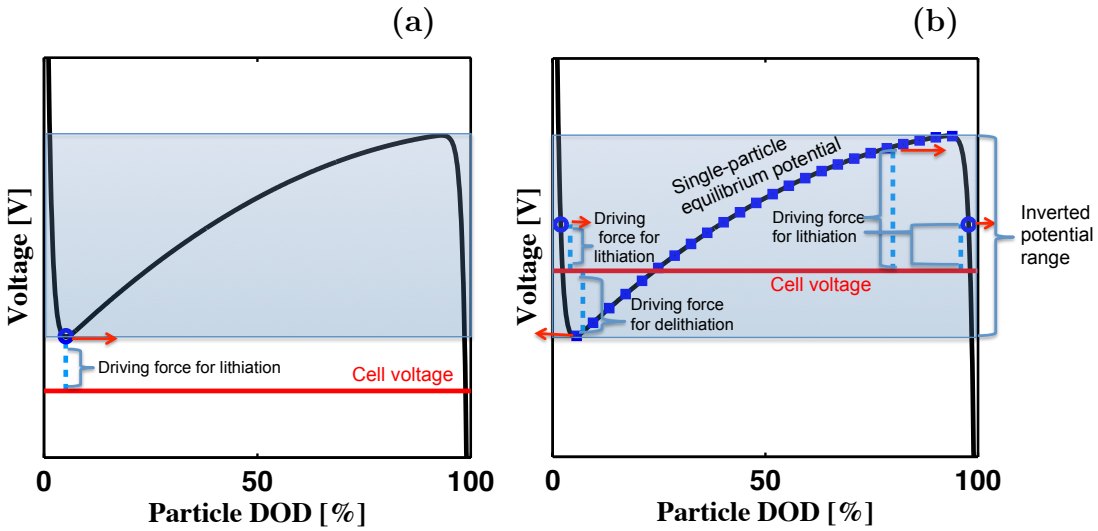

Figure 4.6: A schematic representing the criteria for intraparticle phase separation. (a) In order for a Li-rich phase to be nucleated, a voltage value lower than the lower spinodal point is required. (b) Once a particle is phase separated, the cell voltage can fall inside the inverted potential range and maintain its overall driving force for lithiation. The circles denote the state of a phase in terms of the DOD and the equilibrium potential. The squares denote the equilibrium potential for composition over the interface (without accounting for the energy penalty term).

As in the last section, we also simulate the lithiation processes at higher currents, (ii) $\bar{i} = 18\%\ i_0$ and (iii) $\bar{i} = 54\%\ i_0$. The DOD of the particles and the voltage are shown in Fig. 4.5. At these two C-rates, we observe that nucleation of the Li-rich phases in both particles occurs almost simultaneously. The larger overpotentials resulting from the higher C-rates and the faster dynamics of the lithiation processes causes the larger particle to phase separate before a voltage increase due to the phase separation in the smaller particle prevents it. Thus, the two particles lithiate simultaneously, as can be inferred from the monotonic increase of particle DOD vs. the cell DOD in Fig. 4.5(a) and (b). In both case (ii) and (iii), the smaller particle completes lithiation at an approximate cell DOD of 50% because of its larger area per unit volume compared to that of the larger particle. We observe that the voltage increases when the Li-rich domains in the smaller particle come into contact with each other; thus, the smaller particle transitions from a two-phase state to a single-phase state.

The larger particle continues reacting until it becomes nearly fully lithiated, similarly causing a voltage increase at the end of its lithiation when the Li-rich domains contact each other. Both curves (ii) and (iii) in Fig. 4.5(c) exhibit two voltage plateaus. The first plateau is determined by the intraparticle coexistence of the Li-rich and Li-poor phases in the two particles [5]. The second plateau is an indication of the coexistence of the two-phase larger particle and the single-phase smaller particle. The slight positive slope can be attributed to the increase in the reactive interfacial area as a result of the growth of the Li-rich phase (for the assumed geometry), which a requires a reduction in the overpotential to maintain a constant current.

We conclude that the general dynamics of the two-phase lithiation described here is similar to the case in which intraparticle phase separation is suppressed. Figure 4.7, overplots the results from Fig. 4.2 and Fig. 4.5 for $\bar{i} = 6\%\ i_0$ and $\bar{i} = 54\%\ i_0$. At low C-rates, particles transform sequentially, whereas the sequential transformation is suppressed at high C-rates. However, there are some differences between the two cases. The most distinguishable difference is that, in the intraparticle phase-separation case, the cell voltage is flat instead of being curved (Fig. 4.7(c)), which is expected for a two-phase growth during the lithiation of the individual particles [5]. Even though both cases have a simultaneous lithiation of the two particles at $\bar{i} = 54\%\ i_0$, the intraparticle phase separation yields more uniform reaction over the two particles, resulting in faster (slower) lithiation of the larger (smaller) particle in comparison to the interparticle phase-separation case (Fig. 4.7(b)). This is because, during the simultaneous two-phase lithiation process, (1) the two particles are closer to being in equilibrium with each other and (2) the particles follow a lower free energy path (accessible due to the lower interfacial penalty of this case). Consequently, the particles experience a more similar driving force for lithiation compared to that experienced by monophasic particles with different DODs. For this same reason, because the particles can attain equilibrium easily the interparticle flux observed here

is smaller. However, these differences do not result in qualitative differences in the overall dynamics.

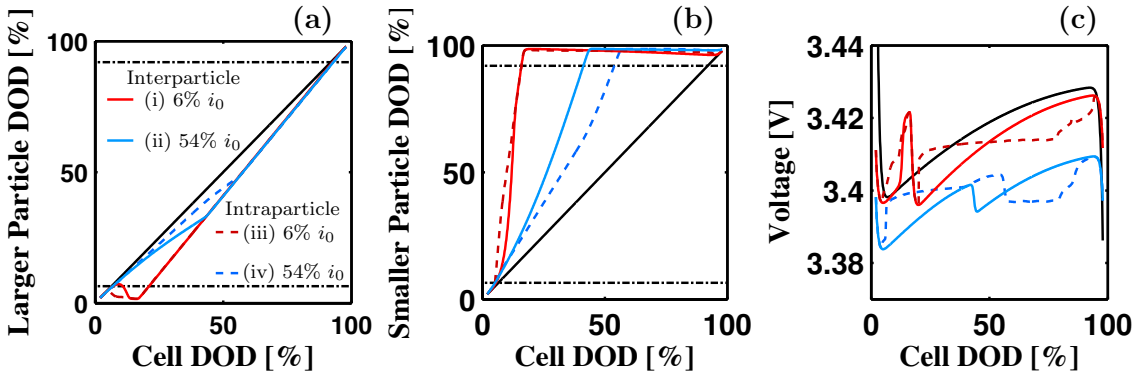

Figure 4.7: Concentration evolution and cell voltage at different currents comparing the interparticle phase separation (solid curves) and the intraparticle phase separation (dashed curves) cases at $\bar{i} = 6\%\ i_0$ (red curves) and $\bar{i} = 54\%\ i_0$ (blue curves). (a) & (b) DOD of the larger particle and the smaller particle, respectively. (c) Cell voltage.

4.3.3 Combined intraparticle and interparticle phase separation

We explore the last case in this study, where the cell contains one particle with intraparticle phase separation and the other with intraparticle phase separation suppressed. The values of $\kappa_x = 4.16 \times 10^{-11}$ J/cm ($\gamma_x = 1.81 \times 10^{-5}$ J/cm^2), $\kappa_y = \kappa_z = 2.08 \times 10^{-10}$ J/cm ($\gamma_y = \gamma_z = 4.04 \times 10^{-5}$ J/cm^2), are used for this case. This set of values effectively suppresses intraparticle phase separation in the smaller particle but not in the larger particle. The thickness of the interface is 22 nm in the y-z plane.

The concentration evolution for this case at $\bar{i} = 6\%\ i_0$ is shown in Fig. 4.8. As in the other two cases, the smaller particle lithiates faster than the larger one initially due to its larger area per volume. As described in the interparticle phase separation case discussed earlier, there is a concentration overshoot before the interparticle phase separation can occur (i.e., a difference between the spinodal point and the onset of the interparticle phase separation). However, in this case, before the smaller particle

can begin interparticle phase separation, the larger particle undergoes intraparticle phase separation, as intraparticle phase separation can occur as soon as some regions of the larger particle reach the spinodal point; see Fig. 4.8(a). The smaller particle partially delithiates when the larger particle nucleates the-Li rich phase and remains delithiated during the lithiation of the larger particle. The larger particle continues its two-phase lithiation process until it is nearly fully lithiated; see Fig. 4.8(b). After it reaches a concentration above the upper spinodal point, the smaller particle lithiates via a solid solution; see Fig. 4.8(c).

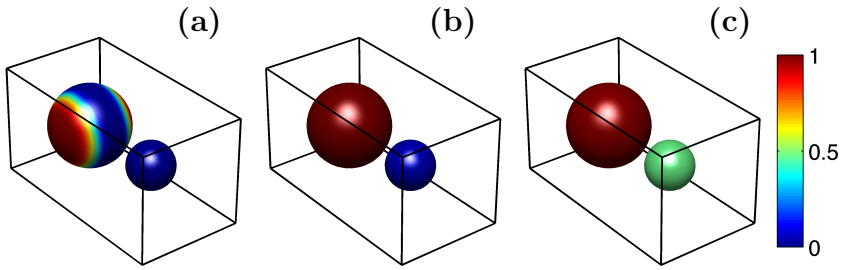

Figure 4.8: The concentration evolution during lithiation with $\bar{i} = 6\%\ i_0$ for the case in which intraparticle phase separation is suppressed in the smaller particle. Three snapshots are shown at three different times at which the DOD is equal to (a) 30%, (b) 84%, and (c) 90%. The colors represent x in Li_xFePO_4 according to the color bar on the right, red and blue corresponding to the fully lithiated and delithiated states, respectively.

We now describe the voltage response. Figure 4.9 shows the DOD of the two particles (curve (i) in Fig. 4.9(a) and 4.9(b)) and the voltage of the cell (curve (i) in Fig. 4.9(c)). The voltage response of the cell differs significantly from those in the last sections (curves (i) in Figs. 4.2(g) and 4.5(c)), which can be understood as the consequence of the inverted order of reaction of the particles; i.e., the larger particle reacts first. A flat voltage plateau in the cell DOD between ∼15% and ∼50% represents the two-phase lithiation of the larger particle. Then, an increase in the voltage is observed as a response to the merging of the two Li-rich domains in the larger particle. This increase in the voltage lasts for a larger fraction of the cell DOD because the interfaces contact each other earlier as a consequence of the thicker

interface (caused by the larger value of κ_x in this case). After the concentration in the larger particle reaches the upper spinodal, the voltage decreases, allowing the smaller particle to lithiate. The voltage increases around a DOD of ∼85% without a plateau as a response to the monophasic lithiation of the smaller particle. The latter part of curve (i) in Fig. 4.9(c) resembles the earlier part of curve (i) in Fig. 4.2(g), and the earlier part of curve (i) in Fig. 4.9(c) is reminiscent of the latter part of Fig. 4.5(c) curve(i).

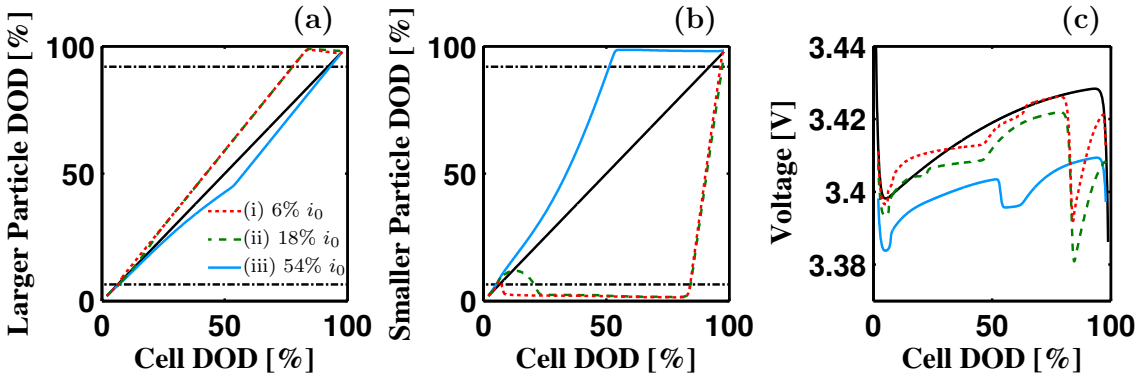

Figure 4.9: Concentration evolution and cell voltage at different currents for the case of intraparticle phase separation only in the larger particle. (a) & (b) DOD of the larger particle and the smaller particle, respectively. (c) Cell voltage. Three rates are shown: (i) $\bar{i} = 6\%\ i_0$ (red dotted curve), (ii) $\bar{i} = 18\%\ i_0$ (green dashed curve), and (iii) $\bar{i} = 54\%\ i_0$ (blue solid curve).

As in the last sections, we also analyze the lithiation processes at (ii) $\bar{i} = 18\%\ i_0$ and (iii) $\bar{i} = 54\%\ i_0$ (Fig. 4.9). At the current of $\bar{i} = 18\%\ i_0$, the sequential transformation of the particles (the larger one followed by the smaller one) still prevails. As can be seen in curve (ii) in Fig. 4.9(b), a larger partial delithiation of the smaller particle (and thus a larger interparticle flux) is observed than at $\bar{i} = 6\%\ i_0$ (case (i)). The voltage response for this case is very similar to that for case (i), but with a larger overpotential. At a current of $\bar{i} = 54\%\ i_0$ (case (iii)), simultaneous lithiation occurs. As in the other higher-rate cases, the smaller particle lithiates faster than the larger particle due to its larger surface area per volume. In this case, the voltage response

is similar to curve (i) in Fig. 4.2(f), with the exception that a small voltage plateau appears (from ∼50% to ∼60% in the cell DOD), corresponding to the two-phase state of the larger particle after the small particle reaches the upper spinodal.

4.4 Discussion

As previously mentioned, whether nanoparticulate phase-separating materials (such as $LiFePO_4$) react through interparticle phase separation, intraparticle phase separation, or a combination of both remains a topic of debate. We have here shown that all of these three cases give rise to particle interactions via Li redistribution at sufficiently low currents. The dynamics resulting from the three cases are qualitatively similar. Specifically, (1) one particle can delithiate as the other particle undergoes rapid lithiation, (2) this leads to interparticle flux, and (3) the voltage can suddenly change to maintain constant current. However, there are two main differences between them. The first difference is the voltage of the cell, and the second is the order of reaction of the particles. As previously known [5], the intraparticle phase separation is marked with plateaus in the voltage curve, while the interparticle phase separation is accompanied by a continuous increase in the voltage followed by a rapid increase. The order in which the particles react can vary depending on the phase-transformation path: if all particles in a cell can internally phase separate, or instead cannot phase separate and remain monophasic, the smaller particle would lithiate first. However, in a cell with some particles that phase separate internally and others that remain monophasic, this order may be reversed.

These differences are important because they can be exploited to identify the actual phase-transformation path occurring in a physical system. While the voltage responses are distinct for the three cases in a two-particle configuration (or other configurations with few particles), such fluctuations are averaged out in a cell with many particles. Therefore, it is not possible to differentiate the phase-transformation

path based on the voltage. However, the order in which particles react may provide a tool for differentiating the mixed case, i.e., that contains both (presumably smaller) particles that do not phase separate within themselves as well as (presumably larger) particles that can internally phase separate. Experiments can be designed to examine the lithiation behavior of systems containing particles with various distributions of sizes at low currents. If larger particles lithiate before nearby smaller particles, it is an indication that the system is a mixture of particles that phase transform via intraparticle phase separation and those that phase transform via interparticle phase separation. The particle size at which this transition occurs may indicate the critical particle size at which the phase-transformation path changes. However, it is important to note that a small monophasic particle might still react before a large phase-separating particle if their sizes are significantly different.

The presence of both interparticle and intraparticle phase separation (along with interparticle connectivity [38]) may help explain the lack of an obvious order of reaction of the particles observed in the experiments of Chueh et al. [11]. However, as will be discussed in Chapter V, for a strong particle-size dependence to prevail, adequate ionic and electronic connectivities through the electrolyte and electron-conducting phase, respectively, are required. Additionally, direct contact between particles should be avoided as they would provide an alternative, non-electrochemical transport path for Li. These conditions are not usually met in working cells. Therefore, the cells used in experiments that aim to identify the critical particle size must be constructed carefully to yield these conditions.

The work in this chapter demonstrates that the qualitative results observed in our previous studies on the dynamics of many-particle systems [38, 36], which assume that particles remain monophasic, apply to cases where all particles undergo intraparticle phase separation. However, it also shows that the dynamics would change quantitatively and qualitatively when the system contains both two-phase and monophasic

particles.

4.5 Conclusion

We explored phase-separation kinetics in a cell containing two nanoparticles that exhibit a tendency to phase separate. In particles that do not undergo intraparticle phase separation, we have identified the relationship between cell voltage and the concentration of both particles. A particle with a concentration within the spinodal region (i.e., an "unstable" particle) has a stronger effect on the voltage than a particle outside the spinodal region (i.e., a "stable" particle). In the three scenarios studied in this chapter, a sequential lithiation was observed at low currents, whereas a simultaneous transformation was observed at higher currents. In cells containing only particles that phase separate or only particles that remain monophasic, the smaller particles react first during a sequential transformation process. However, the order in which the particles phase transform can be reversed in cells containing one particle that phase separates and another that remains monophasic. In such a case, which could arise if the smaller particle is sufficiently small to prevent phase-boundary formation within it while the larger particle is large enough to nucleate a second phase, the larger particle tends to transform before the smaller particle during a sequential transformation. When sequential lithiation occurs through either intraparticle or interparticle phase-separation mechanisms, a partial delithiation accompanied by interparticle flux emerges. Interparticle fluxes will result in internal resistive losses, higher local currents, and additional particle expansion-contraction cycles [38], which are undesirable for battery applications.

CHAPTER V

THE CONNECTIVITY DEPENDENCE OF PARTICLE INTERACTIONS

5.1 Introduction

In this chapter we demonstrate the impact of cell architecture (in terms of ionic and electronic connectivities between active particles) and cycling rate on the multi-particle (de)lithiation kinetics. Specifically, the connectivity between particles is shown to have a strong effect on the interparticle phase separation. We show that interparticle phase separation can be reduced or eliminated by improving ("homogenizing") the connectivity between particles.

With an eye toward both understanding the dominant mechanisms that contribute to inhomogeneous charging/discharging at the electrode scale and identifying practical methods to address them, we develop a model that describes Li redistribution between particles during the charge/discharge process in two different electrode architectures. These two architectures correspond to nanoparticle agglomerates (often observed in nanoparticulate electrodes [68, 21, 69]) of different densities: a dilute agglomerate and a dense agglomerate. These two constructions are illustrated in Fig. 5.1(a). The first architecture (Fig. 5.1(a)(i)) consists of active particles coated and "wired" with electronically and ionically conducting material, providing excellent electrical connectivity to the current collector and ionic connectivity to the electrolyte. Furthermore, the coating prevents any direct contact among active particles. This architecture is hereafter referred to as the configuration with "homogeneous connec-

tivity." In the second architecture (Fig. 5.1(a)(ii)), no or partial coating/wiring leads to direct contacts of active particles in clusters, which provides an additional path for Li transport. In addition, electrical and ionic connectivities are reduced and the electrostatic potential of the particles may become inhomogeneous (the consequence of which is not considered here as discussed later). This architecture is referred to as the configuration with "heterogeneous connectivity." Similar to the work of Kang and Ceder [70], the nanoparticles considered here have an average size (diameter) of ∼50 nm. We choose simulation parameters specific to simulate charging/discharging a network of different-size $LiFePO_4$ (LFP) nanoparticles, a commercial cathode material known for both its high-rate performance [9, 70, 71] and its thermodynamic tendency to phase separate [72, 73].

To elucidate the contribution associated with the connectivity of the particles, we consider two separate cell architectures. First, we investigate a dilute configuration with homogeneous connectivity. This corresponds to an idealized electrode configuration where the particles are completely separated from each other by embedded electronic conductors. In this case, Li can only be redistributed via a reaction by which the resulting ionic Li and electrons are transported through the electrolyte and the electronic conductors, respectively. As it will be shown later, in this ideal case, the lithiation/delithiation processes of individual particles are nearly independent of their position with respect to other particles, as well as the separator and current collector. This is because the electrolyte concentration is nearly constant throughout the small domain considered here (∼300 nm in length) due to the fast Li-ion transport in the electrolyte and the relative high porosity of the two cell constructions. Figure 5.1(a)(i) shows a schematic representation of this architecture and Fig. 5.1(b) a transmission electron microscopy (TEM) image of well-spaced particles. Second, we analyze a configuration with heterogeneous connectivity, a more realistic electrode configuration representative of a dense agglomerate of particles. In hetero-

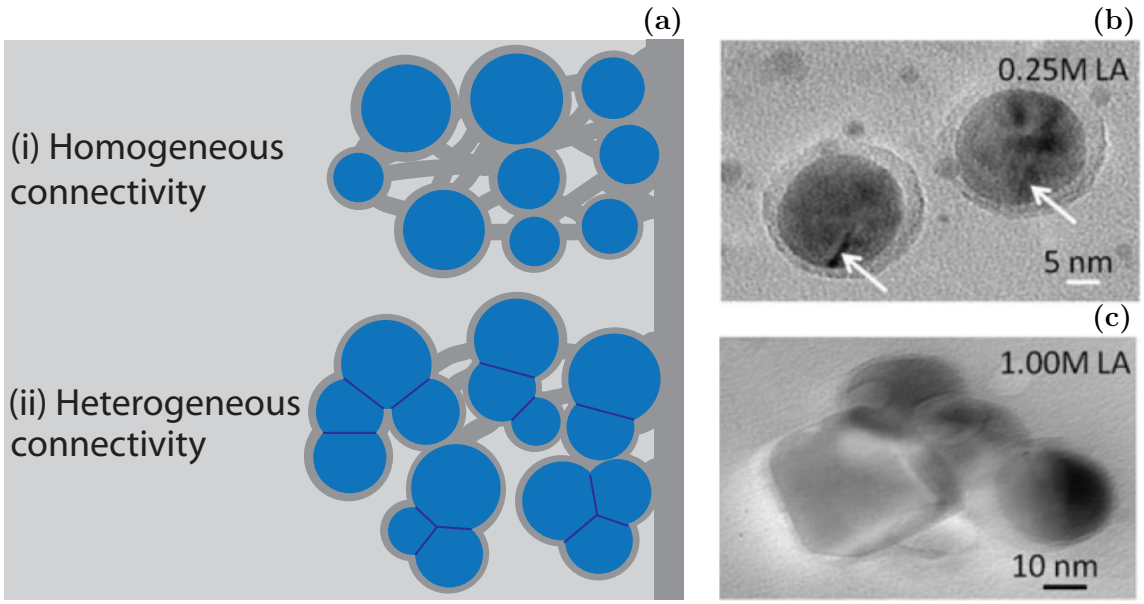

Figure 5.1: (a) Schematics of two different possible Li redistribution mechanisms: (i) In the case with homogeneous connectivity, Li is transported through the electrolyte (and electrons through conductive carbon black or carbon-coating) to be redistributed from one particle to another. (ii) In the case with heterogeneous connectivity, Li can be directly transported between abutting particles. The electrostatic potential of the particles may become inhomogeneous due to poor electronic connectivity, which is not considered here. (b) Transmission electron microscopy (TEM) image of a sample where the particles are perfectly coated and not in direct contact between each other, corresponding to case (i). (c) TEM image of particles in possible direct contact between each other corresponding to case (ii). Figures (b) and (c) obtained from Ref. [3].

geneously connected particles, there is a spatial preference in the order of reaction of the particles caused by the direct contact between particles and electrostatic potential inhomogeneities. Here, we model the heterogeneous connectivity solely by the direct transport between particles. Explicitly tracking the electronic conductors network and solving for the electrostatic potential of the conductors and particles is beyond the scope of this work. However, it is important to note that inhomogeneities in the voltage would lead to more inhomogeneity in the lithiation of the particles than what we report here. Figure 5.1(a)(ii) shows a schematic representation of the configuration with heterogeneous connectivity and Fig. 5.1(c) a TEM image of heterogeneously connected particles. The direct contact between the particles facilitates a redistribution

of Li via the contact area, driven simply by a transport process (dependent on the chemical potential difference between the contacting particles) through a permeable boundary. In this configuration the dynamics is "local-environment dependent" because contacting particles are strongly coupled through direct transport rather than the weaker electrochemical interactions. The direct transport can be physically interpreted as a "shortcut" path because it allows Li to move from one particle to another without an electrochemical reaction.

Direct Li transport between LFP particles has not been studied before in the literature as a mechanism for Li redistribution. However, there is substantial evidence for its existence via analyzing the ionic conductivity of electrode constructions of bare pristine LFP (without electrolyte nor additives). For example, in the work of Wang and Hong [74], the ionic conductivity of a pristine LFP cathode was measured to be in the range of 10^{-5} S/cm (equivalent to an ionic diffusivity of 10^{-10} cm^2/s). In such constructions, the Li transport in the cathode is limited to the direct Li transport between the particles, as there is no driving force for electrochemical reactions.

5.2 Model

To include direct transport between particles, we add a boundary condition to the original formulation of Li transport in the particles and, consequently, modify the smoothed boundary method (SBM) form of the equations.

5.2.1 Original formulation

To describe the physics that govern an electrochemical cell, we employ the four coupled equations introduced in Chapter II: concentration evolution in the (1) cathode particles and (2) electrolyte, (3) current continuity in the electrolyte, and (4) the reaction at the electrode-electrolyte interface.

The concentration evolution in the cathode particles is described using Fickian

diffusion to approximate non-equilibrium solid-solution Li diffusion (Eq. (2.5)) with a reaction boundary condition at the particle-electrolyte interface (Eq. (2.6)). In addition, at the particle-particle boundary A_p, present only in the dense agglomerate, we add a boundary condition to account for direct Li transport,

$$\vec{n}_p^{i,j} \cdot \mathbf{J} = \frac{\rho}{RT} P(\mu_{p,j} - \mu_{p,i}) \in A_p, \tag{5.1}$$

where $\vec{n}_p^{i,j}$ is the unit normal vector from particle j to particle i at the contact interface, P is the permeability of the interface, and $\mu_{p,i}$ and $\mu_{p,j}$ are the chemical potentials of the two particles in contact. Periodic boundary conditions are assumed for the box boundaries. The governing equations and boundary conditions for the concentration (Eqs. (2.8a) and (2.8b)) and electrostatic potential (Eqs. (2.18) - (2.20)) of the electrolyte are the same as those introduced previously.

The Butler-Volmer equation (Eq. (2.37)) is used to model the reaction rate r_{Li}. For simplicity, here, we assume that i_0 is independent of the cathode concentration,

$$i_0 = i_0' \sqrt{\frac{C_e}{C_e^0}}, \tag{5.2}$$

where i_0' is the experimentally measured exchange current density and C_e^0 is the concentration at which i_0' is experimentally measured. The chemical potential, μ_p, is obtained from a first principles calculation [19]. The polynomial used to define the chemical potential is

$$\begin{aligned} -\mu_p/F = -\mu_b/F = \\ \{\left[5(1.05 - 2.1X_p)^{51} - 2.925275X_p^2 + 6.375071X_p - 2.558325\right] \times 10^{-2}\}[\mathrm{V}], \end{aligned} \tag{5.3}$$

where X_p corresponds to the site fraction of Li in $\mathrm{Li}_x\mathrm{FePO}_4$.

Due to the small size of the electrochemical cells considered herein, the electrostatic potential and concentration gradients of the electrolyte are small; therefore, we do not describe those results. For the same reason, we express the observed dynamics

in terms of the applied voltage of the cell instead of the local potential difference across the interface ($\Delta\phi$) because these two values are fairly similar.

5.2.2 Smoothed boundary method

We modify the SBM to define the particles using more than one domain parameter, which is required to consider direct transport between particles in the dense agglomerate because a domain parameter interface between contacting particles is necessary. We refer to the different "i" domains as ψ_i and to the sum of all domains as ψ_T. In the dilute electrode with no direct transport between particles, the 65 particles are defined using one parameter, $\psi_{i=1} = \psi_T$. Alternatively, for the dense agglomerate, the 200 particles are described by five domain parameters such that the neighboring particles are defined by distinct domain parameters.

The SBM formulation of our governing equations is given below. For the dilute agglomerate, only one concentration variable, $C_{p,i=1}$, is used to represent the Li concentration in the particles because the particles only include one domain in this case. For the dense agglomerate, five concentration variables, $C_{p,i}$, are evolved with their corresponding domain parameters, according to

$$\frac{\partial C_{p,i}}{\partial t} = \frac{D_p}{\psi_i}[\nabla \cdot \psi_i \nabla C_p] + W_{r,i}\frac{|\nabla\psi_i|}{\psi_i} r_{Li,i} + \sum_{j\neq i} W_{p,i}\frac{|\nabla\psi_i|}{\psi_i}\frac{\rho}{RT}P(\mu_{p,j} - \mu_{p,i}), \quad (5.4)$$

which combines Eq. (2.5) with the two boundary conditions for the reaction (Eq. (2.6)) and interparticle flux (Eq. (5.1)). Here, $r_{Li,i}$ is the reaction rate for particle i, and $W_{r,i}$ and $W_{p,i}$ are the reaction and interparticle flux weighting factors, respectively, [2], which are defined as

$$W_{r,i} = \left(\frac{|\nabla\psi_i||\nabla\psi_T|}{\sum_{j=1}^{N_{dom}}\sum_{k=j+1}^{N_{dom}}|\nabla\psi_j||\nabla\psi_k| + \sum_{j=1}^{n}|\nabla\psi_j||\nabla\psi_T|}\right)^{\beta}, \quad (5.5)$$

$$W_{p,i} = \left(\frac{\sum_{j\neq i}|\nabla\psi_i||\nabla\psi_j|}{\sum_{j=1}^{N_{dom}}\sum_{k=j+1}^{N_{dom}}|\nabla\psi_j||\nabla\psi_k| + \sum_{j=1}^{N_{dom}}|\nabla\psi_j||\nabla\psi_T|}\right)^{\beta}, \quad (5.6)$$

where N_{dom} is the number of domain parameters and β is the weighting factor exponent [2]. These weighting factors identify the two types of boundaries: the particle-electrolyte and particle-particle boundaries. Note that, for the dilute electrode, the third term on the right-hand side of Eq. (5.4) vanishes, $W_{r,i} = 1$ at all electrolyte-particle interfaces, and the original SBM equation is recovered (Eq. (2.46)).

For the electrostatic potential in the electrolyte, Eq. (2.52) is reformulated to consider the multiple reaction rates from the multiple particle domain parameters,

$$\nabla\cdot[(1-\psi_T)\frac{F}{RT}(z_+D_+-z_-D_-)C_e\nabla\phi_e] = \sum_{i=1}^{N_{dom}} W_{r,i}|\nabla\psi_i|\frac{r_{Li,i}}{\upsilon_+}+\nabla\cdot[(1-\psi_T)(D_--D_+)\nabla C_e], \tag{5.7}$$

where the electrolyte domain is represented by $1 - \psi_T = 1$. For the concentration evolution of the electrolyte, Eq. (2.55) is reformulated in a similar manner,

$$\frac{\partial C_e}{\partial t} = \frac{D_{amb}}{1-\psi_T}\left[\nabla\cdot\left((1-\psi_T)\nabla C_e\right)\right] - (1-t_+)\sum_{i=1}^{N_{dom}} W_{r,i}\frac{|\nabla\psi_i|}{1-\psi_T}r_{Li,i}. \tag{5.8}$$

Note that, Eqs. (5.7) and (5.8) reduce to Eqs. (2.52) and (2.55), respectively, for a dilute electrode.

5.3 Parameters

The parameters employed in the simulations are summarized below. The diffusivities of Li in the particles and of the electrolyte are assumed constant. In the particles, Li diffusivity is set to be $D_p = 5 \times 10^{-13}$ cm^2/s, which is comparable to those found in literature [64, 65]. While larger values have also been reported [75, 76], D_p here is large enough to result in a nearly uniform Li concentration within the cathode particles at the applied currents imposed in this study, and thus, the results would not depend significantly on this parameter. We take $LiPF_6$ salt in a propylene carbonate solvent as the electrolyte solution, where the diffusivities of the ions are taken to be $D_+ = 7.3 \times 10^{-7}$ cm^2/s and $D_- = 1.5 \times 10^{-6}$ cm^2/s for Li^+ and PF_6^-, respectively. These

values of the ionic diffusivities were measured for the electrolyte at a concentration of 1 M (mol/L) [77], which is the average electrolyte concentration of the electrolyte solution assumed. We take the permeability of the particle-particle interface, P, to the conservative value of 1×10^{-7} cm/s. This value is equivalent to 5×10^{-14} cm^2/s if an interfacial thickness of 5 nm is assumed, and it is approximately one order of magnitude smaller than the bulk diffusivity of the particle. Simulations are performed for a temperature, T, of 300 K. The site density, ρ, is estimated from the lattice constants to be 0.0228 mol/cm^3 [14], and V_{OC} of 3.42 V is adopted from an experimental value [29]. The exchange current density, i_0', is set to 8.5×10^{-7} A/cm^2. This value was obtained by scaling the experimentally obtained value [60] by a factor of 200 in order to account for the difference between the actual particle surface area and the macroscopic cathode surface area at which it was measured [20]. For the electrostatic potential, as mentioned earlier, we assume that it is uniform throughout the particles. The value of 0.8 is used for β appearing in the weighing factors, which is a numerical parameter that represents processes near three-phase boundaries optimally [2]. The discretization and numerical methods can be found in Chapter II; in this chapter $h = \Delta x = \Delta y = \Delta z$ is set to 2.5 nm.

5.4 Simulation Configuration

5.4.1 Dilute electrode

The dilute electrode consists of 65 particles in a $320 \times 320 \times 300$ nm^3 volume and features a region of approximately 30 nm at the bottom without particles, corresponding to the separator. The configuration is depicted in Fig. 5.2(a). This agglomerate has a volume fraction of 22% active particles. We assume a log-normal distribution of the

particle radii shifted by b, namely with the following probability density function:

$$f_{a,\sigma,b,\tilde{\beta}}(r) = \begin{cases} \frac{1}{\tilde{\sigma}(r-b)\sqrt{2\pi}} \exp\left(- \frac{[\ln((r-b)/\tilde{\beta})-a]^2}{2\tilde{\sigma}^2} \right) & \text{if} \quad r > b \\ 0 & \text{if} \quad r \leq b, \end{cases} \tag{5.9}$$

where r is the particle radius (in nanometers), $a = 1$, $\tilde{\sigma} = 0.2$, $b = 5$ nm, and $\tilde{\beta} = 7.5$ nm. The particle radii range from approximately 18.7 nm to 35 nm.

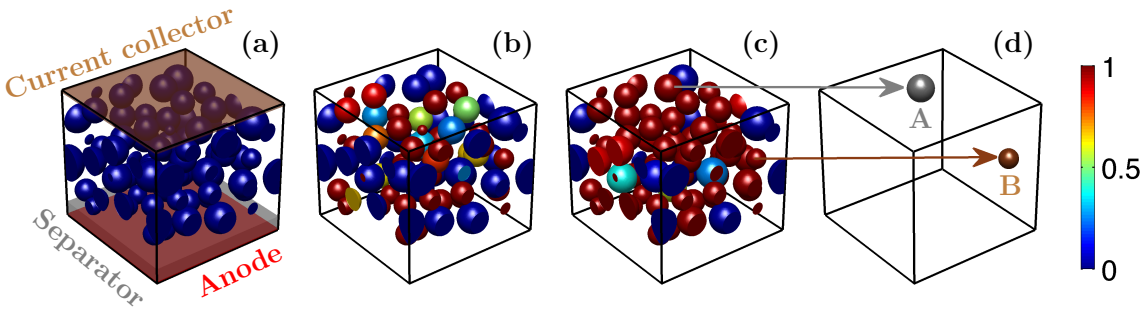

Figure 5.2: Li lattice-site-fraction (0 = $FePO_4$, 1 = $LiFePO_4$) during discharge at C/11.1 in the dilute agglomerate formed by 65 particles. (a) Initial concentration, 2% cell depth of discharge (DOD). (b) At 43% cell DOD. (c) At 71% cell DOD. (d) Two randomly selected particles labeled Particle A and Particle B used for discussion in the text. In (a), the locations of the cathode current collector, separator and anode are indicated.

The domain parameter for each particle $\tilde{\psi}_j$ is created using a hyperbolic tangent function:

$$\tilde{\psi}_j = 1 - \frac{1}{2}\left[\tanh\left(\frac{|\vec{x} - \vec{x}_{j_0}| - r_j}{\xi} \right) + 1 \right], \tag{5.10}$$

where $\vec{x}$ denotes position, and $\vec{x}_{j_0}$ and r_j are the center position and the radius of particle j, respectively. The variable ξ is the interface thickness controlling parameter and is set to $5\Delta x/7$ in order to obtain an interface thickness of approximately three grid points. A cutoff value, ι, is applied to the domain parameter:

$$\tilde{\psi}_j = \begin{cases} 1 & \text{if} \quad \tilde{\psi}_j > 1 - \iota \\ \tilde{\psi}_j & \text{if} \quad \iota \leq \tilde{\psi}_j \leq 1 - \iota \\ 0 & \text{if} \quad \tilde{\psi}_j < \iota. \end{cases} \tag{5.11}$$

The parameter ι is set to 5×10^{-3}. The particles are randomly placed throughout the cell with a constraint that the particles do not contact each other. The particle domain parameters are summed to create a unique domain parameter,

$$\psi = \sum_{j=1}^{N_{tot}} \tilde{\psi}_j. \tag{5.12}$$

5.4.2 Dense electrode

We generate a dense agglomerate with 200, closely packed particles, which are allowed to be in contact with nearby particles. In this cell, the active particle volume fraction was 52%. The simulation volume (for both the cathode and separator) and particle size distribution were the same as that used for the dilute electrode. Because the particles are allowed to be in contact with other particles, additional steps are necessary to create the domain parameter for the agglomerate.

We first create a voxelated domain parameter for each particle in which the domain parameter $\tilde{\psi}_j$ is set to a value of one inside the particle and a value of zero outside the particle,

$$\tilde{\psi}_j = \begin{cases} 1 & \text{if} \quad d_j \leq r_j \\ 0 & \text{if} \quad d_j > r_j. \end{cases} \tag{5.13}$$

The centers of the particles are randomly located throughout the cell. The overlap between two particles (where more than one $\tilde{\psi}_j$ equals one) is limited to 20% of the volume of any single particle. For the regions that overlap, we consider a given grid point to belong to only one particle. The criterion for assigning an order parameter at a given point is the distance inwards from the surface (i.e., the order parameter with the greatest distance is selected). The domain parameters of the 200 particles, $\tilde{\psi}_j$, are grouped into five domain parameters, ψ_j. The grouping is performed such that the contacting particles do not belong to the same domain parameter. The five

domain parameters are added to obtain ψ_T:

$$\psi_T = \sum_{j=1}^{N_{dom}} \psi_j. \tag{5.14}$$

Once the five domain parameters are defined, we smooth the domain parameters using the three-step procedure proposed by Yu et al. [63]. We first apply the Allen-Cahn phase field method to evolve the domain parameters. The Allen-Cahn equation quickly removes sharp interfaces and smooths the interfaces. The equations take the following form:

$$\frac{\partial \psi}{\partial t} = -\mu(\psi) + \epsilon_A \nabla^2 \psi, \tag{5.15a}$$

where ϵ_A is the gradient energy coefficient (set to 0.6) and $\mu(\psi)$ is a non-monotonic polynomial function:

$$\mu(\psi) = 2\psi(1-\psi)(1-2\psi). \tag{5.15b}$$

We apply the Allen-Cahn equation to the particles independently (different $\tilde{\psi}_j$) and to the total electrode domain parameter (ψ_T) to smooth the particle-particle and particle-electrolyte boundaries, respectively. We perform five iterations to ψ_T and ten iterations to 200 $\tilde{\psi}_j$ with $\Delta t = 0.1$. The Allen-Cahn equation can produce a non-uniform thickness at the interface. Thus, we use the level set method initialization as a second step.

To generate a more uniform interface thickness, we use the reinitialization technique from the level set method, in which a distance function is calculated. The distance function Φ is defined as the distance from each grid point to the closest interface; the distances inside a particle are considered negative, and the distances outside the particle are positive. The interfaces are defined as the points where $\Phi = 0$. To initialize the distance function, we first set it to $\Phi = -1$ in the particles (where $\psi_j = 1$), to $\Phi = 1$ in the electrolyte (where $\psi_j = 0$), and to an interpolated value

$-1 < \Phi < 1$ at the interfaces. We then evolve the distance function [78]:

$$\frac{\partial \Phi}{\partial t} = S(\Phi)(1 - |\nabla \Phi|), \tag{5.16}$$

where

$$S(\Phi) = \frac{\Phi}{\sqrt{\Phi^2 + |\nabla \Phi|^2 h^2}}. \tag{5.17}$$

We apply 100 iterations for each of the five domain grouped parameters, ψ_j, with h set at 1.6×10^{-2} and Δt at 1.6×10^{-3}.

Finally, we use a hyperbolic tangent function to convert from the distance function back to the domain parameter:

$$\psi_j = 1 - \frac{1}{2}\left(\tanh\left(\frac{\Phi}{\xi}\right) + 1 \right), \tag{5.18}$$

where ξ is set to $0.89h$. Figure 5.3 shows the domain parameters after the smoothing process. The figure illustrates the five domain parameters ψ_i and the sum of the five different domain parameters ψ_T separately and in different colors. As shown in the figure, the particles in the same domain parameter are not in contact. Both the particle-particle and particle-electrolyte interfaces.

5.5 Results

We simulate the electrochemical process based on the two aforementioned configurations: a dilute electrode and a dense electrode. These configurations represent the case of homogeneously and heterogeneously connected particles, respectively. We present the results for the dilute electrode, followed by the results for the dense electrode. An analysis for both configurations is then presented. The simulation configurations were chosen to facilitate comparison to experimental measurements of LFP composite electrodes.

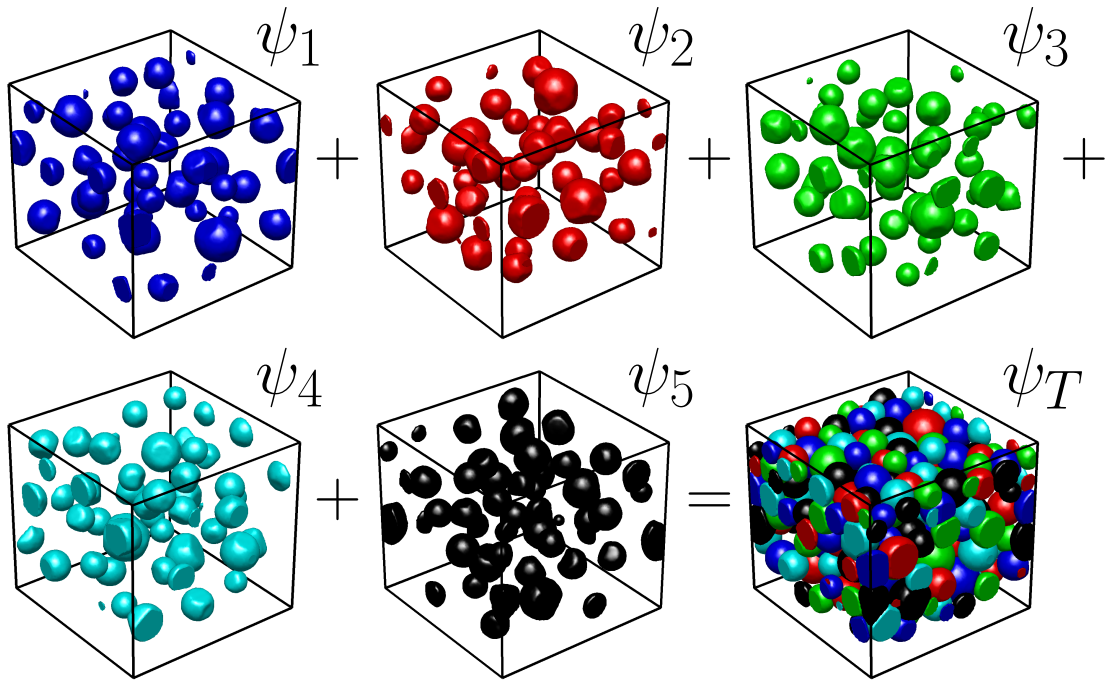

Figure 5.3: Five domain parameters (ψ_1, ψ_2, ψ_3, ψ_4, ψ_5) used to model the dense agglomerate and their sum, (ψ_T). We do not allow contact between particles in the same domain parameter.

5.5.1 Dilute electrode (with homogeneous connectivity)

The dilute electrode is an idealized scenario with optimal ionic and electronic connectivity. Results from the dilute electrode simulations serve two purposes. The first is to remove the effect of the heterogeneous connectivity to gain a general understanding of the lithiation of a multi-particle assembly of phase-separating active particles. Secondly, this configuration serves as the ideal case in terms of the electrode performance as will be shown later.

Figure 5.2 illustrates how lithiation proceeds in a dilute electrode at the lowest rate of discharge considered (C/11.1 rate) at three different snapshots with respect to cell depth of discharge (DOD). As previously mentioned, during the cathode lithiation, two distinct processes occur simultaneously within the cathode: a constant flux of Li ions into the cell and Li redistribution among active particles. The snapshots highlight that the majority of the particles are in either a Li-rich or a Li-poor state during the

entire process, and only a small population of the particles is at an intermediate concentration at any time. For instance, Particle A (highlighted in Fig. 5.2(d)) is nearly fully delithiated when the cell is at 43% DOD but is nearly fully lithiated by the time the cell is at 71% DOD, and Particle B is nearly fully lithiated by 43% DOD. The inhomogeneous lithiation of the particles observed at this current is caused by the Li redistribution between particles, which is more rapid than the overall lithiation of the cell. There is no obvious spatial dependence as to which particles transform in which order, but there is an obvious size-dependent correlation as seen in Fig. 5.4.

The Li content across the entire particle size distribution is shown as a function of cell discharge (at three increasing discharge rates) in Figs. 5.4(a)-(c). Particles are ordered from smallest to largest along the y-axis, the x-axis is the cell DOD, and the color indicates the DOD of the individual particles. The Li concentration evolution in two randomly chosen particles (labeled Particle A and Particle B in Fig. 5.2(d)) is shown in Figs. 5.4(d)-(f). The overall trend, regardless of rate, is that smaller particles transform before larger ones. This is caused by the larger surface area to volume ratio of the smaller particles as Li intake is proportional to the area, and the particle capacity is proportional to the volume. Thus, the smaller particles reach the concentration instability (or spinodal point) that accelerates further Li insertion into the particle before the larger particles. (Note that the tendency for smaller particles to lithiate before larger ones would be reinforced if the equilibrium potential were assumed to be particle-size dependent [79, 80].)

In the zero current limit, it has been proposed that discharging an assembly of particles with a non-monotonic single-particle equilibrium potential results in discrete (sequential) transformation [5]. On the other hand, in the high-rate limit, the magnitude of the applied potential exceeds the difference between the values of the equilibrium potential corresponding to the two concentration instability points, and thus Li insertion would homogeneously distributed among all particles assuming uni-

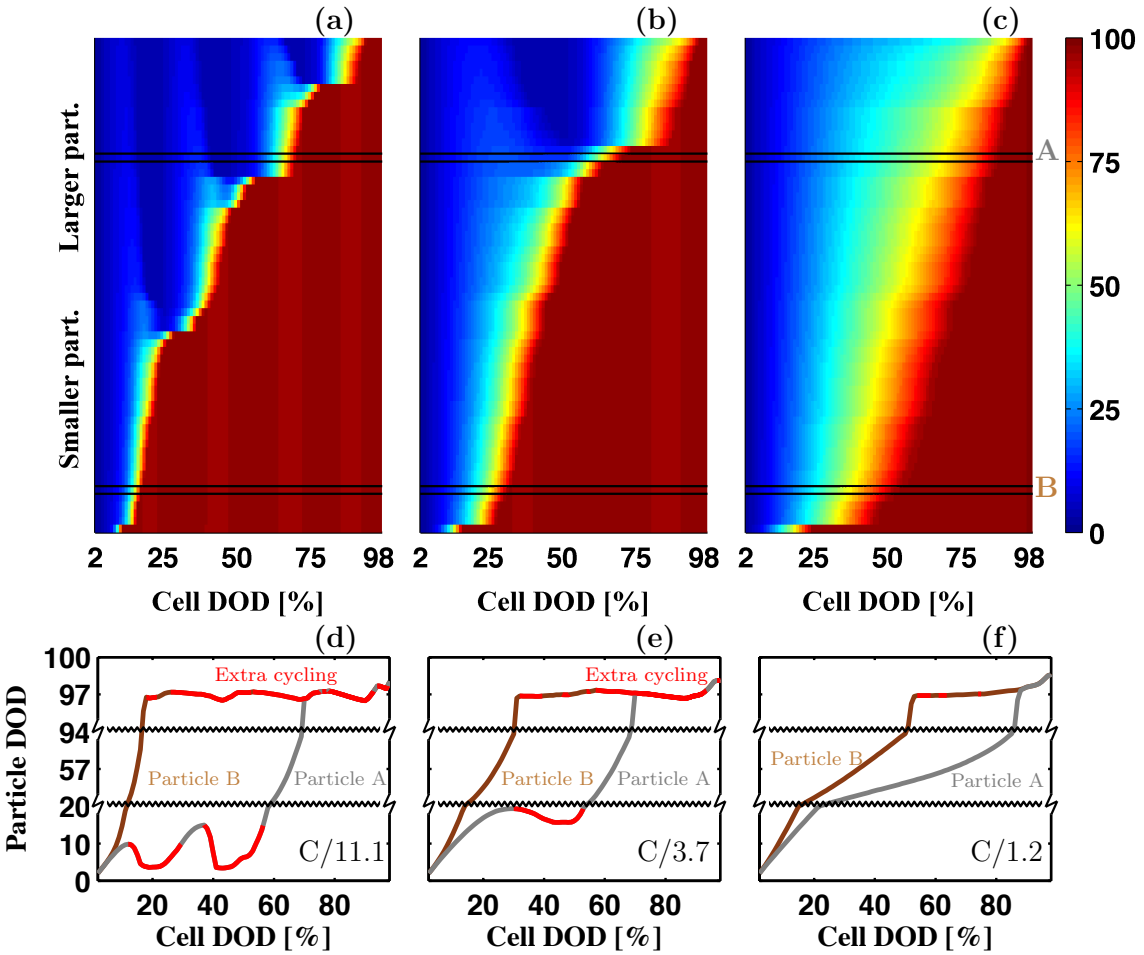

Figure 5.4: (a)-(c) DOD of the particles during discharge arranged from smaller diameter to larger (a) at C/11.1 rate, (b) at C/3.7 rate, and (c) at C/1.2 rate. The color indicates the DOD of the particles from blue (fully delithiated) to red (fully lithiated) as shown in the color bar. (d)-(f) Particle A and particle B during discharge at the same three C-rates. The red portion of the curves indicates the partial delithiation/re-lithiation cycles caused by the particles interactions. The delithiation events seen in (f) are very small and undetectable in this figure (but are noted in red). Note that the y-axis in (d)-(f) is not in linear scale.

form electrostatic potential [1, 20]. In Fig. 5.4(a)-(c), the transition between these two limits can be clearly seen. At the lowest rate, lithiation proceeds group-by-group as observed in Fig. 5.4(a), where there are clearly four groups that transform in sequence. At intermediate rate, shown in Fig. 5.4(b), there are two identifiable groups transforming sequentially, and at higher rates (Fig. 5.4(c)) most of particles transform simultaneously (although smaller particles still transform first). Therefore, as the discharge rate is reduced, the fraction of particles concurrently involved in phase transformation becomes smaller. Consequently, the entire current of the cell must be sustained by a smaller fraction of the particles in the cell. This notion is opposite of what is understood for solid solution systems where the distribution of current over the cell would be homogenized by decreasing the discharge rate.

Several particles exhibit non-monotonic lithiation behavior, partially delithiating before re-lithiating during the course of a single cell discharge, as observed in Figs. 5.4(d)-(f) for Particle A and Particle B. Depending on the rate, each particle within the cell may undergo multiple (partial) delithiation/re-lithiation cycles within a single cycle of a cell, resulting in a significantly higher local rate. Thus, the lithiation process of individual particles is very different from the average across the entire cell. For instance, Particle A in Fig. 5.4(d) (C/11.1 rate) undergoes two Li concentration fluctuations, the first at a cell DOD of $\sim$20% in which the particle delithiates approximately 6%, and the second at $\sim$40% DOD, in which the particle delithiates approximately 11%. Particle A, for example, undergoes an additional $\sim$0.17 cycle (highlighted in red). The amplitude of the oscillation of the particle DOD is larger when the particles are near the lower spinodal while the concentration of the particles remains nearly constant when the particles are nearly fully lithiated. At higher rates, however, the effects of interparticle Li transport and interparticle phase separation become negligible as homogeneous Li insertion dominates (as discussed earlier). Accordingly, Particle A and Particle B undergo less (partial) delithiation/re-lithiation

cycles (i.e., fewer and smaller red regions in Figs. 5.4(e)-(f) than in Fig. 5.4(d) as well as smaller associated concentration drop).

In Fig. 5.5, the cell voltage curve is shown at three different discharge rates along with the single-particle equilibrium potential (solid black curve) and the "single-particle voltage" (dashed curve) superimposed for comparison. The single-particle voltage describes the behavior of an average-size single particle discharging at the same rate. It represents an unphysical scenario where the particles are identical, and are perfectly connected to the counterelectrode (ionically) and to the current collector (electrically) but not to other particles, which prevents the system's free energy from reducing through interparticle Li redistribution. This curve illustrates the scenario where all particles transform simultaneously and independently. Consequently, the characteristic flat voltage profile associated with LFP electrodes is not observed in this scenario, and only when interparticle phase-separation occurs (i.e., through interparticle Li redistribution) a voltage plateau emerges. At C/11.1 rate (Fig. 5.5(a)), the voltage curve strongly resembles the multi-particle equilibrium curve described by Dreyer et al. [5] in which all particles are either nearly fully lithiated or delithiated. In this case, there are four distinct undulations in the voltage which correspond to the four groups of particles transforming in sequence as described earlier, with regions of decreasing voltage corresponding to the interparticle phase separation. As rate increases, the number of undulations (and therefore the number of groups of particles) reduces. At C/3.7 (Fig. 5.5(b)), two undulations are observed, and at C/1.2 (Fig. 5.5(c)) all particles react in one group. At C/1.2, a larger overpotential is required to maintain the constant current, resulting in an increased deviation from the single-particle voltage, but as particles react concurrently, the shape of the curve appears similar to the single-particle voltage. In all the three cases, the difference between the two (cell and single-particle voltage curves) arises from the combination of the effects of the size distribution and of the Li redistribution between particles.

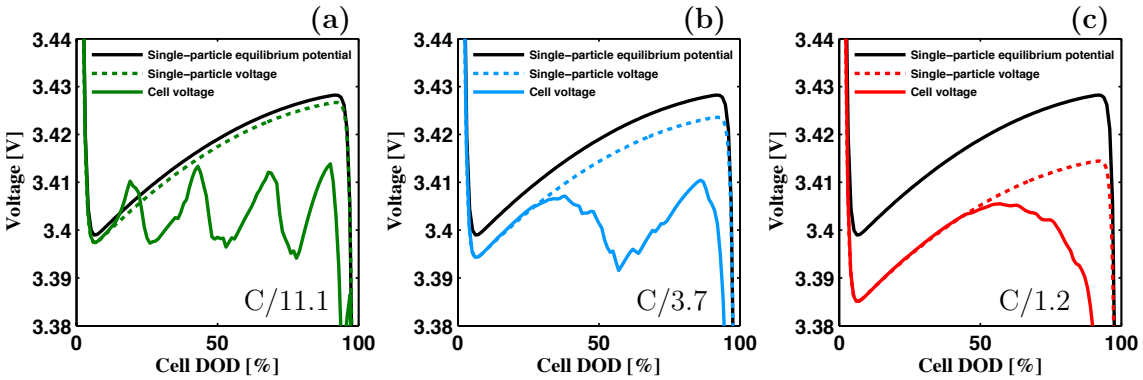

Figure 5.5: Cell voltage (colored solid line) during the discharge of the dilute electrode at (a) C/11.1, (b) C/3.7, and (c) C/1.2 rates. For comparison, the single-particle equilibrium potential (solid black line) and the potential of a single average-size particle would experience at the same rate (dashed colored line, see text) are also plotted.

The interactions in homogeneously connected particles occur only when the current is sufficiently low. As previously mentioned, in this type of connection, Li redistribution only occurs via an electrochemical reaction. Thus, redistribution is limited to the case when the applied potential falls between the local minimum and the local maximum of the equilibrium potential, referred as the inverted potential range (see Fig. 5.6(a)). As illustrated in Fig. 1.10, for significant redistribution to occur, some particles need to have a driving force to lithiate and some to delithiate, which can only occur in this region. Outside of the inverted potential range, all the particles have a driving force for lithiation (except for small concentration fluctuations, as shown in Fig. 5.4(f), noted by the red portions of the curve). When discharging the cell at C/11.1 and C/3.7, the applied potential falls inside the inverted potential range and thus significant redistribution is observed. However, when discharging at C/1.2, this is no longer the case for most of the process and the driving force for redistribution is no longer present. A schematic of the different regimes for cell behavior in homogeneously connected particles is shown in Figs. 5.6(a) and (b)(i). Figure 5.6(b) tabulates the cell behavior that is observed depending on whether the applied voltage is in or outside the inverted potential range.

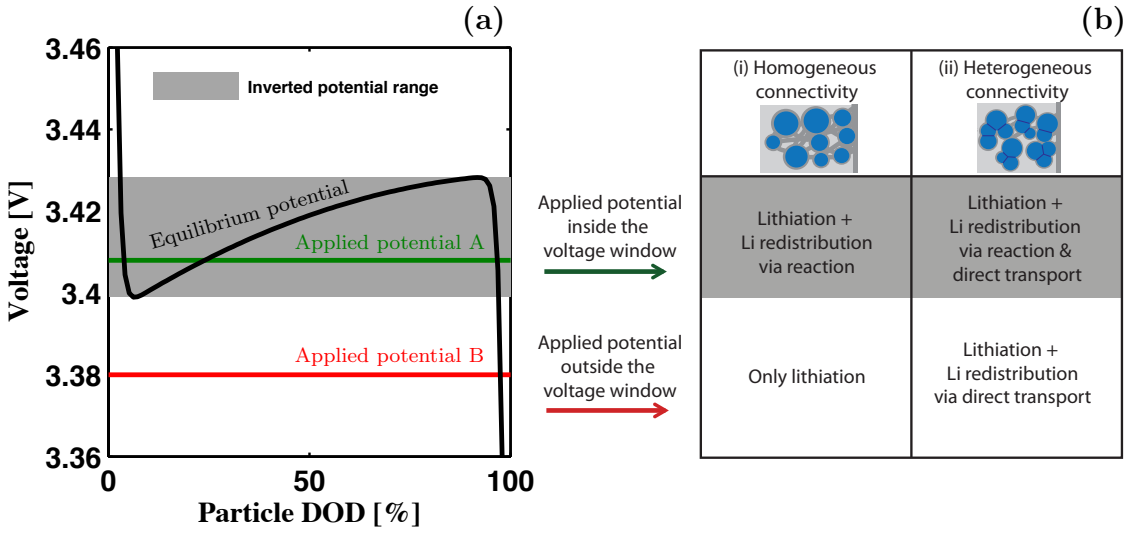

Figure 5.6: (a) Schematic of the applied potential for different scenarios during cell discharge. (b) Cell behaviors observed (assuming the applied potential approximates $\Delta\phi$). (i) For homogeneously connected particles, redistribution via reaction only occurs when the applied voltage is inside the inverted potential range (applied potential A). When the applied potential is outside the inverted potential range (applied potential B), only lithiation can occur. (ii) For heterogeneously connected particles, additionally, redistribution via direct transport can occur at any current.

As DOD increases, the cell potential deviates further from the single-particle voltage because, as some particles complete their transformation, fewer particles must sustain the same cell current density, effectively increasing the local rates. The particles react less uniformly due to the dispersion of the particle size. At C-rates at which the interactions are suppressed, it is more efficient to have a small dispersion in particle-sizes because the magnitude of the overpotential for all particles would be similar at all DODs. At lower currents, where Li redistribution occurs, the electrode should be designed to reduce interparticle Li redistribution since it is a dissipative mechanism that leads to energy loss and the free energy reduction that results from interparticle phase separation decreases the efficiency of the cell.

5.5.2 Dense electrode (with heterogeneous connectivity)

As mentioned earlier, the dilute electrode configuration represents an idealized scenario where there is a homogeneous connectivity between active particles. To better understand the behavior of a more realistic electrode configuration, we use the dense electrode presented above. Here, we introduce an additional mechanism that facilitates Li redistribution between particles when they are in contact with each other (described in detail in the Model Section). Thus, this configuration corresponds to a heterogeneous network that better represents the electrode architecture of a realistic composite electrode in which agglomeration of nanoparticles results in particle-particle contacts.

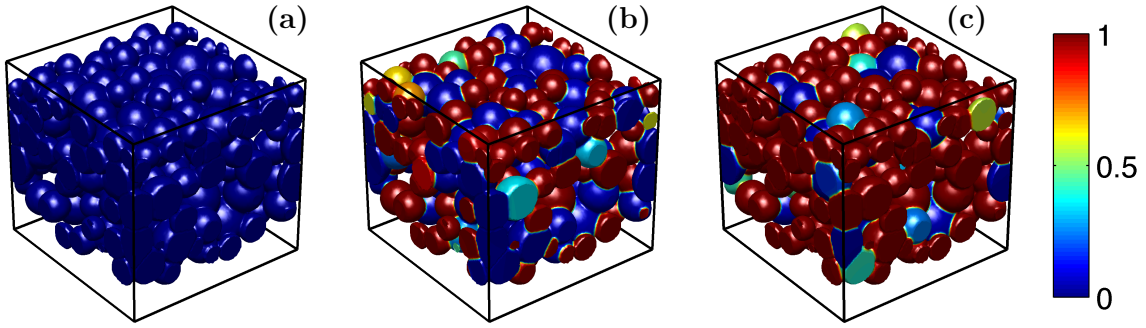

Figure 5.7: Li lattice-fraction in the dense agglomerate composed of 200 particles plotted here during discharge at 1 C-rate. (a) Initial condition with cell DOD = 2%, (b) cell DOD = 43%, and (c) cell DOD = 71%.

Overall, increased particle density and preferential Li redistribution between neighboring particles leads to more sequential (discrete) lithiation for a given rate and generally poorer cell performance, as compared to the dilute configuration. In Fig. 5.7, the arrangement of Li within the cell is shown at three different snapshots in time during a single discharge cycle at 1C. The inhomogeneity in Li distribution across the cell is readily seen in Fig. 5.7(b), with the majority of particles either nearly fully lithiated or fully delithiated. This is similar to the case where the dilute electrode particles transform sequentially. However, in a dense agglomerate this behavior per-

sists at higher rates. For instance, in the dilute electrode, the case with C/1.2 rate shows nearly simultaneous lithiation (Fig. 5.4(c)), while in the dense agglomerate sequential lithiation prevails at 1 C-rate. In the dilute electrode simulations, there is no obvious spatial dependence as to which particles transform after another. In these cases, the order of lithiation is controlled only by the particle size, which changes the surface area to volume ratio of a particle. However, in the dense agglomerate, the order of reaction depends on two factors: First is the ratio between active surface area (i.e., particle-electrolyte interface) and volume of the particle. Second is the active surface area to volume ratio of neighboring particles in direct contact with the particle. (This dependence and the amount of Li redistribution also depends on the crystal alignment of the contacting particles due to the strong anisotropic diffusivity of LFP [75]; however this is not considered here.) For example, if two particles are in contact, the lithiation of the particle with the larger active surface area to volume ratio will be facilitated as it will extract Li from the other particle. Note that active surface area to volume ratio is correlated to the size of the particles; however, the correlation decreases as the contact between particle increases. The influence of cell architecture on battery performance is here apparent as the spatial arrangement of the particles affects the active surface area to volume ratio and the connectivity of the particles.

The individual DOD of the 200 particles ordered by active surface area to volume ratio is given in Fig. 5.8 for three different scenarios. Figure 5.8(a) shows the DOD of the particles during discharge at 1C. The tendency of particles with larger active surface area to volume ratio transforming early is less apparent due to the heterogeneous connectivity in the dense agglomerate. It is also observable that the transformation of the individual particle occurs in a very short period in comparison with the discharge of the cell. Increasing the discharge rate to 10C does not alter this trend; see Fig. 5.8(b). The sequential lithiation behavior still prevails at this rate; the

only difference with respect to Fig. 5.8(a) is that each transformation takes a larger fraction of cell discharge time (as indicated by broader transition between blue and red in Fig. 5.8(b) for each particle). For a direct measurement of the effect of heterogeneous connectivity, we perform an analysis of a dense agglomerate discharged at 1C in which the direct redistribution is prohibited (i.e., we artificially homogenize the connectivity). This could correspond to a case in which all particle-particle contacts are not permeable or have a low permeability to Li (e.g., by the presence of carbon coating blocking the contact area). The DOD of the particles resulting from this case is shown in Fig. 5.8(c). When the particles are homogeneously connected, the order of reaction of particles depends only on their active surface area to volume ratio (similar to the dilute electrode cases).

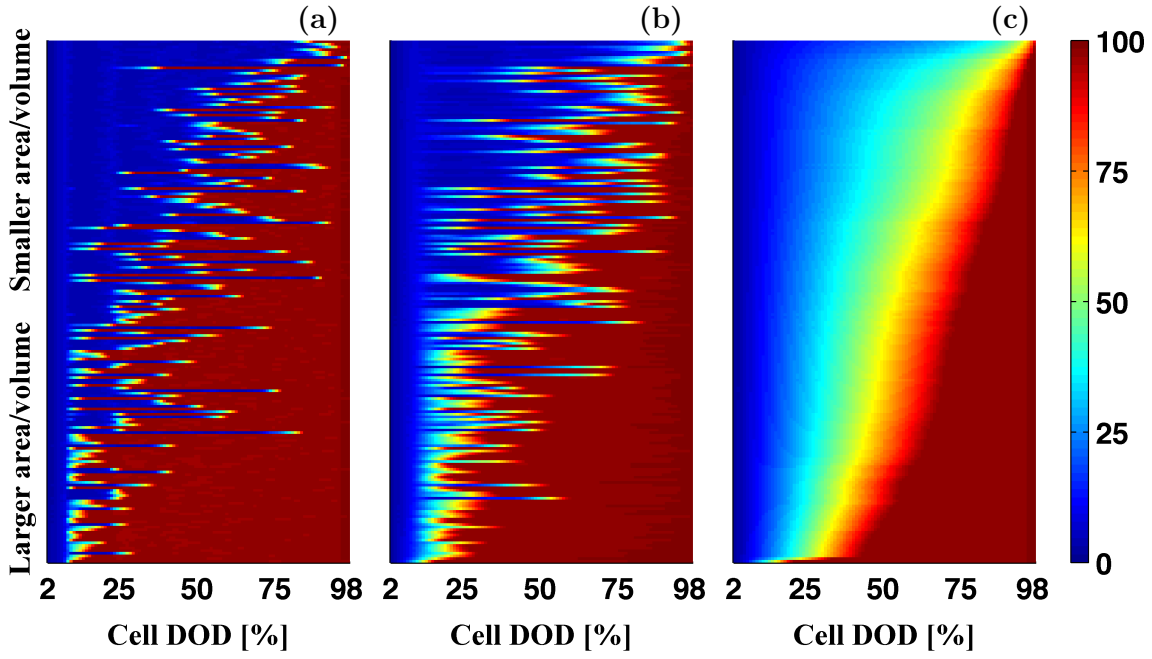

Figure 5.8: DOD of the particles arranged by active surface area to volume ratio during discharge. At (a) 1C and (b) 10C with heterogeneous connectivity. (c) At 1C with homogeneous connectivity.

The cell voltage curves of the dense agglomerate electrode configuration discharged at the two rates considered (1C and 10C) are shown in Fig. 5.9. Superimposed on

each plot are the single-particle equilibrium potential (black solid curve), the voltage curve when the connectivity is homogenized (dashed curve), and the single-particle voltage (dotted curve). The cell voltage for the case with heterogeneous connectivity is slightly lower than that for the case with homogeneous connectivity. This is because heterogeneous connectivity enhances interparticle phase separation, dissipating more energy by Li redistribution. Unlike in homogeneously connected particles, Li redistribution via direct transport can occur at any C-rate as long as the characteristic timescale of the direct transport is smaller or similar to the characteristic timescale of the discharge process. This process depends on the difference of the chemical potential of the contacting particles and the permeability of the boundary between particles (mathematically expressed in Eq. (5.1)), and is independent of the driving force for reaction. A schematic of the voltage regimes and corresponding cell behaviors in heterogeneously connected particles are shown in Figs. 5.6(a) and (b)(ii). Qualitatively, the cell voltage curves for the case with heterogeneous connectivity and the case with homogeneous connectivity (Fig. 5.9) appear fairly similar. However, the lithiation states of particles can be very different as illustrated in Figs. 5.8(a) and (c). This fact is alarming because it demonstrates how challenging it is to extract information about the individual particle states from conventional electroanalytical characterization techniques on composite electrodes [1, 81].

5.6 Analysis

To quantify the interactions of the particles, we perform several analyses for the dilute agglomerate and the dense agglomerate with homogeneous and heterogeneous connectivity. The dense agglomerate with homogeneous connectivity follows a similar trend as the dilute agglomerate and therefore we do not specifically describe it in these analyses. First, we introduce "effective cycles," which account for the additional cycling incurred at the individual particle level due to interparticle Li redistribution.

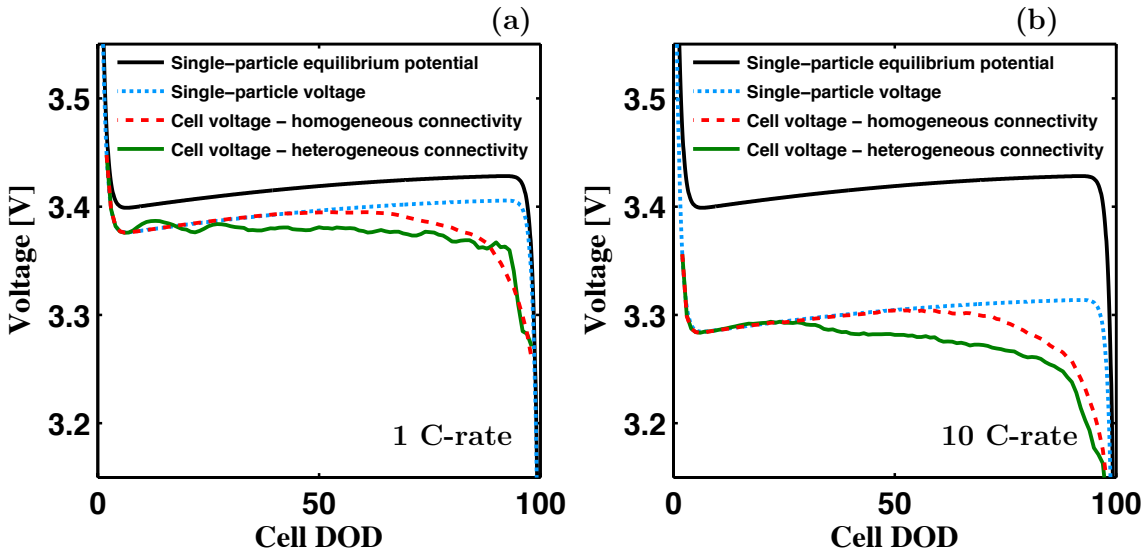

Figure 5.9: Voltage for discharge (a) at 1 C-rate and (b) at 10 C-rate. The solid and dashed color lines indicate the case or heterogeneous and homogeneous connectivity, respectively. The dotted lines indicate single particle voltage. The heterogeneous connectivity increases the hysteresis between particles: the solid line is generally below the dashed line.

Thus, the effective cycles are calculated as the sum of the partial delithiation and redundant re-lithiation of the particles in addition to the full lithiation that occurs during the discharge of the cell. The results are shown in Fig. 5.10(a). The effective cycles are higher at low currents, and tend to a value of one as current increases. Also, at the given rates, the dilute agglomerate undergoes fewer effective cycles than the dense agglomerate. Second, in Fig. 5.10(b) we quantify the number of particles reacting simultaneously by counting the number of particles that have an individual DOD between 15% and 85% [11] and then averaging it over the period that the cell has a DOD in the same range. At lower currents, a small fraction of particles react simultaneously while at higher current, the fraction increases. In the dilute agglomerate, a larger fraction of particles react simultaneously than in the dense agglomerate. Note that the fraction of particles reacting simultaneously does not reach 100% at higher currents. This is attributed to the particle size distribution and the resulting difference of active surface area to volume ratio between the particles.

Last, we calculate the ratio between particle C-rate and the cell C-rate which arises due to sequential versus simultaneous particle lithiation; see Fig. 5.10(c). At lower cell rates, active particles lithiate at a rate an order of magnitude greater than the cell C-rate, but this rate difference between cell and particle diminishes at higher cell C-rates. The ratio of particle-to-cell C-rate does not reach a value of one because some particles have larger area-to-volume ratios that lead to earlier completion of lithiation even when the reaction rate (per unit area) is constant.

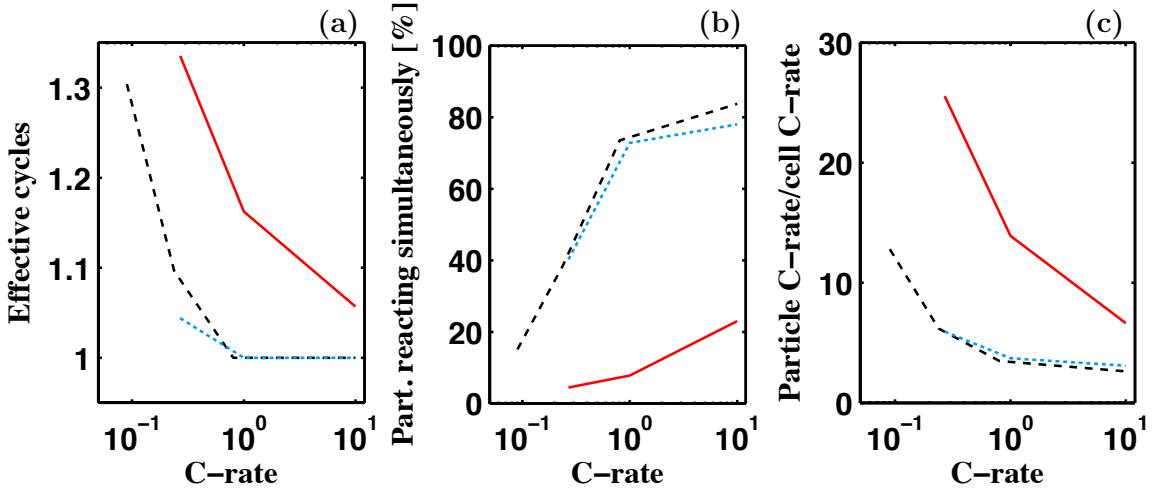

Figure 5.10: (a) Average effective cycles. (b) Percentage of the particles reacting simultaneously. (c) Average reaction C-rate of the particles compared to the cell C-rate. The dashed lines indicate the dilute agglomerate, the dotted lines are the dense agglomerate with homogeneous connectivity, and the solid lines denote the dense agglomerate with heterogeneous connectivity.

These three analyses show that (1) homogeneous connectivity and (2) higher rates reduce effective cycles, enhance simultaneous reaction of the particles, and decrease the ratio of the particle C-rate to the cell C-rate of an agglomerate. The results point to the strong influence of the electrode construction (microstructure and connectivity) on electrochemical behavior of the cell. Furthermore, contrary to intuition, it is observed that discharging at a higher rate leads to potentially beneficial behavior, which will be discussed further below.

5.7 Discussion

In this chapter, we have investigated the effect of interparticle Li transport based on the connectivity of the active particles. As previously mentioned, Li redistribution between particles is a source of inefficiency because the free energy reduction associated with Li redistribution does not contribute to the cell voltage. The contribution of connectivity, therefore, extends beyond simply improving bulk transport in the cell, as it determines the amount of Li redistribution. Homogeneous connectivity facilitates simultaneous transformation rather than sequential transformation of particles, which reduces the local current density on transforming particles (and as a consequence also reduces the overpotential and energy dissipation). High rate performance in LFP electrodes has been observed exclusively when special attention is paid to ensure good electronic and ionic connectivity (notable examples are discussed at length in Ref. [1]). This highlights the importance of optimizing multi-particle kinetics in electrode design rather than a single particle alone. For instance, in the dilute electrode (Fig. 5.4), increasing the rate results in more homogeneous transformation (i.e., each particle DOD approaches the cell DOD). On the other hand, in the dense agglomerate (Figs. 5.8(a) and (b)), increasing the rate does not have a strong effect, and the amplified local current density within the cell does not reduce significantly when discharged at a higher rate. Since Li redistribution underlying these observations are intrinsically detrimental to efficient operation of a battery, the effect of heterogeneous connectivity can potentially explain why high-rate LFP electrodes often require unique electrode architectures that ensure excellent ionic and electronic connectivity between particles [70].

An efficient cell design should minimize Li redistribution. An ideal approach would be a construction where particles are completely isolated from each other but well connected to the electrolyte and current collector. However, since it is unfeasible to construct an electrode where active particles are not connected to each other, the

connectivity between particles should be homogenized as much as possible to at least reduce Li redistribution. This can be accomplished by preventing particle agglomeration and therefore enhancing a more uniform spatial distribution. Particle coating may also play a key role in achieving such result, e.g., by coating of the particles in a way that prevents direct transport. Unfortunately, homogenizing connectivity within a cell typically comes at the cost of reducing the energy density and adding processing steps.

Several experiments support the idea that cell performance can be improved by reducing the interactions between active particles. In the work of Bazzi et al. [3], two different cells were compared, one in which particles had uniform coating and remained isolated from each other (Fig. 5.1(b)), and another in which the coating was non-uniform and particles formed agglomerates with direct particle-particle contacts (Fig. 5.1(c)). As in our simulations, the former case, which corresponds to the homogeneously connected electrode, exhibited a higher voltage in discharge and capacity than the heterogeneously connected electrode. Also, in the work of Chong et al. [69], a significant improvement in the performance of LFP was observed when enough carbon coating was used to fully coat the particles but no significant improvement was found when more carbon coating was used. Moreover, homogeneous connectivity can be achieved by using nontraditional cell architectures, which have been proven to offer an excellent rate performance. Notable approaches include "micro-templating," which enhances the ionic connectivity by forming a three-dimensional (3D) interconnected porous network [82]. Another approach is designing "bicontinuous electrodes," where uniformly distributed active particles with a tight particle size distribution can be constructed with good electronic and ionic contacts through novel synthesis steps and cell assembly. Such systems have been demonstrated for charging/discharging at very high rate [83]. Improvements to cell design at the microstructural level are discussed in detail in Ref. [84]. Since none of these approaches involve modifica-

tions of the active materials, the performance improvement clearly stems from the architecture of the cell. While the observed improvements may be caused by the enhancements in electronic and ionic transport, it may also originate from reducing the interactions between active particles, as indicated by our simulation results.

Our work can help explain the phenomena observed in the scanning transmission x-ray microscopy (STXM) and TEM study of Chueh et al. [11]. In their work, a strong concentration inhomogeneity between particles was observed, where the particles were either nearly fully lithiated or delithiated. This observation is consistent with our simulation results, in which there is no nucleation event, and hence these experimental and modeling observations cannot be used to conclude that nucleation is a limiting factor. Another key observation of Chueh's work is that the lithiation state of the particles appears to lack an obvious particle-size dependence. However, a size dependence has been observed in the experimental work of Robert et al. [21]. Our model can help reconcile these two different observations. The size dependence in the order of reaction in our simulations is more significant when particles are homogeneously connected and less significant when particles are heterogeneously connected. Thus, we surmise that the connectivity plays a role in the conflicting observations made by Robert et al. [21] and Chueh et al. [11] Note, however, that in systems containing large particles (as in these two experiments), bulk diffusion could be the limiting step in the intercalation of the large particles [85], and thus these particles would be less prone to Li redistribution and would have a lower dependence on particle connectivities.

5.8 Conclusion

In this chapter, we explore the consequences of discharging a multi-particle assembly of phase-separating active electrode nanoparticles within an electronic and ionic conducting network, representative of the typical structure of porous Li-ion battery

cathodes. Our model includes rich physics and dynamics similar to those experimentally observed in LFP. The simulation results offer a new, alternative explanation of the lithiation process. Unlike in systems where solid solution is the equilibrium state, the state of the electrode (i.e., each particle DOD) cannot be described only by the cell voltage when there exists a thermodynamic driving force for phase separation. In fact, in this model, the multi-particle (de)lithiation path has additional dependence on the cell architecture (or connectivity between particles) and the imposed cell rate. In both homogeneously and heterogeneously connected electrodes, not only do particles transform discretely at low currents upon charge/discharge, but they also undergo Li concentration fluctuations due to Li redistribution between particles. Such discrete transformation leads to three undesired phenomena: amplification of local rates compared to the overall cell rates, increased effective cycles due to redundant cycles, and resulting energy dissipation. At higher rates, however, active particles within the electrode react more simultaneously in a homogeneously connected electrode as the effect of interparticle Li redistribution is reduced. Unfortunately, this improvement at higher rates is contingent on the connectivity of the particles. Heterogeneously connected electrode particles still transform discretely even at these higher rates. These findings highlight the importance of optimizing cell architecture especially in the design of electrodes constructed with nanoparticulate phase-separating materials.

CHAPTER VI

EFFECT OF A SIZE-DEPENDENT EQUILIBRIUM POTENTIAL

6.1 Introduction

Particle size affects (de)lithiation dynamics in multiple forms. In the first form, as explored in Chapters IV and V, the surface-to-volume ratio difference allows smaller particles to reach the miscibility gap faster and to initiate interparticle phase separation. A second form is the difference in the equilibrium potential between particles of different radii. A dependence of the equilibrium potential on the particle size can stem from the difference in surface-to-volume ratio between particles of different sizes [80], which causes the total surface-to-bulk free energy ratio to change with size. Another source of size dependence may be the change in stress in the host structure caused by the Gibbs-Thomson effect [17, 86]. For $LiFePO_4$ (LFP) particles, several studies have suggested that smaller LFP particles exhibit higher equilibrium potentials than larger particles [17, 25].

In this chapter, we include the dependence of the equilibrium potential on the particle size in the particle-level electrochemical dynamics (PLED) model described in Chapter II. For convenience we refer to this dependence as the "size effect." Two configurations are used for the simulations. The first is a configuration consisting of two particles of different sizes, and the second configuration an agglomerate with 65 particles with a log-normal particle size distribution. In addition, we present a derivation for calculating the current at which particles of two sizes react simultaneously,

given the different surface free energies between the two phases.

6.2 Model

The same four governing equations described in Chapter II are employed: (1) the concentration evolution in the particles, (2) charge conservation in the electrolyte, (3) concentration evolution in the electrolyte and (4) reaction at the particle-electrolyte interface. In this chapter, we assume that phase separation cannot occur inside the particles. The first three governing equations are identical to those used in Chapter V; thus, they are not repeated here. For the electrochemical reaction, the same form of the Butler-Volmer equation as that used in Chapter V is employed (Eqs. (2.37) and (5.2)); the only difference is that the equilibrium potential ϕ_{eq} and, consequently, the overpotential, η, depends on the radius:

$$\eta = \Delta\phi - \phi_{eq}(r), \tag{6.1}$$

where $\Delta\phi = \phi_p - \phi_e$ is the electrostatic potential difference across the particle-electrolyte interface, and ϕ_p and ϕ_e are the electrostatic potential in the particles and in the electrolyte, respectively. $\phi_{eq}(r)$ is the size-dependent equilibrium potential. Note that $\Delta\phi$ is nearly equal to the cell voltage because of the small cell size, limited C-rates, and because no other losses are considered. Ignoring nanoscale effects, we model the size effect as inversely proportional to the particle radius. Here, $\phi_{eq}(r)$ is defined as a function of the particle radius, r, according to the size effect:

$$\phi_{eq}(r) = \phi^0_{eq} + \frac{a}{r}, \tag{6.2}$$

where a is a constant quantifying the magnitude of the size effect. Furthermore, ϕ^0_{eq} is the equilibrium potential of an infinitely large particle, defined by the same

polynomial as in Chapter V (Eq. (5.3)),

$$\phi_{eq}^{0} = \{V_{OC} + \left[5(1.05 - 2.1X_p)^{51} - 2.925275X_p^2 + 6.375071X_p - 2.558325\right] \times 10^{-2}\}[\text{V}], \tag{6.3}$$

where V_{OC} is the reference open circuit voltage plateau, $X_p = C_p\Omega$, and Ω is the molar volume of LFP. As can be inferred from Eq. (6.2), the size effect is significant when the particle radius is small. Here, we consider a metastable solid-solution model in which Li concentration remains nearly uniform throughout the bulk and surfaces of the particles, which justifies the constant shift of the equilibrium potential due to the size effect.

The value of a is 1.7×10^{-8} V/cm, which is estimated from the results reported by Meethong et al. [17] based on a difference of 7 mV in the open circuit voltage of 17-nm- and 56.5-nm-radius particles. If the source of the size effect were solely attributed to the surface-to-volume ratio of the particles, as in Ref. [80], the value of a we selected would correspond to a value of $\sigma_{LFP} - \sigma_{FP} = -1.2 \times 10^{-5}$ J/cm^2. Here σ_{LFP} and σ_{FP} are the surface free energy of $LiFePO_4$ and $FePO_4$, respectively. Note that a is an effective parameter resulting from the contribution from various surface orientations present; ab initio calculations indicate that the size effect would be negative for the (010) surface and larger for the remainder of the surfaces [80, 87].

The values of D_p, D_+ and D_- are set to 5×10^{-13} cm^2/s (comparable to the values from Ref. [64, 65]), 7.3×10^{-7} cm^2/s [77] and 1.5×10^{-6} cm^2/s [77], respectively. The electrolyte has an initial concentration of 1 M. The temperature is set to 300 K, V_{OC} to 3.42 V [29] and i_0 to 8.5×10^{-7} A/cm^2 [38]. A constant-current and a no-flux boundary conditions are imposed at the anode-electrolyte and the electrolyte-current collector interfaces, respectively. For the remainder of the box boundaries, a no-flux and a periodic boundary conditions are imposed for the two-particle cell and the agglomerate, respectively. A central finite difference scheme for the spatial discretization with a 2-nm and 2.5-nm spacing for the two-particle and the 65-particle

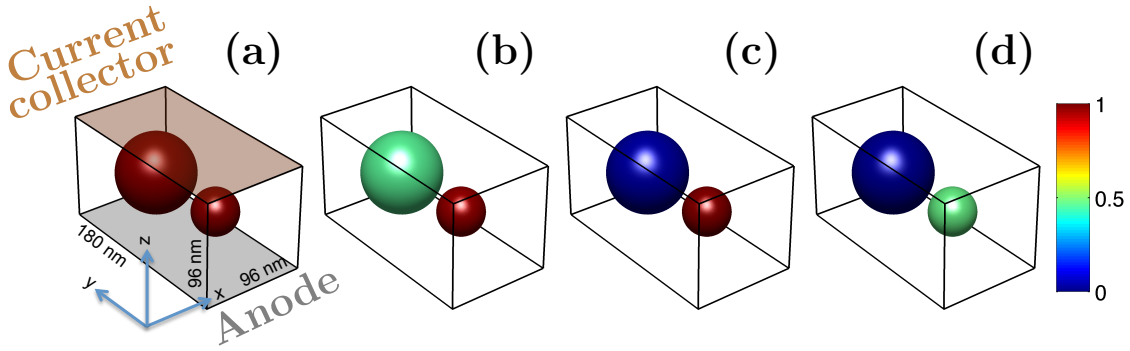

Figure 6.1: Concentration evolution of the two-particle configuration during delithiation at $\bar{i} = 6\%\ i_0$. Four snapshots of the process are shown at different cell depths of discharge (DODs), (a) 98% (initial concentration), (b) 54%, (c) 19%, and (d) 10%. The colors in the color bar represent x in Li_xFePO_4. A schematic of the configuration is included in (a).

configurations are used, respectively. Eq. (2.46) is solved explicitly using an Euler time stepping scheme; Eqs. (2.55) is solved implicitly using and alternating-direction-line-relaxation (ADLR) [2, 52, 51] method. The solution for Eq. (2.52) is also obtained by ADLR every time step.

6.3 Results

The results for the two cells are now described. We only show the results for the particle concentration evolution and the cell voltage, as the electrostatic potential and salt concentration in the electrolyte are nearly uniform due to the small dimension of the cells.

6.3.1 Two-particle configuration

In this section, we use a cell configuration identical to that used in Chapter IV, containing two particles of different sizes. The smaller particle has a 40-nm diameter, and the larger particle has a 70-nm diameter. The dimensions of the domain are $96 \times 180 \times 96$ nm^3. Figure 6.1(a) shows this configuration, which denotes the locations of the anode and current collector.

We first simulate the lithiation-delithiation cycle at $\bar{i} = 6\%\ i_0$ (i.e, the average current at the particle surface is equivalent to 6% of the value of i_0). This current density corresponds to C/12.5 for this cell. Figure 6.2(a) shows the depth of discharge (DOD) for the particles and cell during lithiation. The corresponding voltage is plotted in Fig. 6.2(c) curve (i) with the single-particle equilibrium potentials of the two particles. The size effect produces a higher particle equilibrium potential for the smaller particle, as shown by the black dotted curve in Fig. 6.2(c). The driving force for lithiation is $\phi_{eq}(r) - \Delta\phi = -\eta$. Thus, the size effect enhances lithiation of the smaller particle by increasing $\phi_{eq}(r)$, and consequently the driving force, which further facilitates interparticle phase separation. In addition to this enhancement, the general lithiation dynamics remain similar to the case in which the size effect is excluded, which are shown in Fig. 6.2(d) (DOD) and 6.2(f) curve (i) (voltage). This case was described in Chapter IV; therefore, we do not repeat it here.

The size effect significantly affects the delithiation dynamics at low currents. Figure 6.1 shows the concentration evolution of the particles during delithiation. Initially, both particles are nearly fully lithiated. At $\bar{i} = 6\%\ i_0$, the smaller particle remains lithium-rich until the larger particle becomes nearly fully delithiated; see Figs. 6.1(b) and (c). When the larger particle is fully delithiated, the smaller particle begins delithiation; see Fig. 6.1(d).

Figure 6.2(b) and 6.2(c) curve (ii) show the DOD of the particles and voltage, respectively, for delithiation at $\bar{i} = 6\%\ i_0$. Note that the abscissa in Fig. 6.2(b) is the state of charge (SOC=1-DOD). At the beginning of delithiation, the cell voltage enters the range between the equilibrium potential of the larger particle (solid black curve in Fig. 6.2(c)) and the smaller particle (dotted black curve in the same figure). The driving force for delithiation is $\Delta\phi - \phi_{eq}(r) = \eta$. Therefore, the size effect reduces the driving force for delithiation for the smaller particle. In the case presented in Fig. 6.2(b) and 6.2(c), only the larger particle is driven by the cell voltage to

delithiate for the given current. As the larger particle delithiates, the cell voltage decreases further. Thus, the smaller particle remains nearly fully lithiated. When the larger particle is nearly fully delithiated, the cell voltage increases above the smaller particle equilibrium potential at its upper spinodal point (the local maximum of the equilibrium potential) to maintain the current, causing the smaller particle to begin delithiating. When the size effect is excluded from the model, as shown in Fig. 6.2(e) and 6.2(f) curve (ii), the smaller particle reacts first due to its greater surface-to-volume ratio. The difference between lithiation and delithiation when the size effect is excluded is due to asymmetric equilibrium potential. The smoother shape of the equilibrium potential at the upper spinodal point weakens the interparticle interactions. The size effect enhances the asymmetry in the lithiation/delithiation dynamics by favoring the delithiation of the larger particle.

To further investigate the size effect during delithiation, simulations were performed at two additional currents: $\bar{i} = 18\%\ i_0$ (C/4.2 rate) and $54\%\ i_0$ (C/1.4 rate). (No additional simulations were performed for lithiation because it does not exhibit major differences from the case without the size effect.) The results are shown in Fig. 6.3. A higher current produces a higher overpotential and, consequently, a higher cell voltage. At $i = 18\%\ i_0$, the voltage is sufficiently high such that it exceeds the equilibrium potential of the smaller particle at its upper spinodal point, which facilitates delithiation of both particles at the beginning of the process. However, the larger particle reacts more rapidly than the smaller particle due to the larger overpotential. The voltage decreases as the larger particle delithiates because of its decreasing equilibrium potential. Eventually, the applied potential becomes lower than the equilibrium potential of the smaller particle, which causes the smaller particle to lithiate again to a nearly fully lithiated state. The remaining dynamics proceeds in a similar manner as at $\bar{i} = 6\%\ i_0$. At the highest current considered, $\bar{i} = 54\%\ i_0$, the overpotential is sufficiently large such that the size effect is negligible. The voltage is

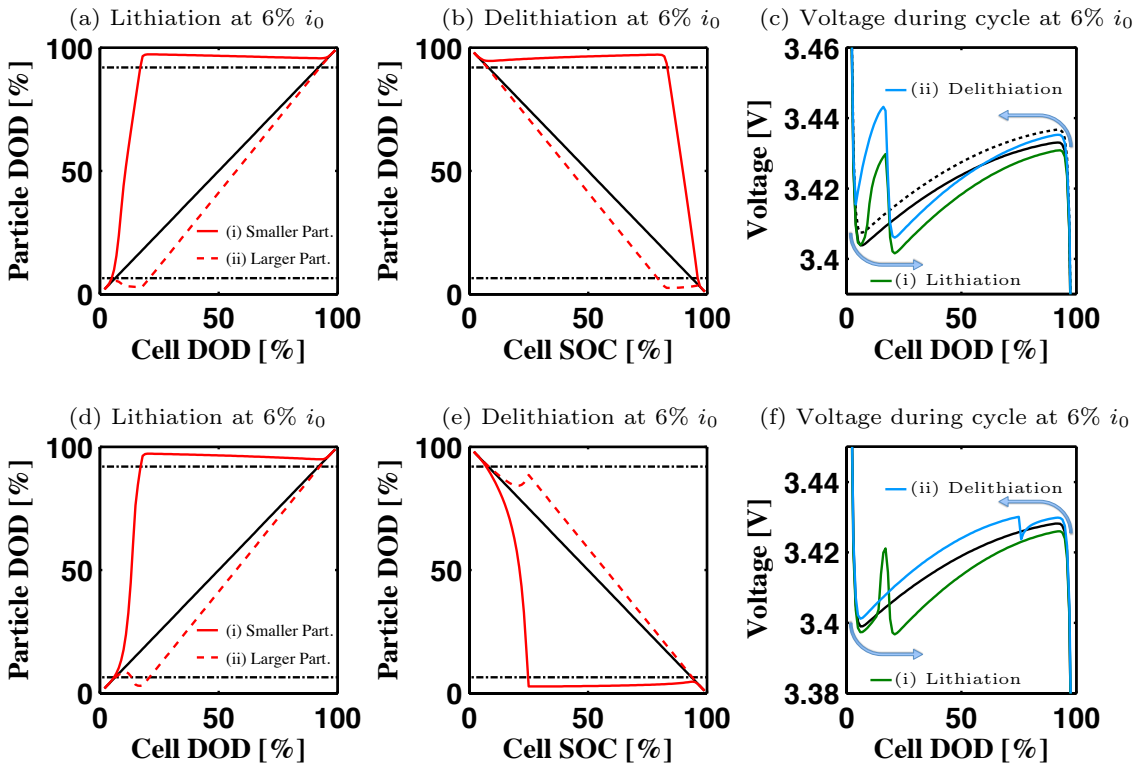

Figure 6.2: The particle DOD and voltage of the two-particle configuration during a lithiation-delithiation cycle at $\bar{i} = 6\%\ i_0$ when the size effect is (a)-(c) considered and (d)-(f) excluded from the calculation. In (a), (b), (d), and (e), the black solid line represents the cell DOD, and the horizontal dash-dotted line represents the spinodal points. In (c), the solid and dotted black curves indicate the equilibrium potential of the larger and smaller particles, respectively; in (f), the solid curve indicates the size-independent equilibrium potential. The horizontal axis in (b) and (e) is the state of charge (SOC = 1 -DOD).

higher than the equilibrium potentials of both particles throughout the entire delithiation process, and the smaller particle lithiates more rapidly than the larger particle due to its larger surface-to-volume ratio.

In this simplified configuration, it is possible to derive an applied current at which the two particles can delithiate at the same rate, even when the two spherical particles have different radii. Here, we assume that transport is not limited (in both the particles and electrolyte) and that the electrostatic potential distribution is uniform throughout the cell. The two particles will delithiate at the same current per volume (proportional to the C-rate) if the particle current normalized by the particle volume

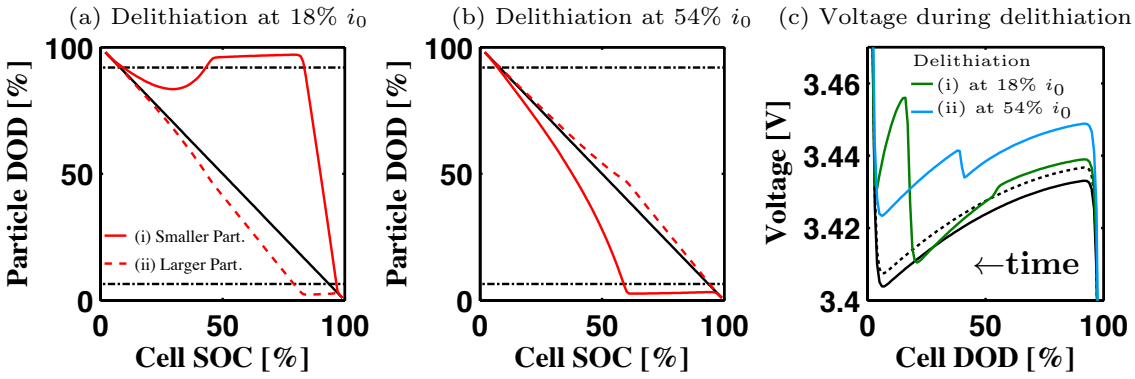

Figure 6.3: The particle DOD and voltage for the two-particle configuration during delithiation at $\bar{i} = 18\%\ i_0$ and $\bar{i} = 54\%\ i_0$. In (a) and (b), the black solid line represents the cell DOD, and the horizontal dash-dotted line represents the spinodal points. In (c), the solid and dotted black curves indicate the equilibrium potential of the larger and the smaller particles, respectively. The horizontal axis in (a) and (b) is the SOC. Note that in (c) the time increases toward the left.

is identical:

$$i_1 \frac{A_1}{V_1} = i_2 \frac{A_2}{V_2}, \tag{6.4}$$

where i_j, A_j and V_j are the particle current density, surface area and volume, respectively, of particle j. At a low current, it is a reasonable approximation to linearize the Butler-Volmer equation, which allows us to obtain the current densities at the particles' surfaces as follows.

$$i_1 = -\frac{Fi_0 a}{RTr_2} \quad \text{and} \quad i_2 = -\frac{Fi_0 a}{RTr_1}. \tag{6.5}$$

See Appendix A for derivation of Eq. (6.5). We calculate the average current density (total current/total particle surface) as

$$\bar{i}(A_1 + A_2) = i_1 A_1 + i_2 A_2. \tag{6.6}$$

The expressions for i_1 and i_2 from Eq. (6.5) are substituted into Eq. (6.6) to obtain the following,

$$\bar{i} = -\frac{Fi_0 a}{RTr_1 r_2} \frac{(r_1^3 + r_2^3)}{(r_1^2 + r_2^2)}. \tag{6.7}$$

Equation (6.7) is also applicable to a cell containing particles of two different sizes that are evenly distributed between the two sizes with the same number of particles of each size. This equation can be easily generalized to account for different number of particles in each size group.

In our aforementioned simulations, the order of delithiation of the particles changed between $\bar{i} = 18\%\ i_0$ and $\bar{i} = 54\%\ i_0$. According to Eq. (6.7), the transition should occur at $\bar{i} = 29.4\%\ i_0$. To verify this prediction, we performed several simulations with applied currents of various magnitudes at approximately $\bar{i} = 29.4\%\ i_0$. The transition occurred at applied currents between $\bar{i} = 27.9\%\ i_0$ and $\bar{i} = 28.8\%\ i_0$. The small discrepancy between the prediction and simulation is attributed to the approximations in the derivation of Eq. (6.7) (including linearization of the Butler-Volmer equation) and the error in the simulation associated with the finite thickness of the smoothed boundary method (SBM) interface [2].

6.3.2 Dilute agglomerate configuration

The lithiation-delithiation dynamics for a cell containing 65 particles are now discussed. The particles are randomly distributed throughout the $320 \times 320 \times 300$ nm^3 domain without allowing the particles to contact one another. An empty region was left in the bottom 30 nm of the domain, which corresponds to the separator. The particles follow a log-normal size distribution, f, with a probability density function:

$$f_{\tilde{a},\sigma,b,\beta}(r) = \begin{cases} \frac{1}{\sigma(r-b)\sqrt{2\pi}} \exp\left(- \frac{[\ln((r-b)/\beta)-\tilde{a}]^2}{2\sigma^2} \right) & \text{if } \ r > b \\ 0 & \text{if } \ r \leq b, \end{cases} \tag{6.8}$$

where r is the radius of the particle (in nanometers), $\tilde{a} = 1$, $\sigma = 0.2$, $b = 5$ nm, and $\beta = 7.5$ nm [38]. The configuration is presented in Fig. 6.4(a) and is identical to the configuration used in Chapter V. Similar to the two-particle configuration, we first describe the lithiation-delithiation cycle at a low current followed by delithiation at

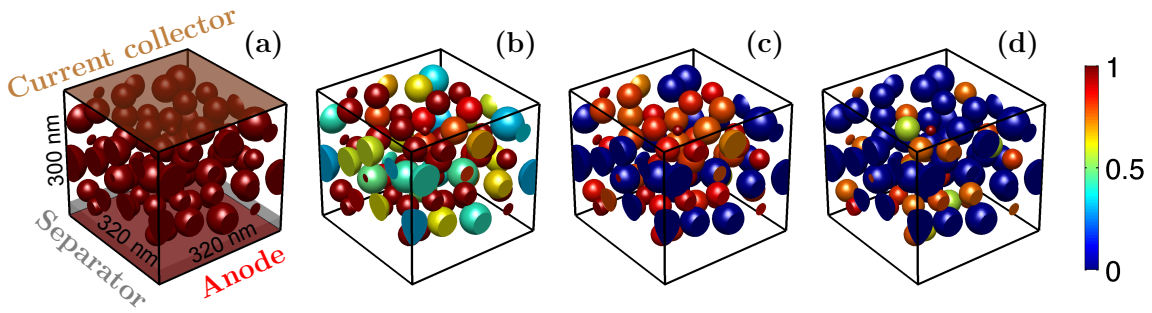

Figure 6.4: Concentration evolution of the dilute agglomerate during delithiation at $\bar{i} = 6\%\ i_0$. Snapshots of the process are shown at four different cell DODs, (a) 98% (initial concentration), (b) 71%, (c) 47%, and (d) 22%. A schematic of the configuration is included in (a).

two additional currents.

The simulation is performed at $\bar{i} = 6\%\ i_0$ (equivalent to C/11.1 rate for this case). Regarding lithiation, Figs. 6.5(a) and 6.5(c) curve (i) show the DOD of the 65 particles, arranged in the order of their size, and cell voltage, respectively. The single-particle equilibrium potentials of the second-smallest (r = 18.7 nm) and second-largest (r = 35 nm) particles are also shown in Fig. 6.5(c). Here, we selected the second-smallest and the second-largest particles and not the smallest/largest because the smallest/largest particles are outliers of the distribution due to the statistically small number of the particles. As in the two-particle configuration, the lithiation dynamics in this simulation are similar to the case in which the size effect is excluded (discussed above and shown in Fig. 6.5(d) and 6.5(f) curve (i)); the only difference is that interparticle phase separation is enhanced. Lithiation begins with the smaller particles, and group-by-group sequential transformation occurs from the smaller to larger particles. During this lithiation process, the cell voltage exhibits five sudden increases and decreases that correspond with the group-by-group transformation of the particles. This behavior has been described in detail in Chapter V, and therefore it is not repeated here.

By contrast, during delithiation, the size effect facilitates delithiation of the larger

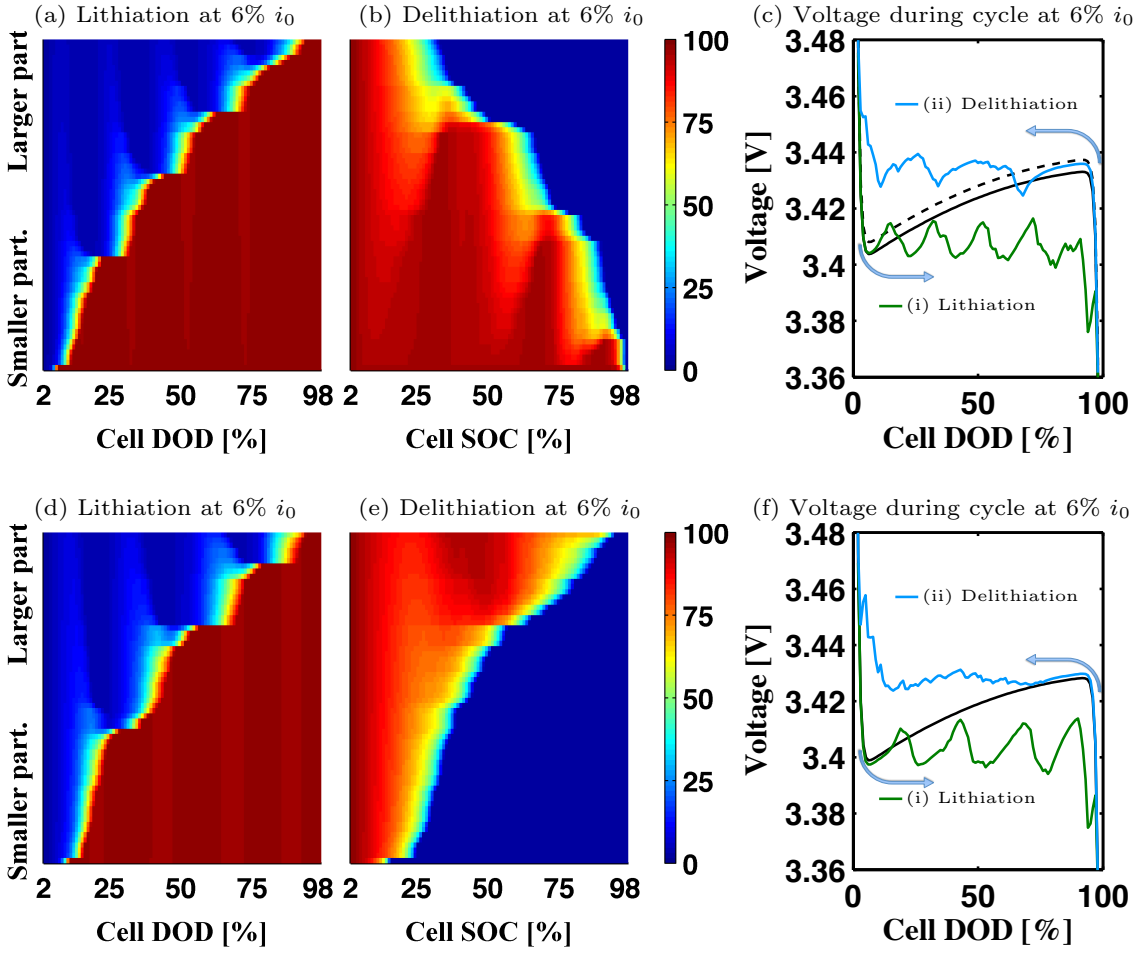

Figure 6.5: The particle DOD and voltage of the dilute agglomerate during a lithiation-delithiation cycle at $\bar{i} = 6\%\ i_0$ when the size effect is (a)-(c) considered and (d)-(f) excluded. In (c), the solid and dotted black curves indicate the equilibrium potential of the second-largest and the second-smallest particle, respectively, as a function of the particle DOD (rather than the cell DOD). In (f) the solid curve indicate the size-independent equilibrium potential. The horizontal axis in (b) and (e) is SOC.

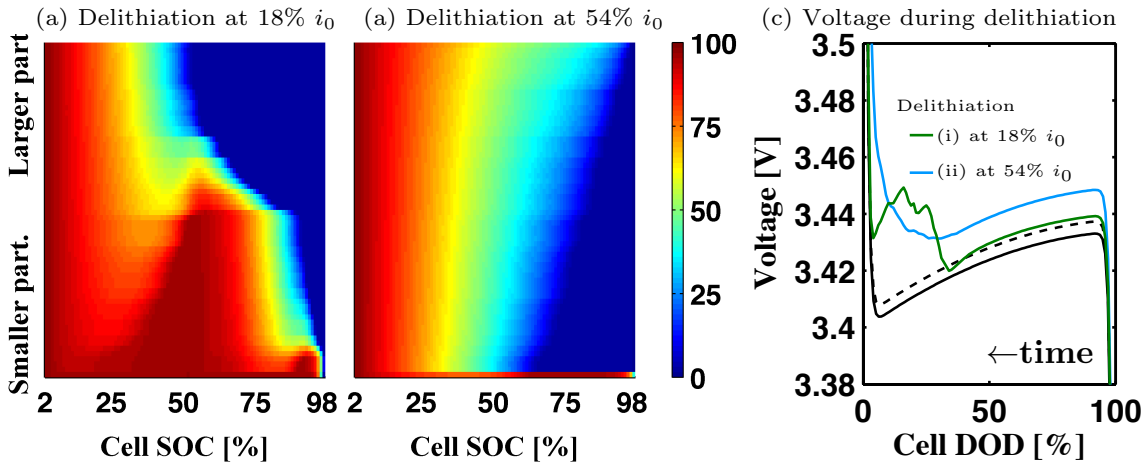

Figure 6.6: The particle DOD and voltage of the dilute agglomerate during delithiation at two additional currents, $\bar{i} = 18\%\ i_0$ and $\bar{i} = 54\%\ i_0$. In (c), the solid and dotted black curves indicate the equilibrium potential of the second-largest and second-smallest particles, respectively, as a function of the particle DOD (rather than the cell DOD). The horizontal axis in (a) and (b) is the SOC (1-DOD). Note that in (c) the time increases toward the left.

particle via the equilibrium potential shift as discussed for the two-particle case. Figure 6.4 shows the concentration evolution of the particles during delithiation. As in the two-particle case, the larger particles delithiate first at low currents. Figures 6.5(b) and 6.5(c) curve (ii) show the DOD of the particles arranged by size and the resulting voltage for delithiation. As with lithiation, the particles react in groups, which produces sudden decreases and increases in the cell voltage. However, when the size effect is included, delithiation begins with the group of larger particles, unlike the case without the size effect, as shown in Fig. 6.5(e) and 6.5(f) curve (ii). An extended analysis of the mechanism underlying the group-by-group transformation is presented on Chapter III. As with the two-particle configuration, the difference between lithiation and delithiation dynamics without the size effect is due to the asymmetric single-particle equilibrium potential.

Van der Ven and Wagemaker [80] suggested that there should be a slight overall tilt in the cell voltage due to the size effect. The simulation result in Fig. 6.6(c) appears to show this tilt, but it is not obvious due to the tight size distribution we

employed and the small value of the constant a. A larger size dependence and/or a wider particle size distribution will enhance the voltage curve tilt.

The delithiation results for two additional currents are described below. The DOD of the particles during delithiation at $\bar{i} = 18\%\ i_0$ (C/3.7 rate) and $\bar{i} = 54\%\ i_0$ (C/1.2 rate) are shown in Fig. 6.6(a) and 6.6(b), respectively. At $\bar{i} = 18\%\ i_0$, the larger particles react first, and the particles react in two groups. Many smaller particles undergo partial lithiation at the cell SOC between 25% and 50%. The results indicate that the size effect remains significant at this current. The cell voltage at this current is plotted as curve (i) in Fig. 6.6(c). Two sudden decreases in the voltage curve are apparent and correspond to the group-by-group interparticle phase separation events. At the early stage, almost all particles are delithiating because the cell voltage is higher than their single-particle equilibrium potentials, as shown in curve (i) at the cell DOD between 50% and 95% in Fig. 6.6(c). The delithiation overpotential of the larger particles is much larger than that of the smaller particles. Thus, the larger particles delithiate more rapidly than the smaller particles, even though the smaller particles have a larger surface-to-volume ratio. At the higher current, $\bar{i} = 54\%\ i_0$, the voltage is sufficiently high such that the size effect is negligible; thus, the smaller particles delithiate first, unlike the previous case. Here, the smallest particle is abnormally small, and thus, the overwhelming size effect hinders its delithiation until all other particles are fully delithiated. In addition, the $\bar{i} = 54\%\ i_0$ voltage is sufficiently high such that interparticle phase separation is hindered [37], and thus, all particles are delithiated nearly simultaneously. Therefore, the particles do not transform in groups.

6.4 Discussion

In portable electronics, intermittent rests during charge/discharge processes (delithiation/lithiation) are common. Because Li transport from/to the counter-electrode is halted, relaxation through interparticle phase separation is the only route toward equi-

librium when intraparticle phase separation is suppressed. Although the size effect may be small, it may be important for determining how phase separation proceeds. Under the assumption that smaller particles have a higher equilibrium potential, smaller particles will favor Li absorption from neighboring larger particles. During delithiation at a higher C-rate, where the size effect is negligible, the smaller particles delithiate before the larger particles. The smaller particles provide a better cell performance in comparison to the larger particles due to their larger surface-to-volume ratio. Thus, the rate performance of the cell will deteriorate as the smaller particles become fully delithiated and the current is supplied mostly by the larger particles. However, this deterioration may be avoided by a pause in the charge process because some of the smaller particles may draw Li from neighboring larger particles during the pause. The delithiation may then proceed similarly as the beginning of the delithiation process, in which the smaller particles delithiate before the larger particles. This process repeats with each pause during the charge process. By contrast, during lithiation the rate performance will degrade by intermittent rests. The smaller particles (which lithiate before the larger particles during discharge) continue to lithiate during the rest periods, extracting Li from the larger particles. Thus, the remainder of the process must proceed through insertion into the larger particles, which requires a larger overpotential for a given rate.

Synthesizing LFP cells with a narrow particle-size distribution can help spatially homogenize the reaction of the particles. However such a task can be challenging and expensive. Instead, for specific battery applications, an alternative approach to improve cell performance can be pursued. Due to the size effect, a particle-size distribution can be optimized to homogenize the charge over a cell for a given C-rate. Equivalently, for a given particle-size distribution, an optimal C-rate can be determined at which the particles delithiate homogeneously (again assuming that the smaller particles have a higher equilibrium potential). However, this type of optimiza-

tion is only desirable for devices in which discharge efficiency is more important than charge efficiency and that are always discharged at the same C-rate (e.g., transmitters, clocks, etc.).

If the larger particles have a higher equilibrium potential, in contrast to the assumption herein, the smaller particles would have a lower single-particle equilibrium potential than the larger particles. In this case, the changes in dynamics due to the size effect would be opposite of what has been described above. The size effect would favor larger particles for lithiation and smaller particles for delithiation and thus would not significantly affect delithiation behavior. However, the lithiation behavior could be reversed such that larger particles would lithiate before smaller particles. For this case, intermittent rest would be beneficial for lithiation and detrimental for delithiation. In such a case, the size effect can be exploited to enhance the rate performance in applications that have intermittent discharge. Candidate materials can thus be screened for their surface energies, in addition to voltage, thermal stability, diffusivity, etc.

6.5 Conclusion

In summary, we analyzed the size effect on lithiation/delithiation of particles in which intraparticle phase separation is suppressed. We first simulated a simple two-particle configuration to systematically analyze the size effect and derive the condition for concurrent delithiation of different-size particles. This was followed by the analysis of the size effect on a group of particles by simulating a system of a 65-particle agglomerate. We demonstrated that, when the smaller particles have a higher equilibrium potential, as suggested by experimental observations, the size effect does not lead to qualitative changes in the lithiation process. On the other hand, the size effect can reverse the order of particle phase transformation at low currents during delithiation. At higher currents, the size effect is negligible even during delithiation. The role of

intermittent rests during the charge and discharge process was also discussed. We showed that discharge rate performance could be enhanced with intermittent rests if the delithiated phase has a larger surface energy than the lithiated phase. This provides an additional material selection criterion for the cathode material selection.

CHAPTER VII

POROUS ELECTRODE SIMULATIONS

7.1 Introduction

In this chapter, we describe three-dimensional (3D) porous electrode simulations of the phase transformation for a full $LiFePO_4$ (LFP) electrode in a coin cell battery. The results are compared to the results of in situ energy-dispersive X-ray diffraction (EDXRD) cell characterization. Replicating the experiment via simulations provides insights into the experimental results. Employing the simulations, we can understand what the limiting factors on the charge/discharge process are. Furthermore, sensitivity analyses of the cell porosity, particle-size distribution and C-rate are performed to propose improvements to the cell construction.

Porous electrode theory (PET) is an efficient approach that allows the modeling of entire battery cells for direct comparison to experimental measurements. However, PET is a simplified approach that cannot be used to study microstructural details. By contrast, particle-level electrochemical dynamics (PLED) simulations can be utilized to study microstructural details but is currently too computationally expensive to model entire cells. PLED simulation results, as those from Chapters III-VI, have some degree of uncertainty as to how the dynamics observed in these small cells translate to entire cells.

We briefly summarize the experimental configuration and results of the EDXRD experiment, which was performed by our collaborators at the University of Cambridge.

The remaining details about the experiments are provided in Ref. [40]. A coin cell cathode was employed in the experiment. The cathode had a diameter of ∼11 mm and a thickness of 300 μm. The diameter of the cathode corresponds to the x- and z-directions and the thickness is y-direction. A two-dimensional representation of the cell is shown in Fig. 7.1. The battery was cycled twice at a C/7 rate with a 24 hour rest between cycles. During the cycles, the depth of discharge (DOD) of different locations of the cathode were obtained using the diffraction patterns obtained from the EDXRD. In the first cycle, the DOD profiles were performed across the y-direction, and in the second cycle, the profiles were performed across both the x- and y-direction.

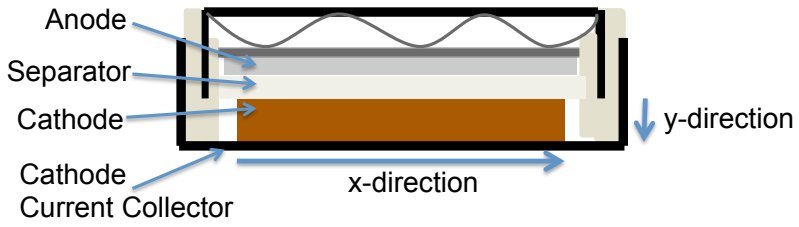

Figure 7.1: Configuration of the cell used for the experimental measurements. The x- and y-directions denote the directions parallel and perpendicular, respectively, to the current collector.

The DOD obtained from the EDXRD profiles in the y-direction during the first discharge (lithiation) are shown in Fig. 7.2. Each marker is a measurement of the local DOD at different overall cell DODs. The regions closer to the separator react before those closer to the current collector. This behavior suggests that Li diffusivity in the electrolyte is the limiting factor for lithiation [28]. Figure 7.3(a) shows the DOD profile in the y-direction during the second discharge. In this case, two different trends are observed: the particles closer to the current collector and the particles closer to the anode react before the particles in the center of the cell. This behavior indicates that, during the second cycle, the limiting factor is not only the diffusivity of the Li in the electrolyte but also the electronic conductivity of the electrode [28].

Finally, in Fig. 7.3(b), we present the DOD profile along the x-direction for the second discharge. The particles closer to the sides react before the particles closer to the electrode center. Furthermore, some asymmetry is observed, which is not expected due to the geometric symmetry of the coin cell, indicating the presence of a nonideality.

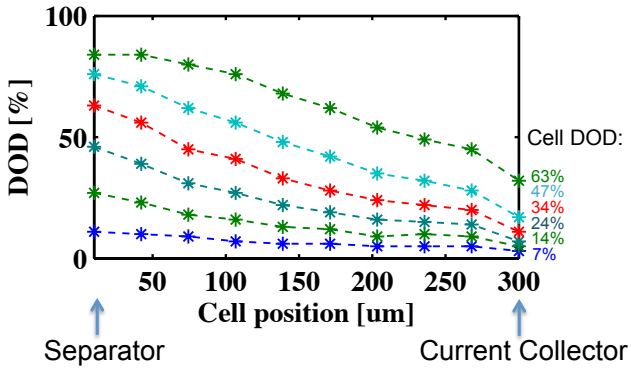

Figure 7.2: Experimental DOD measurements in the y-direction during the first cell discharge of the cell. The experiment was performed by Prof. Grey's group at the University of Cambridge.

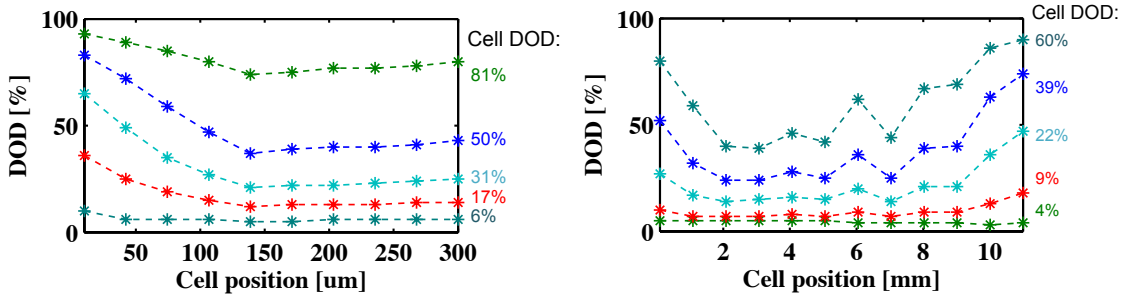

Figure 7.3: Experimental DOD measurements in the (a) y- and (b) x-directions during the second cell discharge. The experiment was performed by Prof. Grey's group at the University of Cambridge.

7.2 Model

Porous electrode theory [45, 88] is used to model the experimental configuration described above during discharge. Five coupled equations are solved to predict the

concentration evolution during discharge of the cell. They describe (1) concentration evolution and (2) current continuity in the electrolyte, (3) concentration evolution and (4) current continuity in the porous electrode, and (5) electrochemical reaction. We consider three relevant phases for this system: active material (LFP), inactive material (carbon and polytetrafluoroethylene (PTFE)), and electrolyte. A domain geometry similar to the experimental cell was employed. Figure 7.4 shows the configuration of the simulation. The casing, which is a cylinder in the experiment, is represented in the simulation by a square prism with the same volume. This approximation is appropriate because, as shown in the results, we do not observe significant gradients in the electrolyte domain on the sides of the cathode.

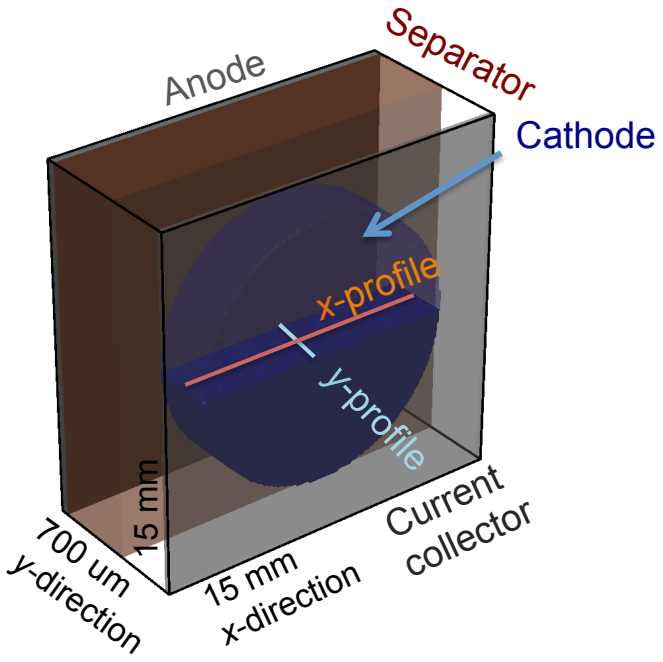

Figure 7.4: Simulation configuration. We use a cylindrical cathode with the same dimensions as the experimental cell. The lines noted by "x-profile" and "y-profile" indicate the lines along which the measurements are made. The graphic is not to scale; the y-direction is magnified by a factor of 10.

7.2.1 Governing equations

In porous electrode simulations, "representative volumes" are used to model the many particles present throughout the cathode. Here, each representative volume is assumed to be composed of ten particles of different sizes that altogether follow a log-normal distribution. The governing equations for porous media are modified to account for the presence of multiple particles in each representative volume (i.e., summation of the terms corresponding to the ten particles are performed). In porous electrode models, the volumetric fraction of the different phases can be represented as:

$$\epsilon_e + \epsilon_s = 1 \tag{7.1}$$

where ϵ_e is the fraction of electrolyte and ϵ_s is the fraction of the solid components. The solid is composed of a fraction of active material, L_p, and a fraction of inactive material, $1 - L_p$.

The governing equations for the electrolyte are the following. For the electrolyte concentration, C_e, we use the concentration evolution equation for a porous medium [45]:

$$\epsilon_e \frac{\partial C_e}{\partial t} = \nabla \cdot \left(\epsilon_e D_{amb} \nabla C_e \right) - \left(1 - t_+ \right) \sum_i \tilde{a}_{p,i} r_{Li,i} \tag{7.2}$$

where C_e is the concentration of the electrolyte, t is time, D_{amb} is the ambipolar diffusivity, and t_+ is the transference number. The terms $a_{p,i}$ and $r_{Li,i}$ are the particle area per electrode volume and the reaction rate of the particle i, respectively. To solve for the electrostatic potential of the electrolyte, ϕ_e, we impose the electroneutrality condition [45],

$$\nabla \cdot \left[\epsilon_e \frac{F}{RT} (z_+ D_+ - z_- D_-) C_e \nabla \phi_e \right] = \sum_i \tilde{a}_{p,i} r_{Li,i} + \nabla \cdot \left[\epsilon_e (D_- - D_+) \nabla C_e \right]. \tag{7.3}$$

where F is Faraday's constant, R is the ideal gas constant, T is temperature, z_j and D_j are the charge number and the diffusivity species j, respectively.

We use the following governing equations for the solid domain. The concentration evolution of the particles is modeled using a pseudocapacitor model (i.e., the concentration of the particles is considered uniform):

$$\frac{\partial C_{p,i}}{\partial t} = \tilde{a}_{v,i} r_{Li,i}, \tag{7.4}$$

where $C_{p,i}$ is the average concentration of particle i. The particle area per particle volume $\tilde{a}_{v,i}$, is defined as $\tilde{a}_{v,i} = A_i/V_i$. Here, A_i and V_i represent the area and volume of particle i, respectively. The term $\tilde{a}_{v,i}$ is related to $\tilde{a}_{p,i}$ by $\tilde{a}_{p,i} = \epsilon_s L_p \tilde{a}_{v,i}(V_i/V_T)$, where V_T is the sum of the volumes for the ten particles in each representative volume. We employ the current continuity equation in a porous medium for the electrostatic potential of the particles,

$$\nabla \cdot [\epsilon_s \kappa_s \nabla \phi_s] = -F \sum_i \tilde{a}_{p,i} r_{Li,i}, \tag{7.5}$$

where κ_s is the effective conductivity of the solid and ϕ_s is the electrostatic potential.

The reaction rate is modeled using the Butler-Volmer equation,

$$r_{Li} = \frac{i_0}{F}\left[\exp\left(-\frac{\alpha F}{RT}\eta\right) - \exp\left(\frac{(1-\alpha)F}{RT}\eta\right)\right], \tag{7.6}$$

where η is the overpotential, i_0 is the exchange current density, and α is the transfer coefficient. For clarity, we here drop the subindex i from the different variables. The exchange current density is defined as [45]:

$$i_0 = \frac{F(k_c^0 a_e)^{1-\alpha}(k_a^0 a_p)^{\alpha}}{\gamma_{TS}} = i_0' \frac{(a_e)^{1-\alpha}(a_p)^{\alpha}}{\gamma_{TS}}. \tag{7.7}$$

where k_c^0 and k_a^0 are the standard rate constants for the cathodic and anodic reaction, respectively. Furthermore, γ_{TS} is the chemical activity coefficient of the transition state approximated as $(1-X_p)^{-1}$ [20], where X_p is the occupied Li site fraction defined as $X_p = c_p/\rho$ and ρ is the Li-site density. The activity of the electrolyte, a_e, is defined as c_e/c_e^0, where c_e^0 is the reference concentration at which the exchange current density

was measured. The activity of the particles a_p, is defined as $a_p = \exp(\mu_p/RT)$. The chemical potential μ_p, is defined based on the regular solution model,

$$\mu_p = RT\left[\ln\left(\frac{X_p}{1-X_p}\right) + \Omega(1-2X_p)\right], \tag{7.8}$$

where Ω is the interaction parameter. The overpotential, η, is defined as $(\phi_s - \psi_e) - \phi_{eq}$. The equilibrium potential, ϕ_{eq}, is approximated to be $V_{OC} - \mu_p/F$, where V_{OC} is the open circuit voltage plateau.

7.2.2 Parameters

The porosity of the cathode is set to be 25%. The remaining 75% of the volume is assumed to be composed of 55% inactive materials and 20% $LiFePO_4$ (LFP). We assume that only 83% of the LFP is active and that the remainder remains inactive throughout the cycling. This approximation is based on the maximum capacity measured in the experiments. In the separator, 84% of the volume is electrolyte and the remainder is inactive material. A log-normal size distribution with an average of 122 nm is used. The average and the standard deviation of the natural logarithm of the variable is 4.679 and 0.5, respectively.

A constant diffusivity is used for the electrolyte. D_+ and D_- are set to 7.3×10^{-7} cm^2/s and $4 \times 10{-}6$ cm^2/s, respectively [77]. D_{amb} and t_+ are obtained from these values using the equations from Newman's and Thomas-Alyea's textbook [44]. For the solid phase, the effective conductivity is set to 4×10^{-2} S/cm during the first cycle simulation and 5×10^{-3} S/cm during the second cycle simulation. For the reaction rate, i_0' is set to 2.975×10^{-6} A/cm^2, similar to the value used in Chapter III. The transfer coefficient is approximated to be 0.2 [89]. A central finite difference scheme with a uniform discretization in each direction is employed. The grid spacing in the x- and z-direction are set at 100 μm while the spacing in the y-direction is set at 10 μm. Equation (7.2) is implicitly solved using the alternating-direction-line-relaxation

(ADLR) scheme described in Chapter II. Equations (7.3) and (7.5) are also solved using the ADLR scheme.

7.3 Results

7.3.1 Simulations of the EDXRD experiments

The simulation results for the first discharge (lithiation) are shown in Fig. 7.5. (The model was parameterized for the discharge only, and therefore the charge process was not considered in this chapter.) Figures 7.5(a)-(d) show four snapshots of the concentration evolution. As in the experiments, the first particles to lithiate are closest to the Li anode. We also observe that the particles closest to the circular side react before those in the center. Figures 7.5(e)-(h) show the concentration of the electrolyte at the same DODs. Throughout the process, the electrolyte in the porous cathode tends to deplete as the particles lithiate, reaching a nearly fully depleted state at the end of the process.

The reaction evolution in the y-direction is shown in Fig. 7.6 (a) at six different DODs for both the simulation and the experimental results. The two sets of results are in good agreement: the slope and the trend matches well, and the values are also close for the most part. For the profile comparisons, the average DOD of the profile is considered representative of the average DOD of the cell and is used to compare the experiment and simulations. The voltages for the simulation and the experiment are shown in Fig. 7.7(b) curve (i) and (ii), respectively. The simulation and the experiment have similar capacities and, in agreement with the experiment, the overpotential starts to increase at a DOD of $\sim$75%. However, the simulation voltage is higher than the experimental voltage (by $\sim$10 - 20 mV). This difference can be attributed to the several simplifications in the model, such as the assumption of electroneutrality in the electrolyte, the lack of consideration of particle contact, and the simplified model for reaction.

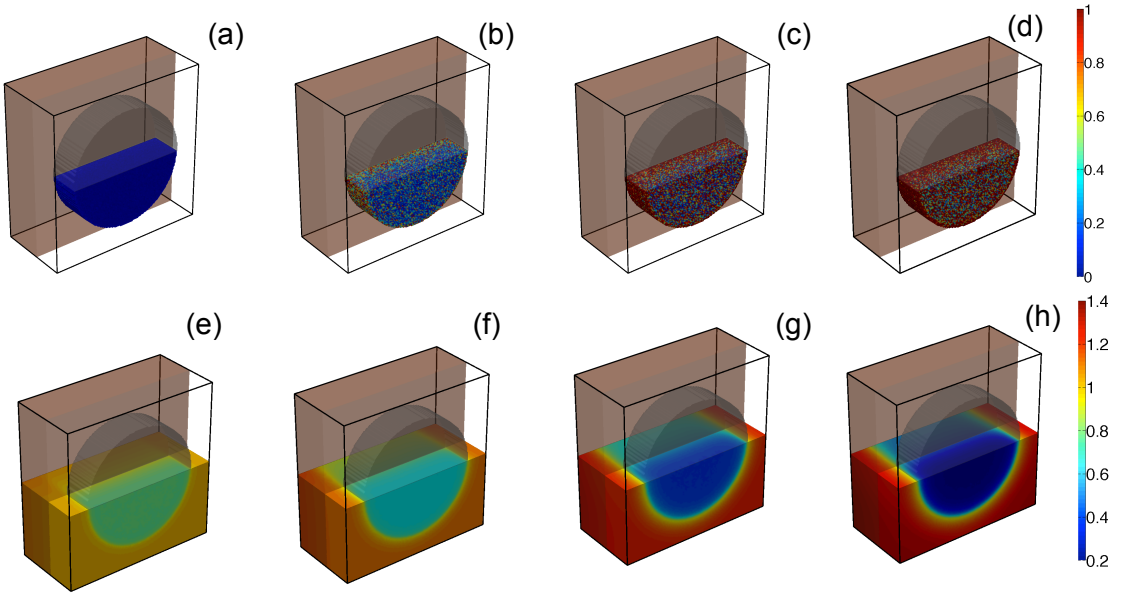

Figure 7.5: Discharge simulation for the first cycle. (a)-(d) Li concentration in the electrode, at (a) 7% DOD, (b) 24% DOD, (c) 47% DOD, and (d) 63% DOD. The color bar represents the Li site fraction. (e)-(h) The electrolyte concentration at the same set of DODs. The color bar indicates the molarity.

A simulation was performed to examine the hypothesis that the effective conductivity is reduced in the second cycle. The configuration and parameters were the same as those used in the simulation of the first cycle, except that the electronic conductivity of the solid components in the electrode was decreased by a factor of eight. Figure 7.8 shows the y-profiles predicted by this simulation. In agreement with the experimental results, two segments are observed, one side having a significant gradient and the other nearly flat, which indicates that two limiting factors are playing a role in the second-cycle discharge. When the electronic conductivity becomes a limiting factor, the driving force for reaction of the particles decreases with increasing separation from the current collector. This limitation offsets the gradient of the Li-diffusion gradient. The resulting voltage for the simulation and the experiment are shown in Fig. 7.7(b) curves (iii) and (iv), respectively. The change in voltage from the first- to the second-cycle simulation is in qualitative agreement with the experimentally observed change; the voltage is slightly lower at the beginning of the

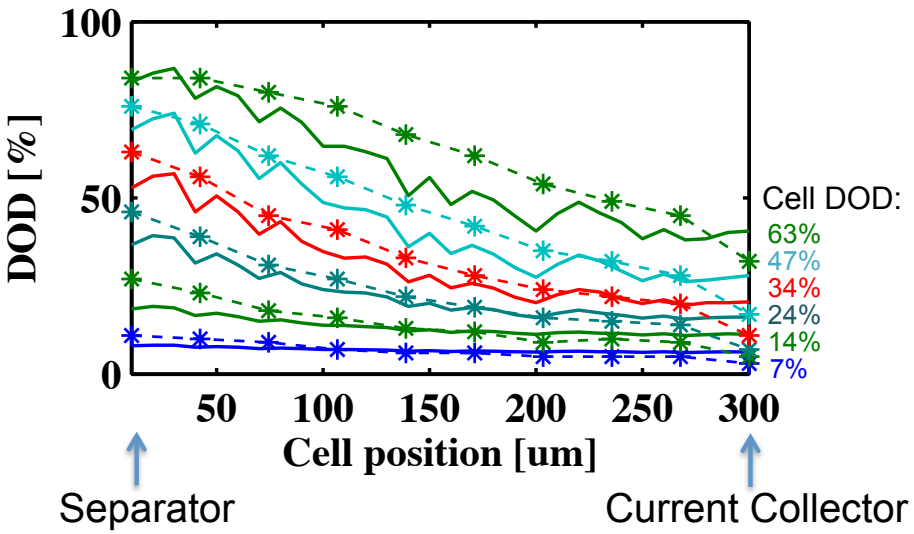

Figure 7.6: DOD in the y-profile for the first discharge. The solid lines indicate the simulation results, and the dashed lines with markers indicate the experimental results.

process and higher at the end. Despite the decrease in the electronic conductivity, the capacity is comparable to that in the first cycle. Therefore, at these low charge rates, the change in conductivity has a negligible affect on the total number of active particles, but instead changes the sequence of reaction of the particles upon cycling, which yields a smaller net reaction gradient across the electrode.

Figure 7.9 shows the simulation results for the x-profiling of the second cycle. In Fig. 7.9(a), when it is assumed that the sample in the experiments from our collaborators is perfectly aligned, the simulation results are symmetrical since there are no asymmetries in any of the governing equations or in the boundary conditions. The agreement between this result and the experiment is poor as the experimental x-profiles show a strong asymmetry. While other causes such as a variation in the pressure on the cell are also possible, we hypothesize that there was a small ($\sim$1 degree) misalignment of the battery in the coin cell holder on the stage, which is within the uncertainty of the experimental setup. Such a small misalignment would cause the sampled region on the right side of the cell to be $\sim$200 μm closer to the

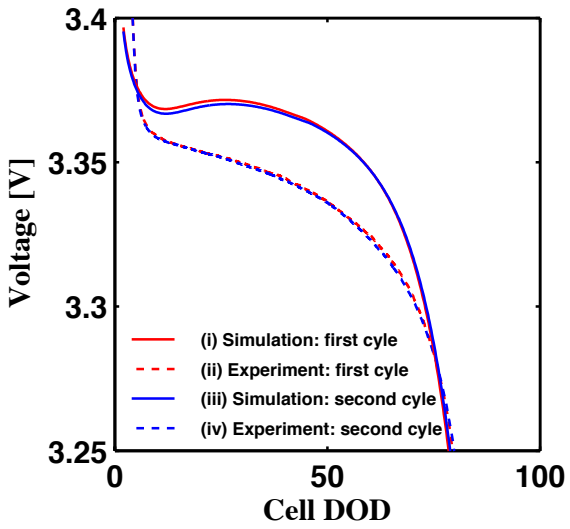

Figure 7.7: Comparison of the experimental and simulated voltages from the first and second discharges.

separator than that on the left side. Figure 7.9(b) shows the results for the tilted x-profiles, which are in good agreement with the experimental results. The tilted x-profiles indicate that the asymmetry in the profiles originate from the higher DOD of the cell closer to the separator in comparison to the DOD closer to the current collector. Furthermore, the agreement between simulations and experiments show that the "cup" appearance of the profiles is due to the pooling of the electrolyte at the edges and not the higher pressures, at least in a coin cell.

7.3.2 Simulations for electrode design

Based on the agreement between the experimental and simulation results, we now employ the simulations to explore further the sensitivities of the gradients in the y-profile to the particle size distribution, porosity, and C-rate. These analyses are performed to extract information that could be utilized to optimize the electrode architecture and are based on the parameters used for the simulation of the second cycle. To quantify the change in dynamics, we measure the Li-fraction gradient across the cell in the y-direction. The gradient is measured at a DOD of 50%, at which the

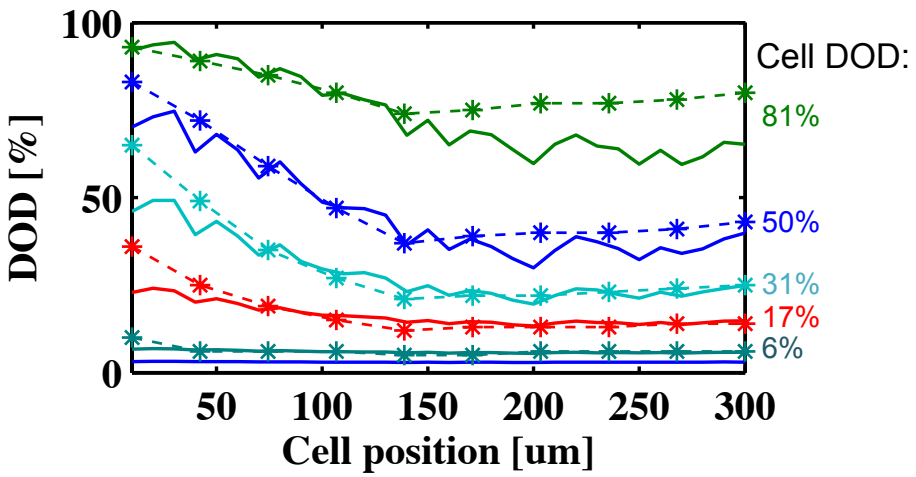

Figure 7.8: DOD in the y-direction for the second discharge simulation. The solid lines indicate the simulation results, and the dashed lines indicate the experimental results.

differences tend to be significant; it is approximated as (DOD near separator - DOD near current collector)/ width.

We first analyze the y-profile for different particle size distributions. For this analysis, two additional log-normal size distributions with the same average particle size were considered: a wider and a narrower particle-size distribution. For the distribution with a wider dispersion, the average and standard deviation of the natural logarithm for the variable are 4.4840 and 0.8, respectively. For the distribution with a narrower dispersion, they are 4.7840 and 0.2, respectively. Figure 7.10(a) shows the probability density of the different distributions, and Fig. 7.10(b) shows the resulting y-profile. We also present the y-profile for the case in which all the particles are considered to have one size (circular markers at cell DOD of 81% in Fig. 7.10(b)). When the distribution is narrower, the position dependence is stronger, which can result in more electrolyte depletion. By contrast, when the distribution is wider, the particles react more homogeneously throughout the cell. Importantly, even though the wider particle-size distribution decreases the net difference in the extent of reaction across the electrode, our earlier work has shown that wider particle-size distributions react

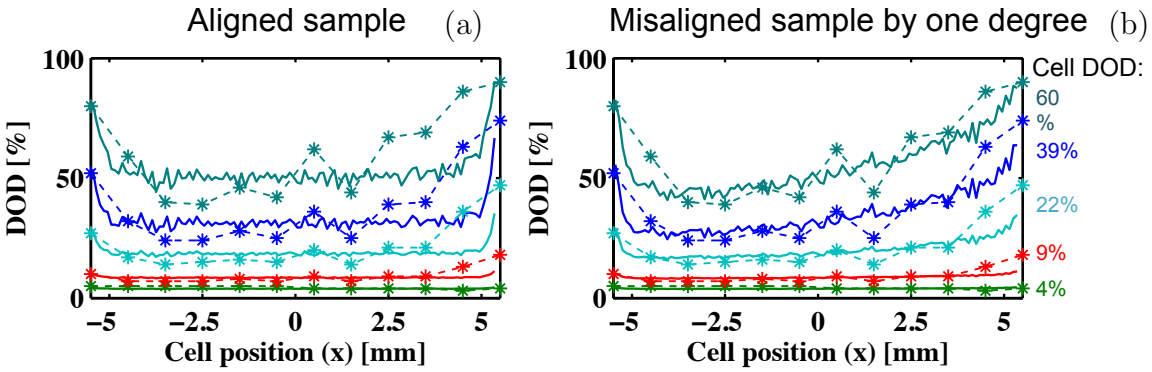

Figure 7.9: DOD in the x-direction for the second discharge simulation. (a) With a perfectly aligned sample. (b) With a sample misaligned by one degree in the y-direction. The solid lines indicate the simulation results, and the dashed lines with markers indicate the experimental results.

more inhomogeneously at shorter length scales. Furthermore, in the case of single-size distribution, the particles react even more inhomogeneously than in the case of a narrow size distribution. The difference in the results illustrates that simple porous electrode models in which only the average of the particle size is employed are not sufficient to model cells in which the size distribution is not negligible.

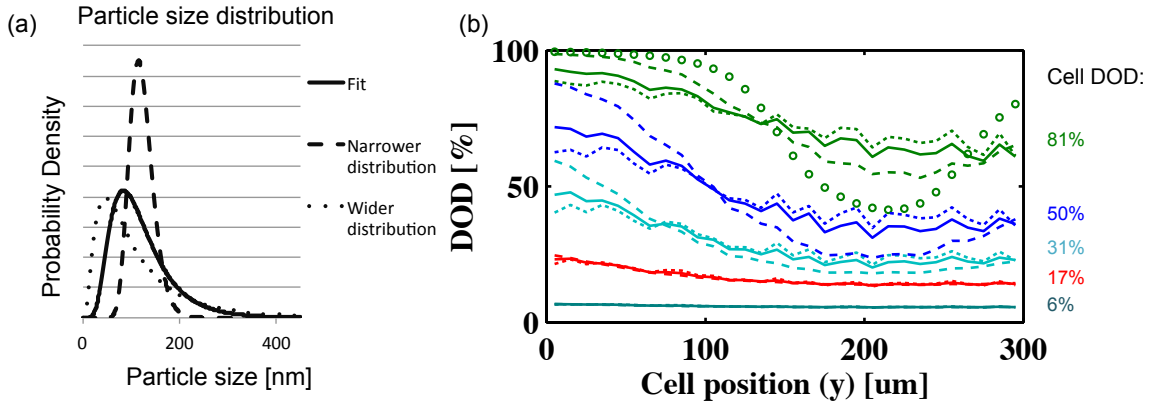

Figure 7.10: (a) Particle size distribution and (b) y-profiling for different size distributions. The solid curves indicate the fitted distribution, the dashed curves indicate a narrower distribution, and the dotted curves indicate a wider distribution. The circular markers (provided only for cell DOD = 81%) indicate the case with single-sized particles.

We next analyze the y-profile gradient responses to porosity. For this analysis, the ratio of active to inactive material in the original distribution remained constant,

and only porosity (the electrolyte volume fraction) was changed. In addition to the original cell, in which the porosity was approximately 25%, we consider 35% and 15% porosities. In Fig. 7.11(a), we calculate the average y-profile gradient for the different porosities and the different size distributions considered above. When the porosity is increased to 35%, the Li-concentration gradient decreases, which can be attributed to a higher effective diffusivity of the ions in the electrolyte. On the other hand, when the porosity is decreased to 15%, the Li-concentration gradient increases. Thus, a higher porosity facilitates the homogenization of particle reactions. A similar trend is observed for the different size distributions. However, it is important to note that when the porosity is increased, the fraction of active material is reduced, thereby decreasing the energy density of the battery.

Finally, we analyze the discharge dynamics at different C-rates. Figure 7.11(b) shows the gradients of the y-profile at C/2 and 0.7C in addition to the original C/7 data for different particle size distributions. The concentration gradients increase as the rate increases, which reflect the fact that, at higher rates, the Li diffusion in the electrolyte becomes more limiting. Interestingly, as the C-rate increases, the dependence of the y-profile gradients on the particle size distribution decreases, and the three different size distributions tend to converge to a similar gradient.

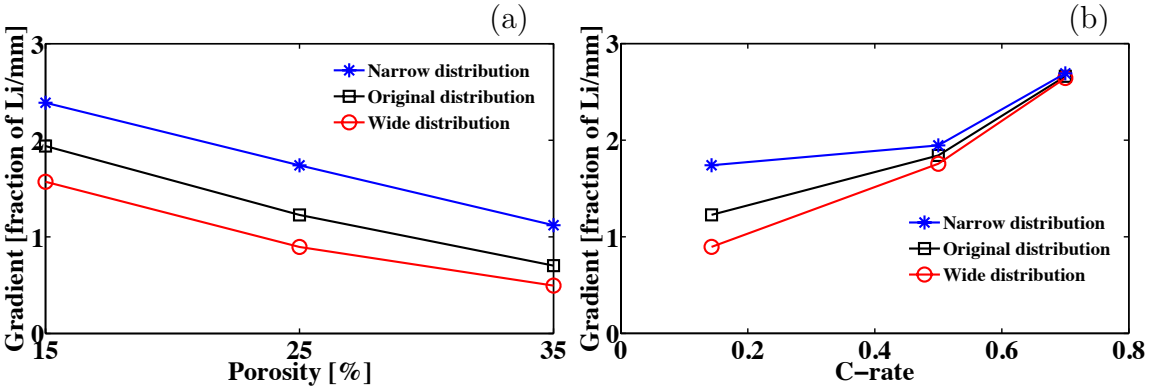

Figure 7.11: Measured y-profile gradient (at DOD = 50 %) as function of (a) porosity and (b) C-rate for the three different particle size distributions.

7.4 Conclusion

In this chapter, we performed 3D PET simulations to model the electrochemical reaction for an LFP coin cell battery. The simulations are consistent with the results of the EDXRD experiments performed by our collaborators. In the first cycle, the particles closer to the anode are the first ones to react indicating that the Li diffusion in the electrolyte is the limiting factor. In the second cycle, in which the effective conductivity is reduced by a factor of eight, the particles near the current collector and the particles near the anode react preferentially than the particles in the middle of the electrode. This dynamics suggest that besides the Li diffusion in the electrolyte, the electronic conductivity is also a limiting factor in this case. The simulation results are consistent with the experimental results. The reduced effective conductivity in the second cycle can be attributed to loss of connectivity due to the expansion and contraction of the particles or due to a formation of a solid-electrolyte interface. A profile in the x-direction was performed for the second cycle, showing that the particles in the sides of the electrode react before the particles in the middle. We also performed simulations in which we varied the size distribution, porosity, and C-rate. When the dispersion of the size distribution is increased, the reaction becomes more evenly distributed throughout the cell. However, it can cause the particles to react locally more inhomogeneously. When the porosity is higher, the particles react more homogeneously; however, the volumetric energy density decreases. When the C-rate is increased, the particles react less homogeneously and the differences caused by the size-distribution become less significant.

CHAPTER VIII

SUMMARY, DISCUSSION AND FUTURE WORK

8.1 Summary

In this dissertation, we studied the electrochemical dynamics of nanoparticulate $LiFePO_4$ (LFP) cell electrodes, focusing on the kinetics of Li redistribution between particles. As analyzed throughout the thesis, particle interactions depend on many factors, such as the position, size, and connectivity. In Chapters III - VI, we employed particle-level electrochemical dynamics (PLED) simulations to analyze the particle interactions on a microscale, while in Chapter VII we used porous electrode theory (PET) simulations to study entire cells on a macroscale.

In Chapters III - VI, we studied the Li redistribution between particles. At low currents, we observed that particles react sequentially and thus Li redistribution tends to be significant. Due to the non-monotonic shape of the single-particle equilibrium potential, at these currents, some particles can lithiate while others delithiate. In the relatively smalls cells studied here, we observed, in most cases, a group-by-group lithiation of the particles. At higher currents, in which the magnitude of the overpotential is larger, all particles in the cell have a driving force to either lithiate (during the discharge process) or delithiate (during the charge process). Thus, all particles react simultaneously, and Li redistribution does not occur.

In Chapter III, we focused on the dependence of the reaction dynamics on the exchange current density as well as on position. We compared two models of the

exchange current density: a cathode-activity-independent and a cathode-activity-dependent exchange current densities. We showed that a cathode-activity-dependent exchange current density can lead to asymmetric charge and discharge dynamics. The position dependence of the reaction dynamics was studied using a simulation configuration with equal-size particles, which isolates the the effect of the particle position. The results provide insights into the electrolyte concentration and electrostatic potential response to the interactions.

In Chapter IV, we focused on how Li redistribution varies between a cell in which the particles undergo intraparticle phase separation and a cell in which the particles undergo interparticle phase separation. We observed a similar dynamics in both cases. At low currents, both particles react sequentially – first the smaller particle followed by the larger particle. At higher currents, both particles react nearly simultaneously with the smaller particle completing the reaction process earlier due to its larger area per volume. We also studied the case in which the larger particle undergoes intraparticle phase separation and the smaller particle interparticle phase separation. In such a case, we observed a change in the order the particles react; the larger particle reacts before the smaller particle.

In Chapter V, we focused on the connectivity dependence of the reaction dynamics. We found that to minimize the Li redistribution and homogenize the reaction of the particles over the cell, the particles need to be (1) ionically and electronically well connected, and (2) not in direct contact with one another. When the particles contact one another, Li can be transported directly between particles chemically (i.e., not electrochemically), which occurs causing the particles to react sequentially.

In Chapter VI, we focused on the effect of a size-dependent equilibrium potential. We observed that, at low currents, the size dependence can lead to an asymmetry between charge and discharge. For the case considered in this chapter, the size dependence significantly affects the delithiation process while it is insignificant during

lithiation. During delithiation at low currents, the size dependence can alter the order of reaction of the particles; in the simulation presented, the larger particles delithiate before the smaller particles. At higher currents, the size dependence becomes almost negligible.

In Chapter VII, we map the reaction of the particles throughout the cathode based on PET. The simulation results are compared to experiments. The simulation results help identify the rate-limiting factors of the cell during lithiation. We also performed a sensitivity analysis of the dynamics on the porosity and size distribution.

8.2 Discussion

The PLED simulations performed herein should be interpreted as a local representation of an electrode and not as that of an entire electrode. Real-size battery cells include material and structural non-uniformities, such as defects in the particles, inhomogeneity in the electrostatic potential, and concentration variations of the electrolyte. As such, the interparticle phase separation is a local phenomenon and not a cell-wide phenomenon; thus, the separation is difficult to observe directly in experiments. In addition, the voltage response to an individual interparticle phase-separation event may be undetectable when averaged over the entire cell. Our work elucidates lithiation/delithiation dynamics at the particle level, which affect the macroscopic behavior of nanoparticulate phase-separating cathodes. As a result, the discrete behavior observed in the PLED simulations is smooth, and cell voltage fluctuations are not apparent. Nevertheless, the particle interactions are local, which lead to an increase in particle C-rates and the effective number of cycles.

Although we studied LFP and assumed in most of the chapters that the particles do not undergo intraparticle phase separation, our predictions may hold qualitatively even if phase separation occurs in some or all of the particles. As analyzed in Chapter IV, the order in which the particles react can change when the system contains

particles that undergo intraparticle phase separation as well as those that do not. Nevertheless, the particles undergo sequential lithiation at low currents and simultaneous lithiation at higher currents. While the particle-size range that may yield a meta-stable solid-solution path is debatable, there is a consensus that particles with a diameter below ∼20 nm do not undergo intraparticle phase separation thermodynamically [42, 17, 18]. Furthermore, the particle size threshold value would increase during the electrochemical processes because phase separation may be kinetically suppressed [43]. As shown in Chapter IV, even if certain particles undergo intraparticle phase separation, there would still be a driving force for Li redistribution. The driving force remains because phase-separated particles have a higher free energy than particles in a Li-rich or Li-poor state due to the energy penalty of the interface and the elastic coherency strain. Due to the small particle size and large Li mobility, the interfaces can be easily moved to the particle surface and then annihilated. Thus, a cell composed of nanoparticles undergoing intraparticle phase separation exhibits some of the behaviors observed herein. More importantly, the findings presented here are also applicable to other nanoparticulate phase-separating materials for which interparticle phase separation is favored.

8.3 Future Work

Integrating PLED and PET simulations can be a powerful modeling approach. The simulation predictions can be enhanced in this manner. As discussed in Chapters III and VII, the two techniques have different limitations: the PLED is computationally expensive, and the PET cannot be utilized to analyze microstructural detail. Therefore, the integrated use of both techniques can facilitate more accurate calculations of particle behavior in the cell. A small cell construct (such as the agglomerates from Chapter V) can be employed to represent different locations of a large cell (such as the electrode from Chapter VII). A PET simulation can be employed to model the

general behavior of a cell. For example, as observed in Chapter VII, particles react inhomogeneously at different cell locations. Results showed that the C-rate for a given region of the cell differs significantly from the cell C-rate. Furthermore, as analyzed in Chapter V, the particle and agglomerate C-rates also differ. Therefore, the particle C-rate can be much greater than the C-rate of the entire cell. The techniques may be combined by first performing the PET simulation, followed by PLED simulations in which the PET simulation results provide the boundary conditions, each representing a small region of the cell; see Fig. 8.1 for a schematic. Using this approach, one could perform simulations that can be directly compared to experiments while taking the microstructural details into account.

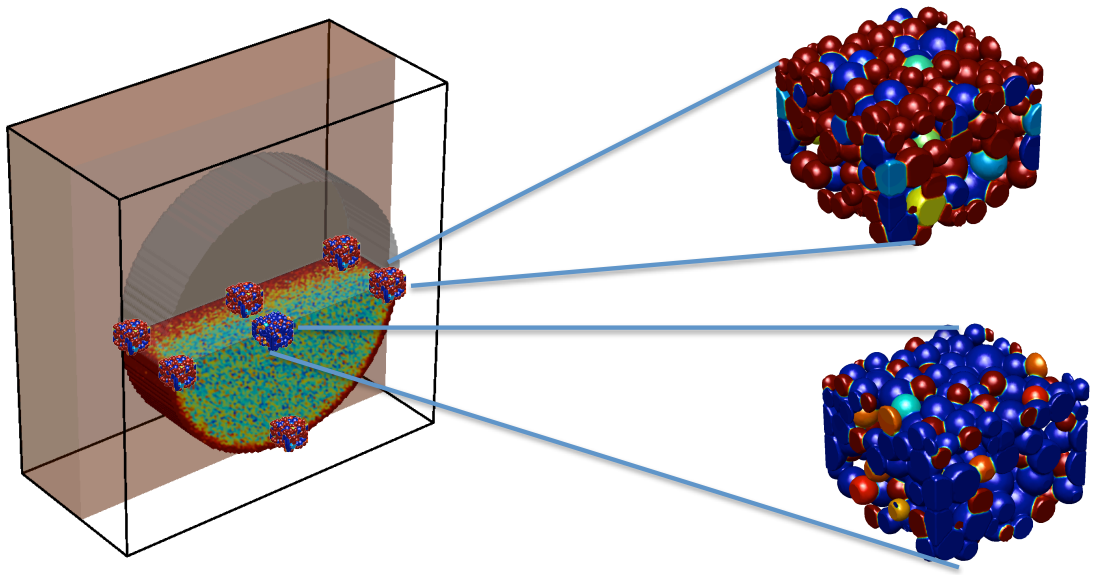

Figure 8.1: Schematic of a multiscale PET-PLED simulation. Different PLED agglomerates (from Chapter V) are plotted next to the PET configuration (from Chapter VII).

CHAPTER IX

CONCLUSION

This work reveals the complexity of the charge/discharge process of nanoparticulate $LiFePO_4$ (LFP) batteries. For the dynamics of these batteries to be fully explained, an understanding on how the particles interact with each other is necessary. We have here shown that the interparticle interactions can vary significantly depending on many factors. The exchange current density can lead to asymmetric charge/discharge. Smaller particles have a larger area-to-volume ratio and thus tend to react before larger particles. Improving the ionic and electronic connectivity between particles and preventing direct Li transport between particles facilitate more uniform reactions over the cell. A size-dependent equilibrium potential can change the order in which the particles react. These aspects are necessary to fully understand and predict interaction dynamics in a real cell, critical for predicting the behavior of and optimizing LFP battery cells.

APPENDIX

APPENDIX A

DERIVATION OF EQ. (6.5)

We begin with the linearized Butler-Volmer equation:

$$i = -i_0\left(\frac{F}{RT}\eta\right), \tag{A.1}$$

where η is defined as

$$\eta = \Delta\phi - \left[\phi^0_{eq} + \frac{a}{r}\right]. \tag{A.2}$$

When two particles react at the same C-rate, their surface current per volume is as follows:

$$i_1\frac{A_1}{V_1} = i_2\frac{A_2}{V_2}. \tag{A.3}$$

For spherical particles, Eq. (A.3) can be rewritten as

$$\frac{i_1}{r_1} = \frac{i_2}{r_2}. \tag{A.4}$$

Substituting Eq. (A.1) into Eq. (A.4) and reorganizing the equation, we obtain the following:

$$\frac{\eta_1}{r_1} = \frac{\eta_2}{r_2}. \tag{A.5}$$

Using the definition from η (Eq. 6.1) and defining $\eta^0 = \Delta\phi - \phi^0_{eq}$ we can express Eq. (A.5) as follows:

$$\frac{1}{r_1}\left(\eta^0 - \frac{a}{r_1}\right) = \frac{1}{r_2}\left(\eta^0 - \frac{a}{r_2}\right), \tag{A.6}$$

and we can solve for η^0,

$$\eta^0 = a\frac{r_2^2 - r_1^2}{r_1 r_2^2 - r_2 r_1^2}. \tag{A.7}$$

Using Eq. (A.1) and Eq. (A.2), we can also write η^0 as a function of i and r for either particle as follows:

$$\eta^0 = -\left(\frac{i_2}{i_0}\frac{RT}{F}\right) + \frac{a}{r_2}. \tag{A.8}$$

Equating Eq. (A.7) with (A.8) and solving for i_2, we obtain

$$i_2 = -\frac{Fi_0 a}{RTr_1}. \tag{A.9}$$

Following the above derivation, we obtain i_1, as shown in Eq. (6.5).

BIBLIOGRAPHY

BIBLIOGRAPHY

[1] R. Malik, A. Abdellahi, and G. Ceder, "A Critical Review of the Li Insertion Mechanisms in $LiFePO_4$ Electrodes," *J. Electrochem. Soc.*, vol. 160, pp. A3179–A3197, Jan. 2013.

[2] H.-C. Yu, H.-Y. Chen, and K. Thornton, "Extended smoothed boundary method for solving partial differential equations with general boundary conditions on complex boundaries," *Modell. Simul. Mater. Sci. Eng.*, vol. 20, p. 075008, Sept. 2012.

[3] K. Bazzi, K. S. Dhindsa, A. Dixit, M. B. Sahana, C. Sudakar, M. Nazri, Z. Zhou, P. Vaishnava, V. M. Naik, G. A. Nazri, and R. Naik, "Nanostructured high specific capacity C-$LiFePO_4$ cathode material for lithium-ion batteries," *J. Mater. Res.*, vol. 27, pp. 424–430, Nov. 2011.

[4] M. S. Whittingham, "Lithium Batteries and Cathode Materials," *Chem. Rev.*, vol. 104, pp. 4271–4302, Oct. 2004.

[5] W. Dreyer, J. Jamnik, C. Guhlke, R. Huth, J. Moškon, and M. Gaberšček, "The thermodynamic origin of hysteresis in insertion batteries," *Nat. Mater.*, vol. 9, pp. 448–453, Apr. 2010.

[6] A. Padhi, K. Nanjundaswamy, and J. Goodenough, "Phospho-olivines as positive-electrode materials for rechargeable lithium batteries," *JOURNAL OF THE ELECTROCHEMICAL SOCIETY*, vol. 144, pp. 1188–1194, APR 1997.

[7] H. Huang, S. C. Yin, and L. F. Nazar, "Approaching Theoretical Capacity of LiFePO4 at Room Temperature at High Rates," *Electrochemical and Solid-State Letters*, vol. 4, no. 10, p. A170, 2001.

[8] Y. Wang, Y. Wang, E. Hosono, K. Wang, and H. Zhou, "The Design of a LiFePO4/Carbon Nanocomposite With a Core-Shell Structure and Its Synthesis by an InSitu Polymerization Restriction Method," *Angew. Chem., Int. Ed.*, vol. 47, pp. 7461–7465, Sept. 2008.

[9] S. Chung, J. Bloking, and Y. Chiang, "Electronically conductive phospho-olivines as lithium storage electrodes," *Nat. Mater.*, vol. 1, no. 2, pp. 123–128, 2002.

[10] S. B. Park, C. K. Park, J. T. Hwang, W. I. Cho, and H. Jang, "Anisotropic lithium ion migration in LiFePO4," *Metals and Materials International*, vol. 17, pp. 1017–1020, Dec. 2011.

[11] W. C. Chueh, F. El Gabaly, J. D. Sugar, N. C. Bartelt, A. H. McDaniel, K. R. Fenton, K. R. Zavadil, T. Tyliszczak, W. Lai, and K. F. McCarty, "Intercalation Pathway in Many-Particle $LiFePO_4$ Electrode Revealed by Nanoscale State-of-Charge Mapping," *Nano Lett.*, Feb. 2013.

[12] V. Srinivasan and J. Newman, "Discharge Model for the Lithium Iron-Phosphate Electrode," *J. Electrochem. Soc.*, vol. 151, no. 10, p. A1517, 2004.

[13] C. Delmas, M. Maccario, L. Croguennec, F. Le Cras, and F. Weill, "Lithium deintercalation in $LiFePO_4$ nanoparticles via a domino-cascade model," *Nat. Mater.*, vol. 7, pp. 665–671, July 2008.

[14] M. Tang, H. Y. Huang, N. Meethong, Y. H. Kao, W. C. Carter, and Y. M. Chiang, "Model for the Particle Size, Overpotential, and Strain Dependence of Phase Transition Pathways in Storage Electrodes: Application to Nanoscale Olivines," *Chem. Mater.*, vol. 21, pp. 1557–1571, Apr. 2009.

[15] L. Laffont, C. Delacourt, P. Gibot, M. Y. Wu, P. Kooyman, C. Masquelier, and J. M. Tarascon, "Study of the LiFePO 4/FePO 4Two-Phase System by High-Resolution Electron Energy Loss Spectroscopy," *Chem. Mater.*, vol. 18, pp. 5520–5529, Nov. 2006.

[16] G. Singh, D. Burch, and M. Z. Bazant, "Intercalation dynamics in rechargeable battery materials: General theory and phase-transformation waves in $LiFePO_4$," *Electrochimica Acta*, vol. 53, pp. 7599–7613, 2008.

[17] N. Meethong, H.-Y. S. Huang, W. C. Carter, and Y.-M. Chiang, "Size-Dependent Lithium Miscibility Gap in Nanoscale $Li_{1-x}FePO_4$," *Electrochem. Solid-State Lett.*, vol. 10, no. 5, p. A134, 2007.

[18] M. Wagemaker, D. P. Singh, W. J. H. Borghols, U. Lafont, L. Haverkate, V. K. Peterson, and F. M. Mulder, "Dynamic Solubility Limits in Nanosized Olivine $LiFePO_4$," *J. Am. Chem. Soc.*, vol. 133, pp. 10222–10228, July 2011.

[19] R. Malik, F. Zhou, and G. Ceder, "Kinetics of non-equilibrium lithium incorporation in $LiFePO_4$," *Nat. Mater.*, vol. 10, pp. 587–590, Aug. 2011.

[20] P. Bai, D. A. Cogswell, and M. Z. Bazant, "Suppression of Phase Separation in $LiFePO_4$ Nanoparticles During Battery Discharge," *Nano Lett.*, vol. 11, pp. 4890–4896, Nov. 2011.

[21] D. Robert, T. Douillard, A. Boulineau, G. Brunetti, P. Nowakowski, D. Venet, P. Bayle-Guillemaud, and C. Cayron, "Multiscale Phase Mapping of LiFePO4-Based Electrodes by Transmission Electron Microscopy and Electron Forward Scattering Diffraction," *ACS Nano*, p. 131105112306007, Nov. 2013.

[22] G. Brunetti, D. Robert, P. Bayle-Guillemaud, J. L. Rouvière, E. F. Rauch, J. F. Martin, J. F. Colin, F. Bertin, and C. Cayron, "Confirmation of the Domino-Cascade Model by $LiFePO_4/FePO_4$ Precession Electron Diffraction," *Chem. Mater.*, vol. 23, pp. 4515–4524, Oct. 2011.

[23] T. Sasaki, Y. Ukyo, and P. Novák, "Memory effect in a lithium-ion battery," *Nat. Mater.*, Apr. 2013.

[24] G. Chen and T. J. Richardson, "Continuity and performance in composite electrodes," *J. Power Sources*, vol. 195, no. 16, pp. 5387–5390, 2010.

[25] K. T. Lee, W. H. Kan, and L. F. Nazar, "Proof of Intercrystallite Ionic Transport in $LiMPO_4$ Electrodes (M = Fe, Mn)," *J. Am. Chem. Soc.*, vol. 131, pp. 6044–6045, May 2009.

[26] E. Callini, L. Pasquini, L. H. Rude, T. K. Nielsen, T. R. Jensen, and E. Bonetti, "Hydrogen storage and phase transformations in Mg–Pd nanoparticles," *Journal of Applied Physics*, vol. 108, no. 7, p. 073513, 2010.

[27] Y. Yan, Y. S. Au, D. Rentsch, A. Remhof, P. E. de Jongh, and A. Züttel, "Reversible hydrogen storage in Mg(BH4)2/carbon nanocomposites," *Journal of Materials Chemistry A*, vol. 1, no. 37, p. 11177, 2013.

[28] J. Newman and C. Tobias, "Theoretical analysis of current distribuion in poruous electrodes," *JOURNAL OF THE ELECTROCHEMICAL SOCIETY*, vol. 109, no. 12, pp. 1183–1191, 1962.

[29] A. Yamada, H. Koizumi, S.-i. Nishimura, N. Sonoyama, R. Kanno, M. Yonemura, T. Nakamura, and Y. Kobayashi, "Room-temperature miscibility gap in $LixFePO_4$," *Nat. Mater.*, vol. 5, pp. 357–360, Apr. 2006.

[30] R. E. Garca, Y.-M. Chiang, W. Craig Carter, P. Limthongkul, and C. M. Bishop, "Microstructural Modeling and Design of Rechargeable Lithium-Ion Batteries," *JOURNAL OF THE ELECTROCHEMICAL SOCIETY*, vol. 152, no. 1, p. A255, 2005.

[31] R. E. García and Y.-M. Chiang, "Spatially Resolved Modeling of Microstructurally Complex Battery Architectures," *J. Electrochem. Soc.*, vol. 154, no. 9, p. A856, 2007.

[32] A. Bueno-Orovio, "Fourier embedded domain methods: Periodic and C extension of a function defined on an irregular region to a rectangle via convolution with Gaussian kernels," *Applied Mathematics and Computation*, vol. 183, pp. 813–818, Dec. 2006.

[33] A. Bueno-Orovio, V. M. Pérez-García, and F. H. Fenton, "Spectral Methods for Partial Differential Equations in Irregular Domains: The Spectral Smoothed Boundary Method," *SIAM Journal on Scientific Computing*, vol. 28, no. 3, p. 886, 2006.

[34] A. Bueno-Orovio and V. M. Pérez-García, "Spectral smoothed boundary methods: The role of external boundary conditions," *Numerical Methods for Partial Differential Equations*, vol. 22, no. 2, pp. 435–448, 2006.

[35] J. R. Wilson, W. Kobsiriphat, R. Mendoza, H.-Y. Chen, J. M. Hiller, D. J. Miller, K. Thornton, P. W. Voorhees, S. B. Adler, and S. A. Barnett, "Three-dimensional reconstruction of a solid-oxide fuel-cell anode," *NATURE MATERIALS*, vol. 5, pp. 541–544, June 2006.

[36] B. Orvananos, T. Ferguson, H.-C. Yu, M. Bazant, and K. Thornton, "Particle-level modeling of the charge-discharge behavior of nanoparticulate phase-separating li-ion battery electrodes," *J. Electrochem. Soc.*, vol. 161, no. 4, pp. A535–A546, 2014.

[37] B. Orvananos, H.-C. Yu, R. Malik, A. Abdellahi, C. P. Grey, G. Ceder, and K. Thornton, "Kinetics of interparticle phase separation." In preparation.

[38] B. Orvananos, R. Malik, H.-C. Yu, A. Abdellahi, C. P. Grey, G. Ceder, and K. Thornton, "Architecture Dependence on the Dynamics of Nano-$LiFePO_4$ Electrodes," *Electrochim. Acta*, vol. 137, pp. 245–257, Aug. 2014.

[39] B. Orvananos, H.-C. Yu, R. Malik, A. Abdellahi, C. P. Grey, G. Ceder, and K. Thornton, "Effect of a Size-Dependent Equilibrium Potential on Nano-LiFePO4 Particle Interactions." In preparation.

[40] F. C. Strobridge, B. Orvananos, M. Croft, H.-C. Yu, R. Robert, H. Liu, Z. Zhong, T. Connelley, M. Drakopoulos, K. Thornton, and C. P. Grey, "Mapping the inhomogeneous electrochemical reaction through porous LiFePO4-electrodes in a standard "coin cell" battery." In preparation.

[41] J. Cahn and J. Hilliard, "Free energy of a nonuniform system .1. interfacial free energy," *JOURNAL OF CHEMICAL PHYSICS*, vol. 28, no. 2, pp. 258–267, 1958.

[42] D. A. Cogswell and M. Z. Bazant, "Theory of coherent nucleation in phase-separating nanoparticles," *Nano Lett.*, 2013.

[43] D. A. Cogswell and M. Z. Bazant, "Coherency Strain and the Kinetics of Phase Separation in $LiFePO_4$ Nanoparticles," *ACS Nano*, vol. 6, pp. 2215–2225, Mar. 2012.

[44] J. Newman and K. E. Thomas-Alyea, *Electrochemical Systems*. Wiley Inter-Science, third ed., 2004.

[45] T. R. Ferguson and M. Z. Bazant, "Nonequilibrium Thermodynamics of Porous Electrodes," *J. Electrochem. Soc.*, vol. 159, pp. A1967–A1985, Jan. 2012.

[46] C. W. Monroe and C. Delacourt, "Continuum transport laws for locally non-neutral concentrated electrolytes," *Electrochim. Acta*, vol. 114, pp. 649–657, Dec. 2013.

[47] P. M. Biesheuvel, Y. Fu, and M. Z. Bazant, "Electrochemistry and capacitive charging of porous electrodes in asymmetric multicomponent electrolytes," *Russ. J. Electrochem.*, vol. 48, pp. 580–592, June 2012.

[48] A. J. Bard and L. R. Faulkner, *Electrochemical Methods. Fundamentals and Applications*. Wiley, second ed., 2001.

[49] P. Bai and M. Z. Bazant, "Charge transfer kinetics at the solid–solid interface in porous electrodes," *Nat. Commun.*, vol. 5, pp. 1–7, Mar. 2014.

[50] C. E. Chidsey, "Free energy and temperature dependence of electron transfer at the metal-electrolyte interface," *Science*, vol. 251, no. 4996, pp. 919–922, 1991.

[51] V. de Velde E F, *Concurrent Scientific Computing*, ch. 8, p. 202. New York: Springer-Verlag, 1st ed., 1994.

[52] J. Hofhaus and E. VandeVelde, "Alternating-direction line-relaxation methods on multicomputers," *SIAM J. Sci. Comput.*, vol. 17, pp. 454–478, MAR 1996.

[53] M. Z. Bazant, "Theory of Chemical Kinetics and Charge Transfer based on Nonequilibrium Thermodynamics," *Acc. Chem. Res.*, vol. 46, pp. 1144–1160, May 2013.

[54] S. Dargaville and T. W. Farrell, "A comparison of mathematical models for phase-change in high-rate $LiFePO_4$ cathodes," *Electrochim. Acta*, vol. 111, pp. 474–490, Nov. 2013.

[55] S. Dargaville and T. W. Farrell, "The persistence of phase-separation in lifepo4 with two-dimensional li+ transport: The cahn–hilliard-reaction equation and the role of defects," *Electrochim. Acta*, vol. 94, pp. 143–158, Apr. 2013.

[56] Y. Zhu and C. Wang, "Galvanostatic Intermittent Titration Technique for Phase-Transformation Electrodes," *The Journal of Physical Chemistry C*, vol. 114, pp. 2830–2841, Feb. 2010.

[57] C. Capiglia, Y. Saito, H. Kageyama, P. Mustarelli, T. Iwamoto, T. Tabuchi, and H. Tukamoto, "Li-7 and F-19 diffusion coefficients and thermal properties of non-aqueous electrolyte solutions for rechargeable lithium batteries," *Journal of Power Sources*, vol. 81, pp. 859–862, Sept. 1999.

[58] L. Valoen and J. Reimers, "Transport properties of LiPF6-based Li-ion battery electrolytes," *JOURNAL OF THE ELECTROCHEMICAL SOCIETY*, vol. 152, no. 5, pp. A882–A891, 2005.

[59] M. Pasquali, A. Dell'Era, and P. P. Prosini, "Fitting of the voltage–Li+ insertion curve of LiFePO4," *Journal of Solid State Electrochemistry*, vol. 13, pp. 1859–1865, Dec. 2008.

[60] Y.-R. Zhu, Y. Xie, R.-S. Zhu, J. Shu, L.-J. Jiang, H.-B. Qiao, and T.-F. Yi, "Kinetic study on LiFePO4-positive electrode material of lithium-ion battery," *Ionics*, vol. 17, pp. 437–441, Feb. 2011.

[61] D. Burch, *Intercalation Dynamics in Lithium-Ion Batteries*. PhD thesis, Massachusetts Institute of Technology, July 2009.

[62] Y. Zeng and M. Z. Bazant, "Phase separation dynamics in isotropic ion-intercalations particles," *arXiv:1309.4543*, Sept. 2013.

[63] H.-C. Yu, B. Orvananos, S. Cronin, M. Z. Bazant, S. Barnett, and K. Thornton, "Smoothed boundary simulation of electrochemical kinetics in LiCoO2 cathode with a complex microstructure." In preparation.

[64] J. Xie, N. Imanishi, T. Zhang, A. Hirano, Y. Takeda, and O. Yamamoto, "Li-ion diffusion kinetics in $LiFePO_4$ thin film prepared by radio frequency magnetron sputtering," *Electrochim. Acta*, vol. 54, pp. 4631–4637, Aug. 2009.

[65] Y. Zhu and C. Wang, "Galvanostatic Intermittent Titration Technique for Phase-Transformation Electrodes," *J. Phys. Chem. C*, vol. 114, pp. 2830–2841, Feb. 2010.

[66] A. Abdellahi, O. Akyildiz, R. Malik, K. Thornton, and G. G. Ceder, "Particle Size and Morphology Dependence of the Preferred Interface in LiFePO4 nanoparticles," *Journal of Materials Chemistry A*, 2014. DOI: 10.1039/C4TA02935F.

[67] Balluffi, Robert W and Allen, Sam and Carter, W Craig, *Kinetics of materials*. John Wiley & Sons, 2005.

[68] M. Ender, J. Joos, T. Carraro, and E. Ivers-Tiffee, "Quantitative Characterization of LiFePO4 Cathodes Reconstructed by FIB/SEM Tomography," *J. Electrochem. Soc.*, vol. 159, pp. A972–A980, Jan. 2012.

[69] J. Chong, S. Xun, X. Song, P. Ridgway, G. Liu, and V. S. Battaglia, "Towards the understanding of coatings on rate performance of $lifepo_4$," *J. Power Sources*, vol. 200, pp. 67–76, Feb. 2012.

[70] B. Kang and G. Ceder, "Battery materials for ultrafast charging and discharging," *Nature*, vol. 457, pp. 190–193, Mar. 2009.

[71] D.-H. Kim and J. Kim, "Synthesis of LiFePO4 Nanoparticles in Polyol Medium and Their Electrochemical Properties," *Electrochem. Solid-State Lett.*, vol. 9, no. 9, p. A439, 2006.

[72] C. Delacourt, P. Poizot, J.-M. Tarascon, and C. Masquelier, "The existence of a temperature-driven solid solution in Li_xFePO_4 for $0 \leq x \leq 1$," *Nat. Mater.*, vol. 4, pp. 254–260, Feb. 2005.

[73] J. L. Dodd, R. Yazami, and B. Fultz, "Phase Diagram of Li_xFePO_4," *Electrochem. Solid-State Lett.*, vol. 9, no. 3, p. A151, 2006.

[74] C. Wang and J. Hong, "Ionic/Electronic Conducting Characteristics of $LiFePO_4$ Cathode Materials," *Electrochem. Solid-State Lett.*, vol. 10, no. 3, p. A65, 2007.

[75] D. Morgan, A. Van der Ven, and G. Ceder, "Li Conductivity in Li_xMPO_4 (M = Mn, Fe, Co, Ni) Olivine Materials," *Electrochem. Solid-State Lett.*, vol. 7, no. 2, p. A30, 2004.

[76] J. Sugiyama, H. Nozaki, M. Harada, K. Kamazawa, O. Ofer, M. Månsson, J. H. Brewer, E. J. Ansaldo, K. H. Chow, Y. Ikedo, Y. Miyake, K. Ohishi, I. Watanabe, G. Kobayashi, and R. Kanno, "Magnetic and diffusive nature of $LiFePO_4$ investigated by muon spin rotation and relaxation," *Phys. Rev. B*, vol. 84, p. 054430, Aug. 2011.

[77] M. Takeuchi, Y. Kameda, Y. Umebayashi, S. Ogawa, T. Sonoda, S.-i. Ishiguro, M. Fujita, and M. Sano, "Ion-ion interactions of $LiPF_6$ and $LiBF_4$ in propylene carbonate solutions," *J. Mol. Liq.*, vol. 148, pp. 99–108, Sept. 2009.

[78] D. Peng, B. Merriman, S. Osher, H. Zhao, and M. Kang, "A PDE-based fast local level set method," *JOURNAL OF COMPUTATIONAL PHYSICS*, vol. 155, pp. 410–438, NOV 1 1999.

[79] T. R. Ferguson and M. Z. Bazant, "Phase transformation dynamics in porous electrodes," *arXiv:1401.7072*, 2014.

[80] A. Van der Ven and M. Wagemaker, "Effect of surface energies and nano-particle size distribution on open circuit voltage of Li-electrodes," *Electrochem. Commun.*, vol. 11, pp. 881–884, Apr. 2009.

[81] M. D. Levi, S. Sigalov, G. Salitra, P. Nayak, D. Aurbach, L. Daikhin, E. Perre, and V. Presser, "Collective Phase Transition Dynamics in Microarray Composite Li xFePO 4Electrodes Tracked by in Situ Electrochemical Quartz Crystal Admittance," *J. Phys. Chem. C*, vol. 117, pp. 15505–15514, Aug. 2013.

[82] D. P. Singh, F. M. Mulder, A. M. Abdelkader, and M. Wagemaker, "Facile Micro Templating $LiFePO_4$ Electrodes for High Performance Li-Ion Batteries," *Adv. Energy Mater.*, Mar. 2013.

[83] H. Zhang, X. Yu, and P. V. Braun, "Three-dimensional bicontinuous ultrafast-charge and -discharge bulk battery electrodes," *Nat. Nanotechnol.*, vol. 6, pp. 277–281, Mar. 2011.

[84] S. J. Dillon and K. Sun, "Microstructural design considerations for Li-ion battery systems," *Curr. Opin. Solid State Mater. Sci.*, vol. 16, pp. 153–162, Aug. 2012.

[85] M. Gaberscek, R. Dominko, and J. Jamnik, "Is small particle size more important than carbon coating? An example study on LiFePO4 cathodes," *Electrochem. Commun.*, vol. 9, pp. 2778–2783, Dec. 2007.

[86] D. A. Porter and K. E. Easterling, *Phase Transformations in Metals and Alloys, (Revised Reprint)*. CRC press, 1992.

[87] L. Wang, F. Zhou, Y. Meng, and G. Ceder, "First-principles study of surface properties of LiFePO4: Surface energy, structure, Wulff shape, and surface redox potential," *Physical Review B*, vol. 76, p. 165435, Oct. 2007.

[88] J. NEWMAN and W. TIEDEMANN, "POROUS-ELECTRODE THEORY WITH BATTERY APPLICATIONS," *AICHE JOURNAL*, vol. 21, no. 1, pp. 25–41, 1975.

[89] T. R. Ferguson, *Lithium-ion Battery Modeling Using Non-Equilibrium Thermodynamics*. PhD thesis, Massachusetts Institute of Technology, 2013.